이학박사 학위논문

Point Source Catalogue of AKARI's NEP-Wide Survey & Mid-Infrared Luminosity Function in the Local Universe

아카리 우주 망원경으로 관측한 황도북극 지역의 적외선 천체목록 및 근접 은하들의 중적외 광도함수

2013년 2월

서울대학교 대학원
물리·천문학부 천문학 전공
김 성 진

Point Source Catalogue of AKARI's NEP-Wide Survey & Mid-Infrared Luminosity Function in the Local Universe

by

Seong Jin Kim
(seongini@astro.snu.ac.kr)

A dissertation submitted in partial fulfillment of the requirements for the degree of

Doctor of Philosophy

in
Astronomy

in
Astronomy Program, Department of Physics and Astronomy
Seoul National University

Committee:

Professor	Myung Gyoon Lee
Professor	Hyung Mok Lee
Professor	Myungshin Im
Professor	Woong-Soeb Jeong
Professor	Jong-Hak Woo

Dedicated to my parents

ABSTRACT

Point Source Catalogue of AKARI's NEP-Wide Survey & Mid-Infrared Luminosity Function in the Local Universe

Seong Jin Kim

Astronomy Program, Department of Physics and Astronomy

The Graduate School

Seoul National University

Infrared space observatory AKARI successfully accomplished one of its mission, the North Ecliptic Pole (NEP) survey. We carried out the data reduction and analysis for NEP-Wide field survey. In order to understand infrared (IR) galaxy populations, we investigated the properties of statistically significant number of IR sources. On the basis of this work, we present a photometric catalogue and properties of IR sources found in the NEP-Wide field. The NEP-Wide survey covered 5.4 deg^2 area centered on the NEP, using nine photometric filter bands from 2.4, 3.2, 4.1, 7.0,, 9.0, 11, 15, 18 and 24 μm of Infrared Camera (IRC). Extensive efforts were made to reduce possible false objects due to the cosmic ray hits, multiplex bleeding phenomena around bright sources and other artifacts. The number of detected sources varied depending on the filter band: with about 109,000 sources catalogued in the near-IR (NIR) bands at 2 to 5 μm, about 20,000 sources in the shorter parts of the mid-IR (MIR) between 7 and 11 μm, and about 16,000 sources seen at longer wavelengths in the mid-IR band, with a few thousand sources catalogued at 24 μm. The estimated

5σ detection limits are approximately 21 mag in the 2 to 5 μm bands, 19.5 – 19 mag in the 7 to 11 μm, and 18.8 – 18.5 mag in the 15 to 24 μm bands in the AB magnitude scale. The completeness for those bands were evaluated as a function of magnitude: 50% completeness levels are about 19.8 mag at 3 μm, 18.6 mag at 9 μm, and 18 mag at 18 μm band, respectively. To validate the detected sources for the construction of a reliable catalogue, all of the detected sources were examined by matching against those in other wavelength data including optical and ground based near-IR bands. The final band-merged catalogue contained about 114,800 sources which were detected at least in one of the IRC filter bands. The 'star-like' sources, defined by the high stellarity and magnitude cut from the ancillary optical data, appear statistically to have a high probability of being stars. The nature of various types of extragalactic sources in this field are discussed in terms of the distributions in various color-color diagrams of the NIR and MIR bands with the redshift tracks providing useful guidelines. We made an analysis of the NEP-Wide sources with spectroscopic redshifts data allowing an accurate determination of the luminosity function of local ($z < 0.3$) galaxies. Infrared luminosities (νL_ν) measured at mid-infrared wavelengths are predominantly attributed to normal galaxies, which means the contributions from luminous galaxies are small. The 8μm luminosity function shows a good agreement with the previous works in the bright-end, suggesting the luminosity evolution, whereas it seems not easy to constrain the faint-end slope.

Keywords: data analysis; catalogue; infrared;galaxies; luminosity function; surveys

Student Number: 2004-30943

Contents

List of Figures

List of Tables

Chapter 1

Introduction

1.1 AKARI space telescope

AKARI (formerly known as ASTRO-F) is a space mission dedicated to infrared (IR) astronomy. Although IR astronomy has been continuously and increasingly important to astronomers since the IRAS mission (Neugebauer et al. 1984), many IR astronomers have relied greatly on the IRAS point source catalogue (Beichman et al. 1988) over two decades, because it was the unique and uniform source of information about the entire sky at mid- to far-infrared wavelengths.

AKARI was designed to carry out a new all-sky survey at 10–180 μm and deep pointed surveys of selected areas at 2–180 μm using modern detector technology with improved resolution, sensitivity and wide wavelengths coverage. The satellite was launched with ambitious expectation in 2006 by ISAS/JAXA (Murakami et al. 2007), and successfully sent into a sun-synchronous polar orbit along the day-night border. The latitude of this orbit is about 700 km and the period is approximately 100 minutes (with the eccentricity ~ 0.017). Table 1.1 summarizes the parameters of the AKARI satellite.

AKARI was equipped with a cryogenically cooled telescope that had a 68.5 cm

Table 1.1 Fundamental Parameters of the AKARI satellite

Main Parameters	Values
Altitude	700 km
Eccentricity	0.0172
Period	99.83 minutes
Mean motion of Argument of Perigee	0.9856 deg day^{-1}
Maximum offset angle out of the observing plane	$\pm$1 deg
Maneuver time from the survey mode to the pointing mode	450 sec
Attitude stabilization time before the pointed observation	300 sec max.
Duration of a pointed observation	600 sec nominal
Maneuver time from the pointing mode to the survey mode	450 sec

diameter (primary-mirror aperture size) with two scientific instruments on the focal-plane: the Infrared Camera (IRC, Onaka et al. 2007) and the Far-Infrared Surveyor (FIS, Kawada et al. 2007). The FIS had 2-dimensional detector arrays covering 50 – 200 μm range with four wide-band photometric filters, and a Fourier Transform Spectrometer (FTS). IRC was designed to carry out near- to mid-infrared imaging with nine photometric filters to provide nearly continuous coverage from 2 to 25μm, and spectroscopic observation with a prism and grisms. The wide field of view (FOV) covered by these instruments made AKARI suitable for efficient surveys.

In addition to the survey mode for all-sky survey, AKARI had the capability to make pointed observation, although it was not a fully observatory-type such as ISO (Kessler et al. 1996) and Spitzer (Werner et al. 2004). The filter system of IRC was designated as $N2$, $N3$ and $N4$ for NIR bands, $S7$, $S9W$ and $S11$ for the shorter part of mid-IR band (MIR-S), and $L15$, $L18W$ and $L24$ for the longer part of mid-IR bands (MIR-L) with the numbers representing the approximate effective

wavelengths in units of μm. The photometric bands with wider spectral widths were indicated by W at the end.

AKARI successfully carried out its missions including all sky surveys at mid to far infrared wavelengths and pointed observations at near to far infrared. The 'cold' mission lasted until the helium boil out on August 26, 2007. After that, AKARI continued its observations with the NIR bands (N2, N3 and N4) during the warm mission. A variety of results based on the AKARI observation including the all-sky and the large area surveys brought a great contribution to infrared astronomy. The North Ecliptic Pole (NEP) survey (Matsuhara et al. 2006) was one of the large area surveys of the AKARI telescope. The AKARI devoted a great deal of time for this survey since the NEP region was the location on the sky with excellent visibility thanks to its Sun synchronous orbit.

1.2 The North Ecliptic Pole (NEP) Survey

1.2.1 NEP-Wide survey

The north ecliptic pole (NEP) is located at $\alpha = 18^h00^m00^s$, $\delta = +66°33'38''$ (See Figure 1.1). Although the NEP is just a blank field sky and not a distinguished region, it is particularly important region for the extragalactic studies. Taking advantages that this region suffers very little obscuration or extinction by foreground Galactic sources, the NEP has been a very good target region for the observation of extragalactic sky. This field is the natural extragalactic deep field location for most space observatories. It is the continuous viewing zone for Herschel (Pilbratt et al. 2010), HST etc., and will also be a likely high visibility wide-field survey region for already planned or upcoming space projects, e.g. Hershel (Pilbratt et al. 2010), SPICA (Onaka et al. 2005; Nakagawa et al 2007). Therefore, many survey data have been accumulated in various wavelength bands ever since the NEP area

was mapped in the soft X-ray photon band (0.3 to 3.5 keV) by the Einstein observatory (Marshall et al. 1985). After the launch of the IRAS satellite, this region was also observed (Hacking et al. 1987; Houck et al. 1988), deeper than the IRAS Point Source Catalogue, although it was limited by detector noise. Loiseau et al. (1988) also mapped an area ($10^\circ \times 6^\circ$) around the NEP in the 11cm continuum and presented list of radio sources. The radio observation at 1.5 GHz (20 cm VLA) band was also conducted by Kollgarrd et al. (1994), still, it was too shallow to identify the mid-infrared sources. And a radio-optical survey was followed on this region (Lacy et al. 1995). And then, the *ROSAT* source catalogue released (Henry et al. 2001, 2006; Gioia et al. 2003) based on the *ROSAT* all-sky survey (RASS, Voges et al. 1999). For the AKARI survey project, pre-survey was also conducted with KPNO-2m/FLAMINGOS in 2004. After the AKARI observation, optical follow-up observations were carried out at CFHT (Hwang et al. 2007) and Maidanak (Jeon et al. 2010) observatories. Also, by other infrared survey such as Spitzer (Werner et al. 2004) and Wide-field Infrared Explorer (WISE, Wright et al. 2010), the NEP region was continuously covered (Jarrett et al. 2011). Many astronomers are still interested in obtaining high-quality data on this region, and relevant proposals are under consideration using various ground-based/orbital facilities and upcoming observation projects (e.g. JWST, SPICA, etc.).

The AKARI's NEP survey was composed of two parts: a wide (henceforth NEP-Wide) survey and a deep (henceforth NEP-Deep) survey. The area observed in the NEP-Wide survey is shown in Fig. 1.1 (green tiles) and is about 5.4 deg^2 with a circular shape (whose radius is about 1.25 deg) centered on the NEP ($\alpha = 18^h00^m00^s$, $\delta = +66^\circ33'38''$) while the NEP-Deep covers about 0.6 deg^2 (Wada et al. 2008, Takagi et al. 2012), with a center slightly offset from the NEP (shaded region) with integration times longer than the NEP-Wide survey. These two surveys are intended to be mutually complementary.

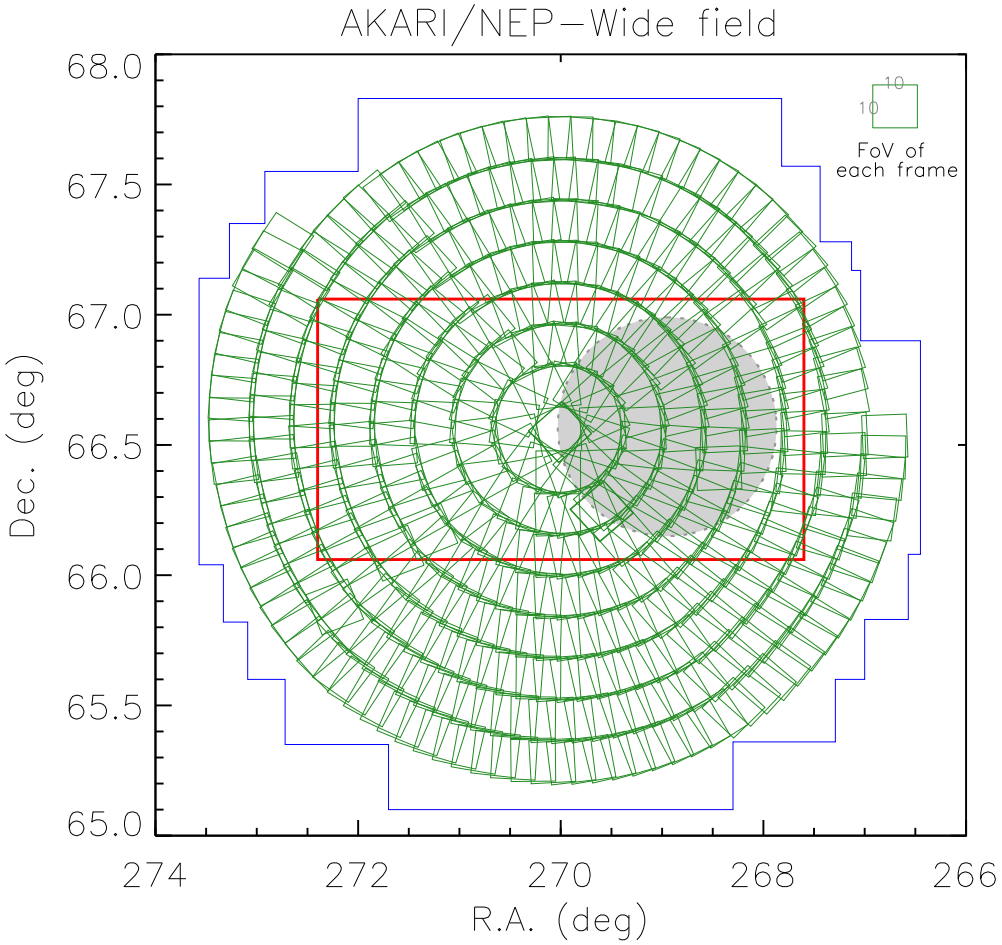

Figure 1.1 The overall map of the NEP-Wide field. The survey consisted of 446 pointing observations represented by green boxes. Each frame covers a $10' \times 10'$ area with half of its field of view (FoV) overlapped by neighboring frames. The red box and blue lines represent the regions covered by optical surveys at the CFHT and Maidanak Observatory, respectively. The circular gray-shaded region denotes the NEP-Deep field.

Prior to the full scale survey of the NEP, mini surveys were carried out during the performance verification period in order to check the performance of the instruments as well as survey strategies. The results of such surveys were already published (Lee et al. 2007; Matsuhara et al. 2007). In addition, AKARI has regularly observed the 'monitor field' near NEP centered at $\alpha = 17^h55^m24^s$, $\delta = 66°37'32''$ with all 9 IRC bands in order to check the stability of the instruments during the entire period of the NEP Surveys. The preliminary analysis of the monitor field data was presented by Takagi et al. (2007).

The NEP-Wide data set has similar but slightly worse (by up to 0.6^m) sensitivity compared to that of the early data of NEP-Deep as presented by Lee et al.(2007) who focused on the nature of 11 μm selected sources covering around $10' \times 10'$ field of view (FOV). They found that a majority of sources detected at MIR are star forming galaxies located at redshift of $0.2 < z < 0.7$. Some of the sources are suspected to be very red objects at much higher redshift. Since the observed area was much smaller than the entire NEP-Wide, there were only 72 sources with 11 μm magnitude brighter than 18.5. By simple scaling, we expected, at that time, to detect around 15,000 MIR sources Here we present the basic strategies of the NEP-Wide survey.

1.2.2 Survey Strategies for NEP-Wide Field

The large area of ~ 5.4 deg^2 of the NEP-Wide survey was required to avoid uncertainty of cosmic variance in the universe at $z = 0.5 \sim 1$, to search for the large-scale fluctuations of the cosmic near infrared background, and to obtain a large sample of luminous infrared galaxies. In order to cover such a large area with small FOV ($10' \times 10'$) of IRC for extragalactic study, NEP is the most suitable area because another high visibility area of South Ecliptic Pole (SEP) region lies very close to the Large Magellanic Cloud and the visibility is not sufficiently high at any other

places.

There were strong constraints on making a large area map using IRC. First, the FOVs of the MIR-L channel is separated by approximately $20'$ from that of the NIR and MIR-S channels of AKARI/IRC, although the three channels take images simultaneously. Second, the position angle of IRC FOVs depends on the date of the observation because the sun-shield of the AKARI satellite always has to point to the Sun and thus the focal plane instruments are aligned along ecliptic coordinates.

Given these constraints, to maximize the survey efficiency toward the NEP we planned to make seven concentric circles (and one additional in some quadrants) centered on NEP with the FOVs of all IRC channels. The survey was scheduled to be completed within a year. Also shown in the figure 1.1 are the NEP-Deep exposure map indicated by shaded region as well as the optical survey area. For the observational redundancy, observations along a circle were planned to be shifted with half of FOVs overlapped with neighboring frames, so that any area would be observed at least twice. Each pointing observation was done by the 'IRC03' template. This observing mode was designed for general purpose imaging observations that take images with three filters in a pointed observation. For each filter two imaging observations are made with dithering operations. The detailed observational procedure for each Astronomical Observation Template (AOT) is described in AKARI IRC Data User Manual (Lorente et al. 2008). The observations were carried out as planned as long as the schedule permits. The NEP-wide survey was completed with 446 pointing observations.

Details of the observational plans for the coordinated pointing surveys, the scientific goals and the technical constraints are described in Matsuhara et al. (2006). The initial results and the catalog for NEP-Deep survey have been reported by Wada et al. (2008).

1.3 Purpose of the Present Study

The success of the AKARI survey like this mission should result in analysis and catalogues to be used in many astronomical studies for the upcoming years. Thereby we are going to describe entire data set of the NEP-Wide survey. The main scientific purpose of this work is to present a point source catalogue of NEP-Wide field observed by AKARI. The significance of a reliable source catalogue after such a survey mission can hardly be overemphasized in astronomy. Therefore, extensive efforts are made with careful attention to reduce the unreliable false object. We also present the detailed description for the data reduction methodology, and make an analysis on the statistical nature of the sources. And, for another goal of this work, we investigate the luminosities of the selected samples to construct the infrared luminosity function of local galaxies in the redshift range of our interest (below z$\sim$ 0.3).

This thesis is organized as follows. In the next chapter (chap. 2), we would like to present details of the data reduction process, characteristics and the significant image corrections needed to improve the efficacy of the image data. We also describe the results of source extraction and photometry as well as the properties of the data such as sensitivity and the completeness of source detection in this chapter. The next chapter (chap. 3) describes the source matching across the available bands to confirm the genuineness of the detected sources and band-merging procedure as well as the contents in the final catalogue. The nature of the detected sources will be shown using various color-magnitude diagrams (CMDs) and color-color diagrams (CCDs) are in this chapter. In chapter 4, this study present the spectroscopic sample of NEP-Wide field and construct mid-IR luminosity function of local (z$<$ 0.3) galaxies using this sample. And then, the results will be summarized in the final chapter.

Chapter 2

Data Characteristics of NEP-Wide survey

2.1 Data Reduction Methodology

2.1.1 Standard Reduction with IRC pipeline

The individual pointing data from the AKARI NEP-Wide field was obtained using the observation template 'IRC03' (Onaka et al. 2007) which was designed for general imaging observations. During a single pointing observation with IRC03, each exposure consisted of observations with three combined filters (2 mid-IR bands and one near-IR band). Fig. 2.1 shows the overall view of the observation sequence, as well as the structure of raw data obtained from a single pointing observation using 'IRC03'.

Each pointing data was reduced by the IRC imaging pipeline (Lorente et al. 2008) implemented in the IRAF[1] environment. We adopted the official package version

[1]IRAF is distributed by the National Optical Astronomy Observatories, which are operated by the Association of Universities for Research in Astronomy, Inc., under cooperative agreement with the National Science Foundation.

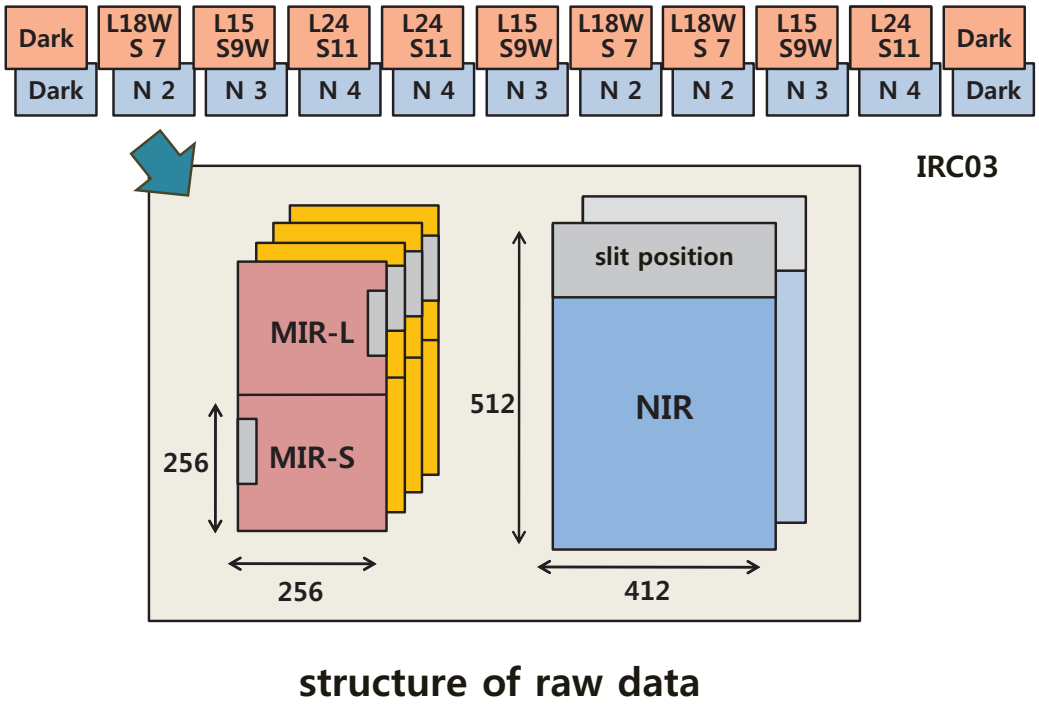

Figure 2.1 An overall view of the observation template IRC03, which was used for NEP-Wide observations. For one pointing observation, the exposure was carried out according to a fixed sequence. The structure of the raw data obtained in the IRC03 mode are shown in the bottom panel. The NIR data consist of one short and one long exposure while the MIR data are composed of one short and three long exposures.

071017 without any modification of the CL script. This software is accessible at AKARI observers web page [2]. The pipeline is composed of three stages, correcting for the instrumental features and transforming the raw data packets to basic science data as described below. The conceptual structure of the pipeline is schematically shown in Fig. 2.2. The structure of the packaged raw data for each individual pointed observation is a 3-dimensional (3D) cube that consists of combined single frames

[2]http://www.ir.isas.jaxa.jp/AKARI/Observation

created during each exposure cycle as shown in Fig. 2.1 The first stage, called the 'Red-Box', slices these into standard 2D image frames and creates an observation log containing the summary of the processed files in the working directory. Each data set can be recognized by its target name, filter name, pointing identification number (PID), and coordinates (R.A., Dec.). Most of these procedures are automatically carried out by running the 'prepipeline' command.

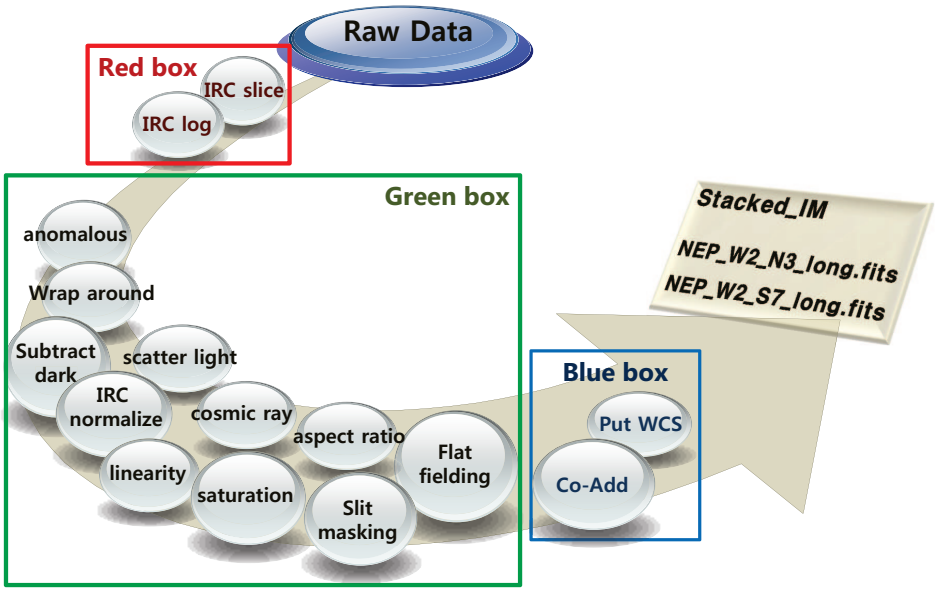

Figure 2.2 A schematic view of the procedures in the pipeline which is designed for the preprocessing of IRC imaging data. The imaging pipeline is composed of three parts.

In the second stage (the Green-box module), the pipeline performs various procedures such as masking of bad pixels, subtraction of dark current, linearization of detector response, and correction for distortion and flat fielding. We chose a 'self-dark' parameter and the pipeline's default flat. The self-dark is an image made by averaging pre-dark images of MIR-S and MIR-L long exposure dark frames from each pointed observation (Lorente et al. 2008). Here, the pre-dark is the dark frame taken at the beginning of the operation for the NIR and MIR channels (Fig. 2.1). The super-dark was obtained from more than 100 pointings of pre-dark images taken at the early stage of the mission to provide superior signal to noise (S/N). However, self-dark may be able to remove hot pixels more efficiently than using the super-dark, especially for the MIR-S and MIR-L. Hence, for the NIR long exposure frames, the super-dark is used to get better S/N. In the MIR data, the cosmic ray hits were removed at this stage. But, for about 20 frames of the $S9W$ and 90 frames of $S11$, there remains a small noticeable pattern in the lower right part even after flat-fielding. We simply removed the area having bright patterns after the pre-processing stage.

The third stage (the Blue-box) calculates the relative shifts and rotations among the frames before stacking, in order to match the attitude of the frames, since the individual frames taken at a given pointing observation are not exactly aligned due to the jitters. Also, the blue-box stage estimates the average sky and adjusts the sky levels for stacking of those frames. We chose the default option 'submedsky' for those processes. At this point, for the staking of MIR-L frames, we used 'coaddLusingS', an optional task in the IRC pipeline, that utilizes the stacking information from the MIR-S frames which are simultaneously obtained with MIR-L frames, thus sharing the identical PID. We used this method because a successful coaddition is guaranteed thanks to the same rotations and shifts as the MIR-S frames of the same PID, even though some of them are not properly stacked when using only MIR-L images. For these tasks, we used long exposure frames, and selected 3σ for the limits of image

statistics in the pipeline reduction. Finally, the IRC pipeline adds header information that supports World Coordinate System (WCS).

2.1.2 Astrometry

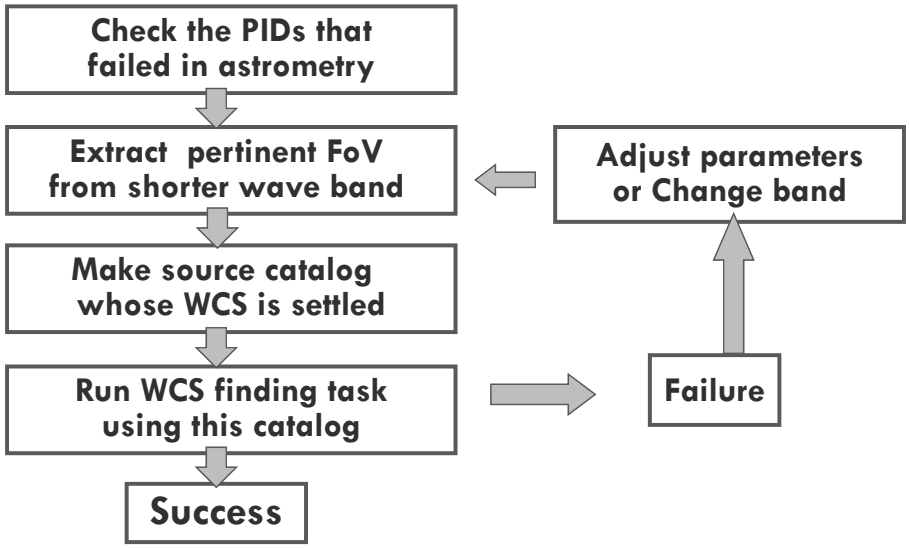

Figure 2.3 Schematic flow chart describing the iterative procedures for finding satisfactory solution for the WCS headers for the $L18W$ and $L24$ bands.

In order to input the information of WCS into the stacked frame, the toolkit 'putwcs' of the pipeline calculates astrometry by matching the bright point sources in the IRC image to reference objects using the Two-Micron All-Sky Survey (2MASS) data (Skrutskie et al. 2006). The astrometric accuracy of the 'putwcs' is less than $1''$ rms for NIR bands, about $2''$ rms for MIR-S bands, and $3'' - 4''$ rms for MIR-L bands (Wada et al. 2008; Shim et al. 2011). The full-width-at-half-maximum (FWHM) of

the stacked frames are about $4''.2$ in NIR bands, and between $5''.2$ – $6''.8$ in MIR bands (Lorente et al. 2008; Lee et al. 2009) depending on the filter.

The 'putwcs' was run automatically on the $N2$ to $S9W$ images. However, this task did not work well for the wavelength bands longer than $S9W$ because of insufficient number of sources having 2MASS counterparts. For that reason, astrometry of $\sim 9\%$ in $S11$ frames was derived by the cross-matching with $S9W$ sources whose WCS solutions had already been resolved. This alternative method was satisfactory since the number of $S11$ frames with unsuccessful 'putwcs' operation was only a small fraction, and the sources in those $S11$ frames were easily identified using $S9W$ data of the same PID. At this stage, a few of the pointing data were discarded due to the stacking failure in the NIR, and very low quality (PID : 2110888). For $L15$ band, the automatic operation of 'putwcs' was successful only for 84% of the frames. The astrometry of the remaining $\sim 16\%$ was done using $S11$ sources in the same manner described above for $S11$ frames. However, the pointing direction of the MIR-L channels is $\sim 20.6'$ apart from that of the MIR-S while NIR and MIR-S share the same field of view. Therefore, in order to use $S11$ sources for the astrometry of $L15$ data, we used pertinent region extracted from the mosaicked image of $S11$ band.

The astrometric solutions for the $L18W$ data were obtained in a similar way to that for the $L15$ band. But the number of common sources between the $L18W$ band and 2MASS data is quite small so that the 'putwcs' operations were applicable for about only 50% of L18W frames. The remaining frames were processed using the $L15$ sources, but these attempts were not fully successful either because, for many frames, the number of $L18W$ sources cross-matched with $L15$ sources was not sufficient. For those frames, we used the corresponding region extracted from the mosaicked images of $S11$ and $S9W$ bands. For the $L24$ band, automatic 'putwcs' was able to find the astrometric solution for only $\sim 10\%$ of the frames since 24 μm sources having 2MASS counterpart are very rare. Therefore, we conducted an alternative source matching

with $L18W$ and $L15$ bands and obtained the astrometry for about 65%. To get correct astrometry using WCS deriving tasks, we have to ensure sufficient number of sources that are effectively available by the fitting process of the software. The iterative procedures to find the enough sources for the astrometry of $L18W$ and $L24$ data are shown schematically in Fig. 2.3. We were able to obtain astrometric solutions for about 90% of the $L24$ frames, leaving $\sim$ 10% of the frames unusable for source detection and photometry.

2.1.3 Post-processing and image correction

Cosmic ray rejection in NIR bands

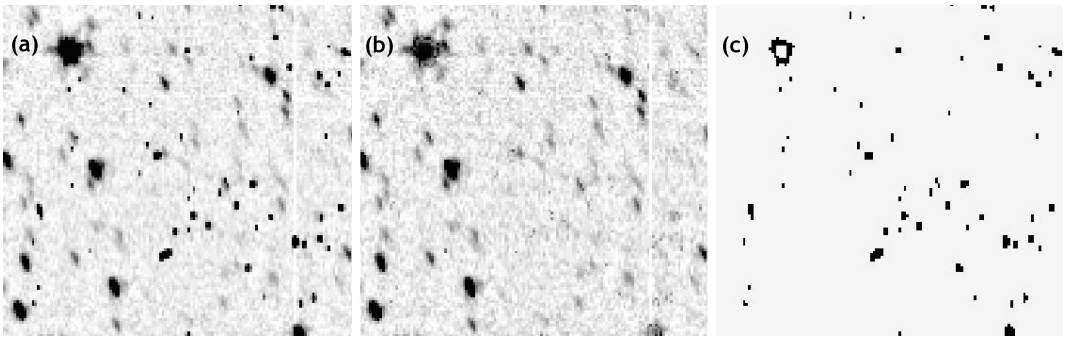

Figure 2.4 An example showing the result of cosmic-ray rejection. The left panel (a) is a sample portion of the $N4$ image produced by the IRC imaging pipeline (PID : 2100757) on which many cosmic rays remain. The middle panel (b) is the same image restored by cosmic-ray rejection using L.A. cosmic procedure. The third panel (c) shows the result of subtraction, (a) - (b), which is just a map showing rejected cosmic rays.

The 'IRC03' template takes three long exposure frames for each NIR band. The last frame $N4$ in a pointed observation may be taken during a satellite maneuver for the next pointing, and can be automatically rejected by the pipeline due to

the poor data quality. As shown in Fig. 2.1, this last exposure was performed to take $N4$ frame while $N2$ and $N3$ frames are safe from the maneuvering period. For that reason, most of $N4$ pointing data have two frames stacked by the pipeline. This causes difficulties in removing cosmic rays from $N4$ frames (as well as a small fraction of $N2$ and $N3$ frames).

Therefore, an alternative method to remove cosmic rays from individual frames has to be applied to those frames before the mosaicking. We used a program 'L.A. cosmic' which is based on the Laplacian edge detection algorithm for highlighting boundaries (van Dokkum 2001). We used the imaging version[3] of the software written in CL script for IRAF users provided by van Dokkum[4]. This procedure relies on the sharpness of the edges rather than the contrast between entire cosmic rays and their surroundings, therefore it is independent of their shapes. The L.A. cosmic procedure was run by the implementation in the IRAF with the default setting. This algorithm was quite robust and it effectively rejected remaining cosmic rays of arbitrary size. Fig. 2.4 shows an example for comparison of the images before (left panel) and after the procedure (middle panel). The right panel shows the difference between two images. However, the sources directly hit by cosmic rays are consequently deformed or damaged during the L.A. cosmic procedure. Therefore, the photometry for those sources are inevitably affected. Most of these damaged sources by cosmic rays are finally rejected by the masking process during the image correction to remove MUX-bleeding effects in NIR bands, as described in the following section.

Correction for MUX-bleeding effects

In addition to cosmic rays, multiplexer bleed trails (or MUXbleeds, hereafter) remained along the horizontal direction in the NIR data due to the nature of InSb

[3]There are imaging version and spectroscopic version for IRAF users.

[4]See http://www.astro.yale.edu/dokkum/lacosmic

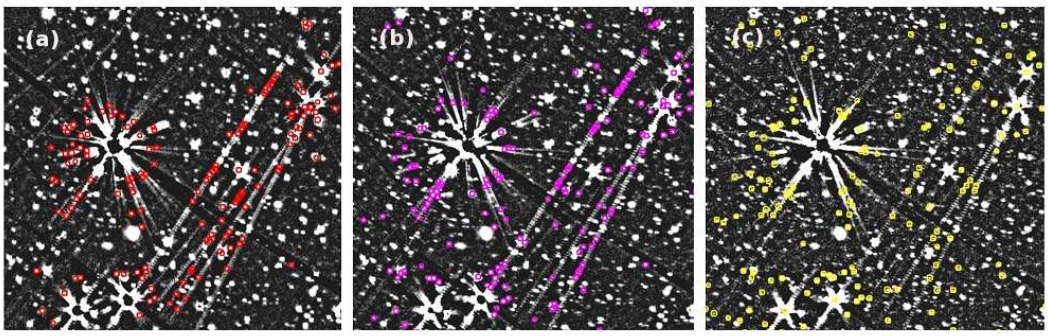

Figure 2.5 Close-up views of a sample region around bright sources showing false detections at each NIR band caused by MUX-bleeding trails before the correction. The left, middle and right panels show the $N2$, $N3$ and $N4$ band images, respectively. Colored circles indicate the objects which are not matched with optical data.

detector array (Holloway 1986; Offenberg 2001). When there is a bright source in a frame, periodic horizontal features appear along the same row. Consequently, many spurious artifacts are detected as sources along the bleeding trails. Fig. 2.5 shows the region where the spurious detection is serious due to MUXbleeds. To mitigate such image artifacts, and to facilitate detection and accurate positional matching with real source in the other bands, we have to apply appropriate rejection procedure. However, it is difficult to accurately correct for the bleeding effect without any influence on the real sources. We simply masked the regions of MUXbleeds, at the expense of rejecting a small number of real sources.

The method we used to mask the region with severe effects is to give a different weight on the selected regions when we make mosaic image with the software SWarp[5]. If we want to remove a region affected by MUXbleeds we give zero weight on that region. Fig. 2.6 shows a schematic overview that describes the steps to determine the region to be masked and make a weight map which is used to generate a

[5]See http://terapix.iap.fr/IMG/pdf/swarp.pdf

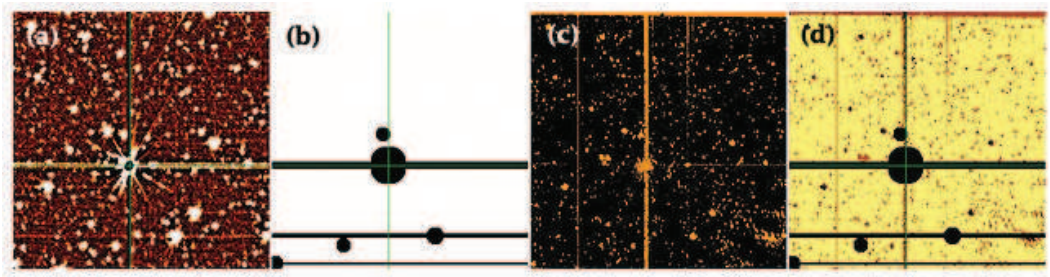

Figure 2.6 Schematic diagram describing the procedures to make a weight map for an individual frame obtained from a single pointing observation. The First panel (a) is a sample image containing bleeding trail and a bright source whose center is disrupted. The second panel (b) shows the regions to be masked. The third panel (c) represents the number of rejected frames during the stacking procedure. Each pixel has an integer value ranging 0 to 3. The last panel (d) is a weight map used for the final mosaic image.

mosaic image at the final stage. The leftmost panel (a) is a sample image reduced by the IRC pipeline. In the second panel (b), dark stripes and circles show the regions to be masked by assigning a zero weight while white regions have 100% weight. The third image (c) shows the number of rejected frames during the stacking procedure in the final stage of the pipeline. For example, there are 3 dithers in the $N2$ band and each pixel in this map may have an integer value ranging from 0 to 3. If we multiply this by 'mask image' of the second panel, we can make the final weight map like panel (d) that gives proper weight factors for individual pixels. Here, the most important task is how to decide the region to be masked to effectively remove the Muxbleeds while minimizing the pixel losses that were not affected by the bleeding trail.

In order to decide the area to be masked, we have to trace the bright sources causing MUXbleeds. We investigated the threshold brightness that begins to create

MUXbleeds. We carried out photometry on all of the individual frames to find the sources brighter than the threshold. The photometry was done on both before and after the L.A cosmic procedure in order to search for the sources hit by cosmic rays and deformed during the cosmic ray rejection process. The results of these measurements enable us to determine the area to be masked, as well as sources distorted by cosmic rays. The typical shape of the masked region around a bright source is a circular disk centered on the centroid of the source, with a narrower horizontal stripe covering the bleeding trail. We found that sources brighter than $\sim$ 12.6 mag cause MUXbleeds in the $N2$ band (about 13 mag in $N3$ and $N4$ bands). The radius of circular area, and the width of the stripe depend on the brightness of the source. For the circular mask, the center is defined by the pixel coordinate of the source that causes the bleeds, and the appropriate radius was chosen to be 2.5 times of the Kron radius (Kron 1980). The width of the stripe was set to be 1.5 Kron radius, and the actual position of stripe was 2 – 3-pixels parallel-shifted in a vertical direction from the original y-coordinate of the source to block the MUXbleed efficiently, because it is not symmetric with respect to horizontal axis. Applying these criteria on each frame, we masked the MUXbleeds and extremely bright sources (brighter than 12.6 magnitude) as well as deformed sources by the cosmic ray rejection procedure in the NIR bands.

In the MIR bands, the MUXbleeds have less significant effects on the image frames because the bleeding trails are rarely found in the $S7$ and $S9W$ bands, and completely disappear in the $S11$ band. Since the horizontal trails usually do not extend to the edge of frame, we used small patches covering the trails around the source in order not to lose too many pixels. However, in about 20 frames of $S9W$ and $S11$ bands, a bright bean-shaped pattern remained in the corner of the frames. The influence from artifacts occasionally caused by moving objects such as satellites or asteroids passing through the field of view were also found in a few frames in MIR-S

bands. To reject those bright artifacts, masking regions were carefully determined with the visual inspection on individual frames and generated weight maps which will be used for image mosaicking basically in the same manner as NIR data. The number of frames that requires weight map for mosaicking was about 10% of MIR-S data.

Weight Maps and Mosaic Images

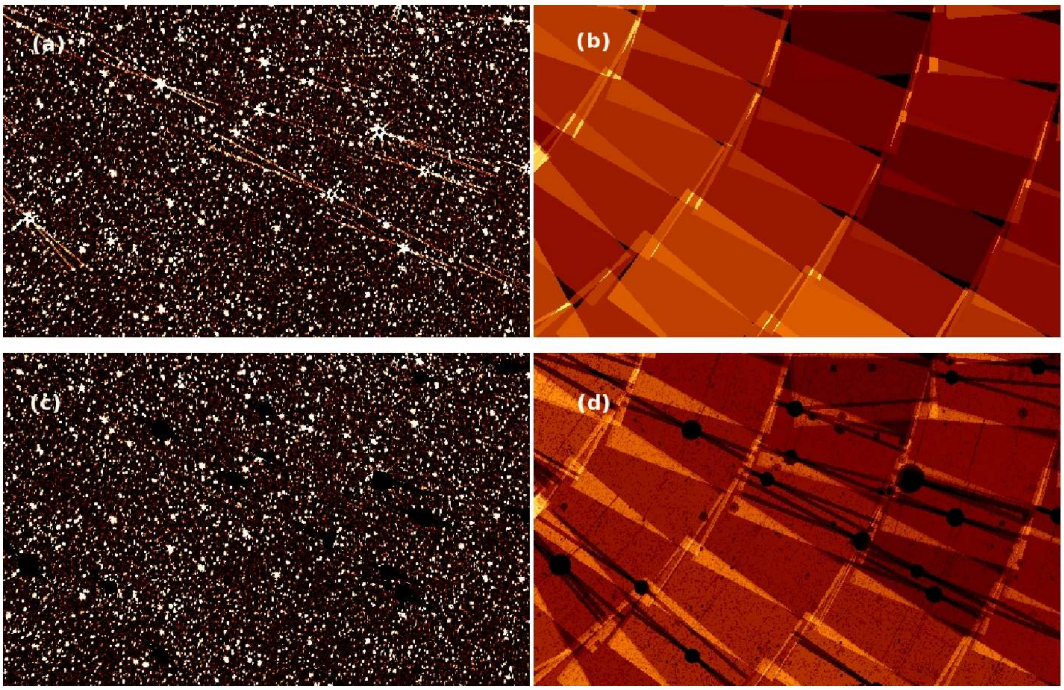

Figure 2.7 Segments of a mosaic images (left) and weighted coverage maps (right) showing before and after the MUXbleed correction ($N3$). The upper pair shows the images before this process and the bottom panels show after the operation. The bleeding trails in this field are completely removed by this weighted mosaicking method using mask image and weight map. In the map (d), none weighted pixels are in black.

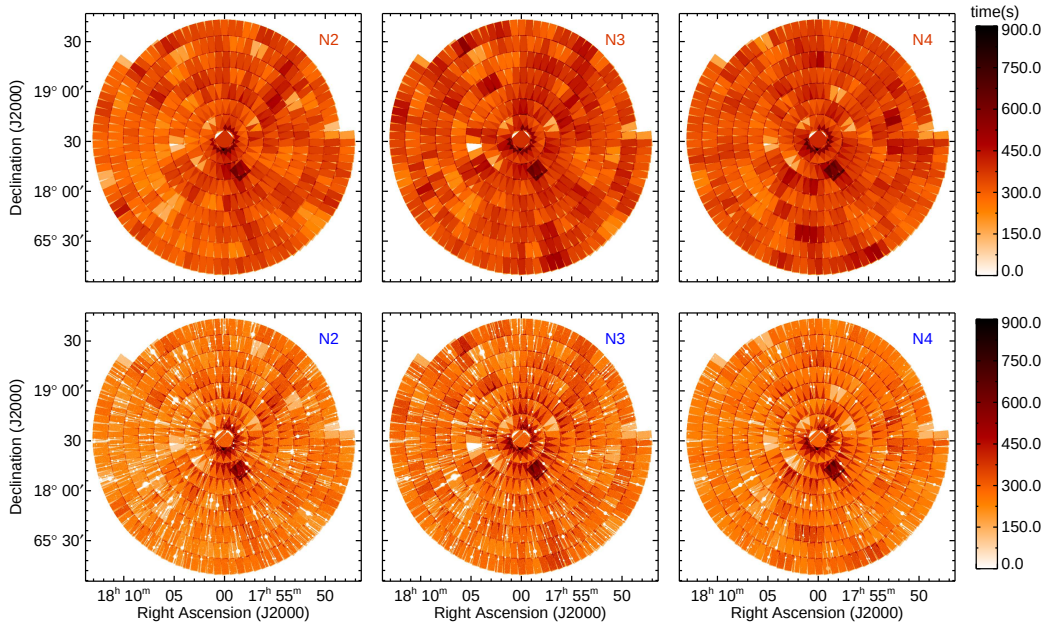

Figure 2.8 Entire coverage maps of NIR data comparing before (upper) and after (lower) the correction for MUX bleeds. Uncovered area and none-weighted pixels have zero-value (white area), which have wedge-like shape from the center to radially outer direction.

To make a mosaic image for each band, we combined individual frames using SWarp. During the SWarp run, the 'WEIGHTED' option was selected as a combine type in order to use the weight maps generated for MUXbleed correction. The BILINEAR resampling method was also used since it is known to be effective at suppressing boundary's discontinuities. In the final mosaic images, there still remain spiky structures close to bright sources because such features are difficult to remove unless we apply rather large circular radii for masking regions. But they do not occupy a significant fraction and do not cause serious false detection problems. False sources are easily filtered out during the confirmation procedure against other bands (see chap. 3).

Fig. 2.7 shows the results of the image correction of MUXbleed effects using two pairs of maps. The upper panels are mosaic (left) and weight (right) maps before correction while the bottom panels show the corresponding images after correction. Most of the bleeding trails in the NIR bands are effectively removed by this process. By co-adding the individual pointed observations, utilizing the weight map for each frame, we finally produced 3 NIR master images for the source extraction and photometry. Among 446 frames, three were excluded due to the stacking failure and poor data quality. The actual area covered by NIR bands is about 5.34 deg^2 and the fraction of masked region ranges 2 – 4% of the observed area. About 0.21 deg^2 was masked out in $N2$ band, and this is about 4% of the entire area covered by $N2$ band. In $N3$ band, 0.198 deg^2 (3.7%), and in $N4$, 0.111 deg^2 (2.1%) was masked, respectively.

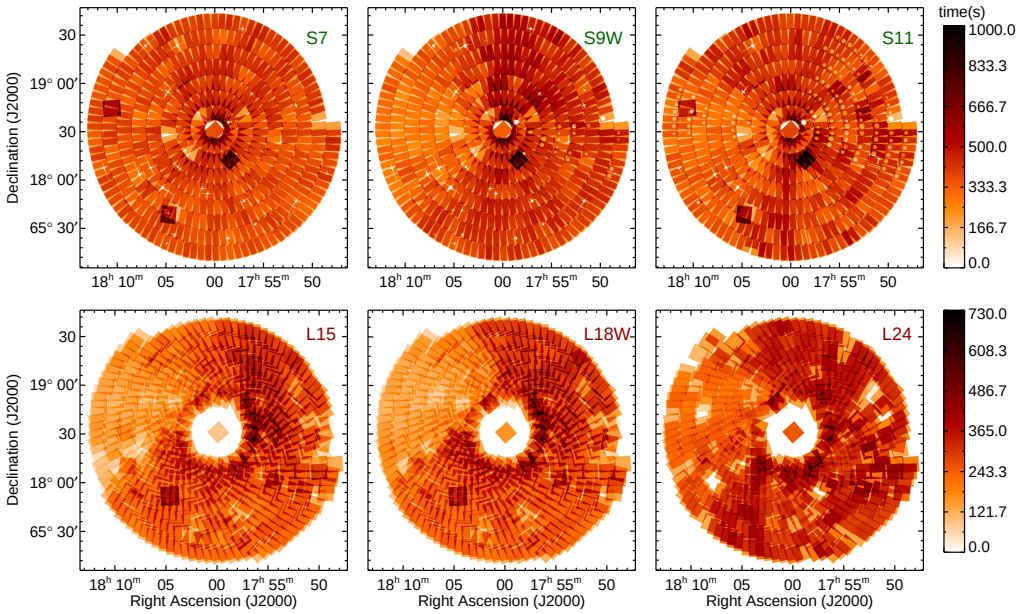

Figure 2.9 Entire coverage maps of MIR-S (upper) and MIR-L (lower) bands.

The weighted coverage maps may help us to understand the overall view of the

final results compared to the uncorrected image data, as shown in Fig. 2.8. The maps before and after correction for NIR bands are presented for comparison. The actual coverage, as well as the masked area were calculated using these maps. The mosaic images for the MIR bands were generated in the same way using weight maps for individual frames, and have the similar coverage maps as shown in Fig. 2.9.

The area observed by the MIR-S bands ranges between 5.33 and 5.35 deg^2. The fraction of the masked region (none weighted regions) is less than ~ 0.03 %, a very small fraction compared to that of the NIR bands (Table 2.1). The masking of the $S7$ band was mainly due to the streaks caused by bright stars in ~ 25 frames. For the $S9W$ and $S11$ bands, the masking was done in order to reject the noticeable patterns in about 20 and 90 frames in the $S9W$ and $S11$ band. Fig. 2.10 shows the segments of resultant mosaic images of $S9W$ band. The upper and lower panels show the images before and after the correction for the irregular artifacts, respectively. For the MIR-L bands, this procedure was not necessary because there is no artifact. Note that there is uncovered region near the central parts of the MIR-L observation because of the offset between the FoV for MIR-S and MIR-L (see Murakami et al. 2007, for the focal plane allocation of the instruments of AKARI).

Table 2.1. Coverage and Masked area

Band	N2	N3	N4	S7	S9W	S11	L15	L18W	L24
Number of combined frames	443	443	443	445	445	445	445	445	445
Areal coverage (deg^2)	5.338	5.338	5.335	5.330	5.341	5.352	4.983	5.007	4.941
Masked area (deg^2)	0.214	0.198	0.111	0.002	0.026	0.016	0.0	0.0	0.0
Fraction of masked region (%)	4.0	3.7	2.1	0.04	0.5	0.3	0.0	0.0	0.0

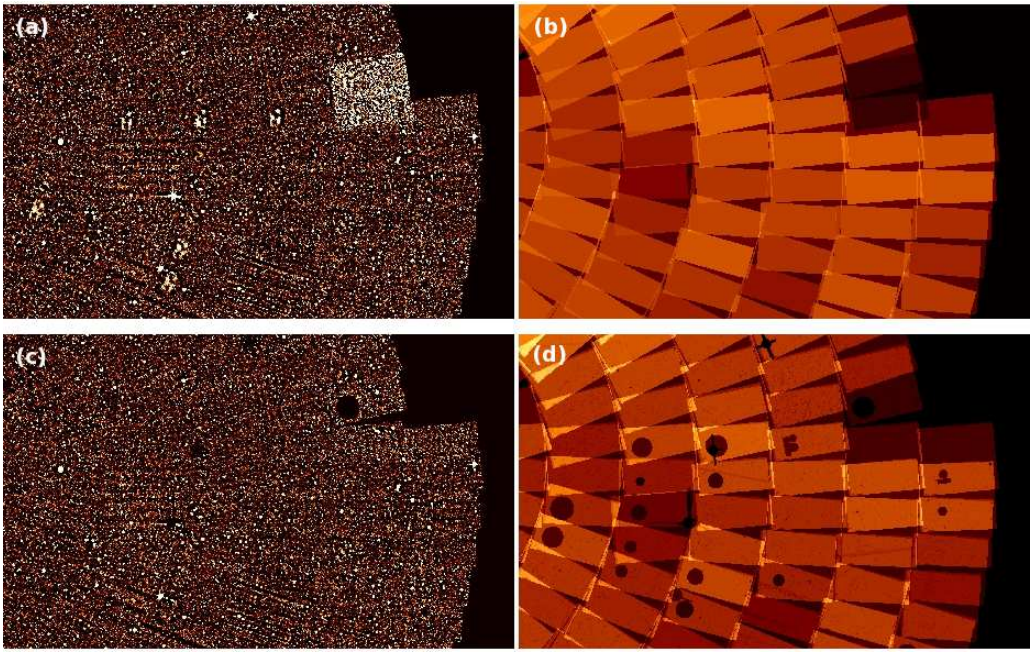

Figure 2.10 Segments of a mosaic images (left) and weighted coverage maps (right) showing before and after the correction for undesirable patterns in *S9W* image. The upper panels show the images before the masking and bottom panels show the resultant images after masking. Coverage maps show that the masking of MIR-S images effectively removes most of the remaining patterns (for about 20 frames), and demonstrates that remaining MUXbleed effects are almost completely removed.

2.2 Photometric Properties of Data

2.2.1 Source detection and photometry

As shown in the previous chapter, we removed most of the MUXbleed effects in the NIR bands, as well as other artifacts in the MIR bands, to minimize spurious detections. We confirmed that the detection reliability was significantly improved by comparing the detected sources from a small portion of both the corrected and the uncorrected images, using the same detection parameters.

We used the entire mosaic images covering the whole NEP-Wide area to carry out extraction and photometry of the sources for each band. To measure the fluxes of the detected sources, we used a software SExtractor developed by Bertin & Arnouts (1996)[6]. Here, we chose DETECT_THRESH=3[7], DETECT_MINAREA=5 and BACK_SIZE=3 to reduce false detection. The number of detected sources from nine master images are presented in Table 2.2, together with the estimated detection limits as described in the following section. In the NIR bands, about 87,800, 104,000 and 96,000 sources are detected from $N2$, $N3$, and $N4$ band, respectively. The number of detected sources in the MIR bands are much smaller than in the NIR bands. In the MIR-S bands, 15,300 ($S7$), 18,700 ($S9W$), and 15,600 ($S11$) sources were detected, and in the MIR-L bands, 13,100 ($L15$), 15,100, ($L18W$), and about 4,000 ($L24$) sources were detected, respectively.

The photometric measurements were made in a single mode operation for each band in order not to use the same aperture for different band images. The size of the sources depends significantly on the effective wavelength of the filter band because the IRC images are nearly diffraction limited. In order to confirm the validity of detected sources and to reject spurious objects, it is more appropriate to employ the single mode operation for each band and look for the counterparts in the other

[6]For the detailed description of this software, See http://terapix.iap.fr/IMG/pdf/sextractor.pdf

[7]We chose a higher threshold than that by Wada (2008) to reduce false detections.

bands.

In order to use flexible apertures for various sources, the fluxes of them were measured using elliptical Kron apertures (i.e., SExtractor's Flux_AUTO), due to the elongated shape of PSFs in NIR bands as well as for the variable sizes and shapes of MIR bands sources. The fluxes in units of ADU are converted to μJy using the flux calibration Table 4.6.7 in the IRC data user manual version 1.4 (Lorente et al. 2008; Tanabe et al. 2008) which has been established based on the observation of the standard stars. Finally we obtained the AB magnitude (Oke & Gunn 1983) using the relation, AB (mag) $= -2.5 \log f_\nu + 23.9$, where f_ν is the flux density within a given passband in units of μJy.

We checked the reliability of the photometry by comparing our magnitudes (mag) of the bright (< 16 mag) sources with those in NEP-Deep catalogue of Wada et al. (2008, see also Takagi et al. 2012). We found that the average magnitudes of the same sources in NEP-Wide and NEP-Deep differ by up to 0.05 mag. Since rms of magnitude differences between NEP-Deep and Wide were about 0.1, the systematic difference of a few hundredths of a magnitude is not considered to be statistically significant. Furthermore the differences are within the absolute calibration uncertainties ($\sim 6\%$). Considering that the observations for NEP-Wide and NEP-Deep surveys were done with different observing templates (i.e. IRC03 for NEP-Wide and IRC05 for NEP-Deep) and the photometry was done with slightly different parameters we regard that the small systematic differences in the measured magnitudes are not serious.

Table 2.2. Number of detected sources and 5σ detection limits

IRC bands	NIR			MIR-S			MIR-L		
	N2	N3	N4	S7	S9W	S11	L15	L18W	L24
FWHM of PSF ($''$)	4.8	4.9	4.9	5.8	5.9	6.1	6.5	6.9	7.3
Number of detected sources	87,858	104,170	96,159	15,390	18,772	15,680	13,148	15,154	4,019
Detection limit in AB	20.93	21.09	21.07	19.48	19.33	18.97	18.59	18.70	17.82
(in μJy)	(15.42)	(13.30)	(13.55)	(58.61)	(67.30)	(93.76)	(133.1)	(120.2)	(274.4)
50% completeness in AB	19.75	19.81	19.87	18.7	18.6	18.2	17.9	18.0	16.8
(in μJy)	(45.68)	(43.39)	(41.02)	(120.2)	(131.8)	(190.5)	(251.2)	(229.1)	(691.8)

2.2.2 Detection Limits and Completeness

The flux limit of the point source detection in each band was estimated from the sky fluctuation, by measuring the flux at random positions far away from the source positions. We used the aperture sizes three times[8] of the FWHM, and determined the 5σ detection limits based on the value of σ derived from the sky background. The detection limits depend on the noise levels of the fields, which vary from place to place, and we present the averaged values over the entire NEP field in Table 2.2. In this table, we listed the FWHMs of sources detected in mosaicked images for all the IRC bands. For each band, we measured the FWHM for about 30 bright sources whose optical counterparts have stellarities greater than 0.95 and took the average of them. In the NIR bands, the $N2$ filter reaches a depth of $\sim$ 20.9 mag, and the $N3$ and $N4$ bands each reaching $\sim$ 21.1 mag. The MIR detection limits are much shallower: $\sim$ 19.5 ($S7$), 19.3 ($S9W$) and 18.9 mag ($S11$) for the MIR-S bands, and $\sim$ 18.5 ($L15$), 18.6 ($L18W$) and 17.8 mag ($L24$) for the MIR-L bands. In the table, the 50% completeness levels, that are measured by injecting artificial sources as described below, are also presented.

Using IRAF tasks in `noao.artdata` package, we generated artificial sources with a fixed range of magnitude and spread them at random positions in 8 sample regions of $10' \times 10'$ selected from all over the mapped area. The sources injected at positions within a distance of 20 pixels from any other sources are not counted as input sources in order to avoid source blending and miscount. We attempted to detect the injected objects and measured the brightness of them by running the SExtarctor with the same parameters as those applied for the detection and photometry for the real sources.

[8]This size is usually sufficient to measure the total magnitude.

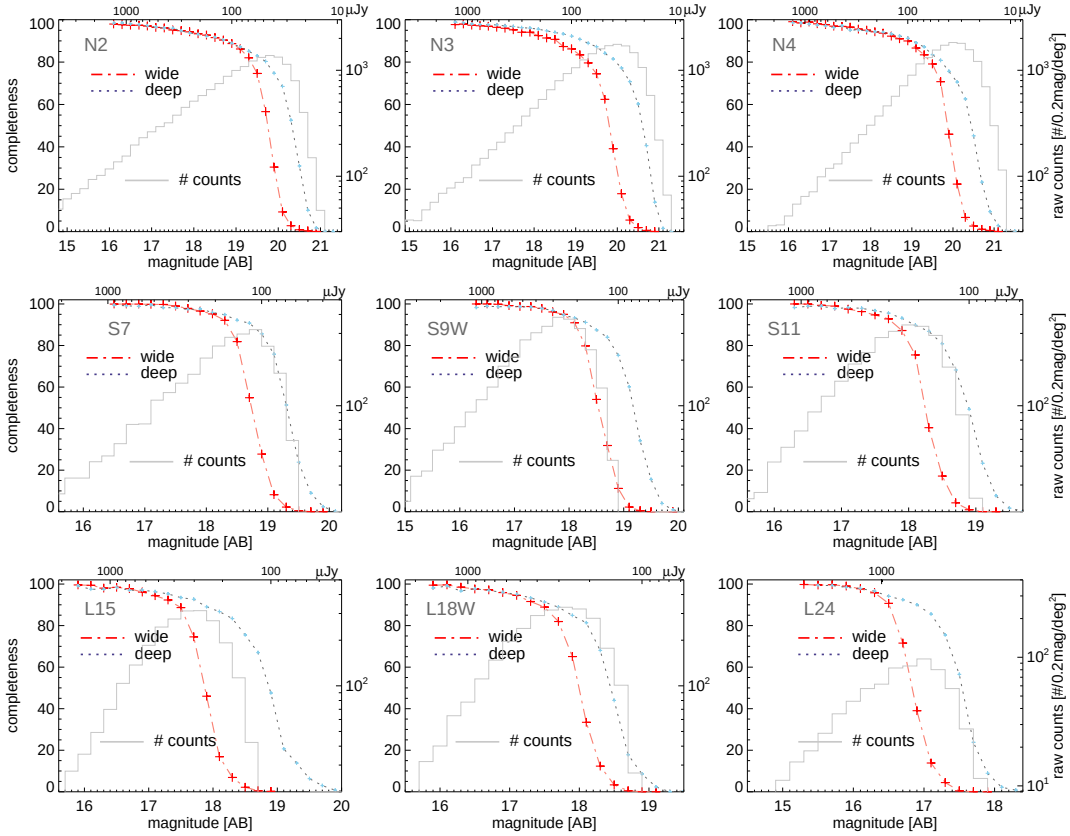

Figure 2.11 The completeness estimation for each band (red curves). The estimates for the NEP-Deep data by Wada et al. (2008) are also shown for comparison. The gray histograms show the NEP-Wide the source density per square degree per 0.2 magnitude bin at each band (not corrected for incompleteness).

For each magnitude bin, we repeated the same procedures 7 – 10 times with different seed numbers for brightness and spatial distribution, and took the average. Among the various input parameters for this test, the most sensitive was found to be the half intensity radius at each wave band.

The completeness fraction for the IRC bands of NEP-Wide data are shown in Fig. 2.11 as a function of magnitude. We also show the estimation of the completeness for NEP-Deep (Wada et al. 2008) data using the same parameters as those employed for the NEP-Wide data.[9] The completeness curve shows that the detection probability begins to drop rapidly from about 85% value in the NIR bands, and about 90% in the MIR bands. The magnitude difference between the 90% and 10% completeness is about 1 mag in the NIR bands, and less than 1 mag in the MIR bands. The 50% completeness level are about 19.8 in the NIR bands, 18.7 – 18.3 mag in the MIR-S bands, and 18.0 – 16.8 mag in the MIR-L bands, as presented in Table 2. The differences of 50% complete magnitudes between the NEP-Wide and NEP-Deep data are about 0.5 – 0.6 in the NIR and MIR-S bands. In the MIR-L bands, the differences are 1.0 ($L15$) – 0.5 mag ($L18W$).

Fig. 2.12 shows the comparison of the 5σ detection limits and 50% completeness magnitudes for the IRC bands. The measurements of detection limits using individual frames are also shown for comparison (gray). These estimates using mosaic images give slightly shallower detection limits than those measured using the individual frames for the NIR bands while deeper limits are measured for the MIR bands. The differences in the NIR bands are less than 0.2 mag and possibly results from the variation of the image quality, for example from FWHM changes and seeing variations, along with resampling during the mosaicking process.

[9]The parameters of the source detection and photometry applied for NEP-Wide data are somewhat different from those used for NEP-Deep data (Wada et al. 2008), thus the parameters for the completeness estimation for NEP-Deep data in this test are also different from those used by Wada et al. (2008).

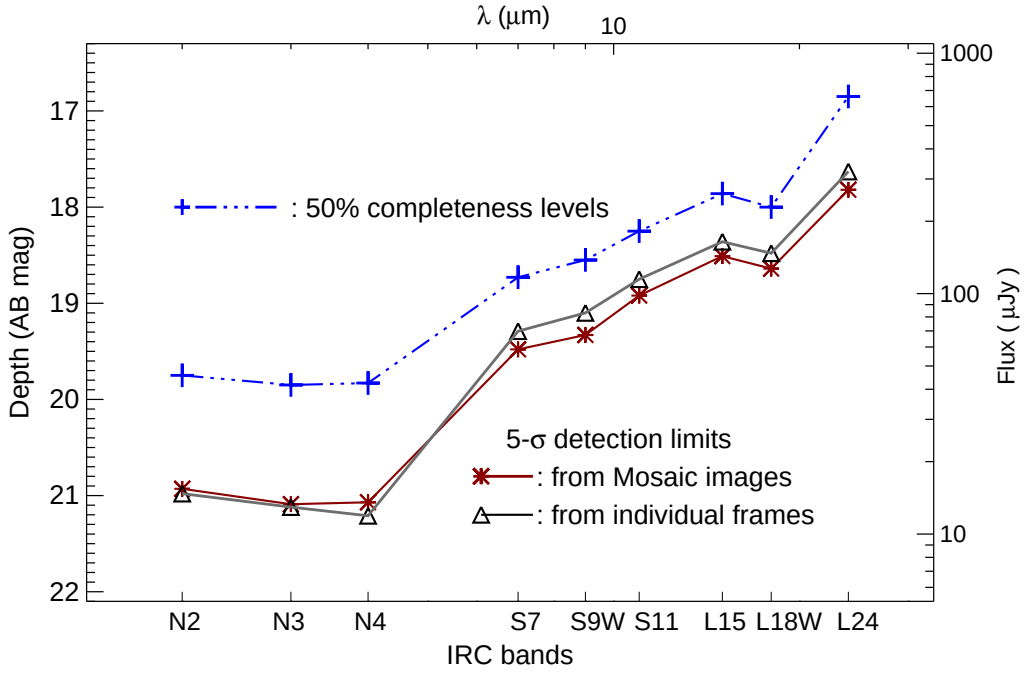

Figure 2.12 The flux detection limits and 50% completeness levels for each band. The detection limits of the NIR bands are around 21 mag, and MIR bands reach much shallower depth than NIR bands. The 50% completeness levels are about 1.2 mag shallower than the detection limits in the NIR filters and about 0.7 mag shallower in the MIR bands from $S7$ to $L18W$.

The 50% completeness limits are shallower than the 5σ detection limits by about 1.2 – 1.3 mag. for the NIR bands and about 0.6 – 0.8 mag for the MIR bands (except for $L24$ which has a relatively larger difference of 1.0 mag). Wada et al. (2007) also found a similar trend in the differences between the 5σ detection limits and 50% completeness limits for the NEP-Deep data. By comparing a single exposure and stacked image of ten exposures, they found that the 50% limits do not improve much for the NIR bands, while the improvements for the MIR bands are close to the square-root of the exposure time. On the basis of these results, they concluded that

the NIR bands are affected by the source confusion. In fact, the improvement in the 50% limit between one pointing and ten pointing observations is only a factor of 1.15 (Wada et al. 2007) for the $N3$ band, implying that the source confusion could be significant.

The MIR bands are unlikely to be affected by the confusion because the source density is much lower than that of the NIR bands, while the sizes of the PSFs are nearly the same (Lee et al. 2009). The smaller difference between the 50% completeness and 5σ detection limit can thus be understood by the confusion effects in the NIR bands. Note that the numbers of source per beam are 1/60.7, 1/46.8, and 1/51.3 for $N2$, $N3$ and $N4$ bands, respectively. These values are smaller than the classical definition of the confusion limit of 1/30 sources per beam, but only by a factor of two. The NIR band observations are affected by the source confusion to some extent.

Chapter 3

Construction of the Point Source Catalogue

3.1 Confirmation of the Sources

3.1.1 Supplementary data

In addition to our AKARI/NEP-Wide data, high-quality optical data, NIR J and H band data, and radio data over a more limited field are available for the NEP-Wide field (Kollgaard et al. 1994; Lacy et al. 1995; Sedgwick et al. 2009; White et al. 2010). Optical data were obtained using the 3.5m Canada-France-Hawaii Telescope (CFHT) for the inner parts and the 1.5m telescope at Maidanak observatory in Uzbekistan for the outer parts of the NEP-Wide field as shown Fig. 1.1. The CFHT observations with the MegaCam covered the inner part of the 2 deg^2 rectangular field centered on the NEP using the u^*, $g^{'}$, $r^{'}$, $i^{'}$, $z^{'}$ filter system. The detection limits (4σ) are about 26 mag for u^*, $g^{'}$, $r^{'}$, about 25 mag for $i^{'}$, and 24 mag for $z^{'}$ band, and the full catalog contains over $\sim$ 110,000 sources (Hwang et al. 2007). The Maidanak observations were carried out using the SNUCAM (Im et al. 2010). The

observations covered the outer regions surrounding the CFHT field using B, R, I filters (Jeon et al. 2010), whose depths are around 23 mag in B, R and about 22 mag in I band. In addition, NIR J, H band data was obtained using FLAMINGOS mounted the Kitt Peak National Observatory (KPNO) 2.1m telescope, which cover the entire NEP-Wide area ($\sim$ 5.2 deg^2). The number of sources in this data is over 220,000 (Jeon et al., in preparation). The optical data are crucial for identifying the nature of the corresponding AKARI sources, since the stellarity parameters help us to distinguish between stars and galaxies. The J, H data are used to bridge the gap in wavelength coverage between the AKARI/NIR and the optical data.

3.1.2 Overview of the source matching

To construct a reliable source catalog, we have to validate the detected sources. If a certain source is detected at only one filter band without any counterpart in the other bands, it could potentially be as a false detection, especially in the case of the NIR bands. In order to verify the reliability of detected sources in a given IRC band, we searched for their counterparts within a $3''$ radius in the other IRC bands, as well as ancillary optical and J, H band data search parameter. The overall matching procedures concerning NIR bands are summarized in Fig. 3.1. The choice of $3''$ as a matching radius is somewhat arbitrary: we considered the astrometric accuracy of the NEP-Wide data to be $1.38''$ (Lee et al. 2009), hence selected a search radius of twice of this value. We tried several values and found that the number of matched sources begins to increase very slowly with radius larger than $2''$, and nearly saturates at around $3''$. Note that the typical size of the FWHM of the point sources ranges from $5''$ (NIR) to $7''$ (MIR) (see Table 2.2), approximately corresponding to the diameter of the matching circle.

In the case of the $N2$ band, for example, the positional matching with $N3$ and $N4$ band were examined first. Then, we proceeded to find counterparts in the optical,

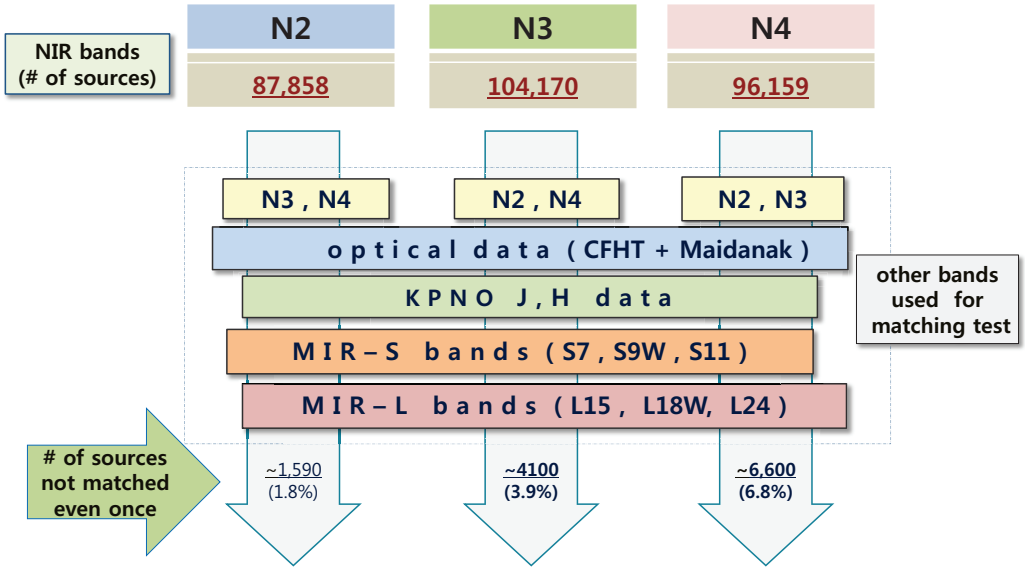

Figure 3.1 Schematic overview of the matching procedures for the sources in AKARI bands. The boxes at the top of the diagram show the number of detected sources in each band. Under those boxes, the downward arrows denote the matching order. Each NIR band sources were matched against those in other NIR bands first, and then matched with optical, KPNO J, H bands data. The MIR data are used during the final stage.

and KPNO's J and H bands. We finally looked for the matching sources in the AKARI's MIR-S and MIR-L data. In the lower part of the figure, we showed the number of sources which were not matched even once during these procedures on the heads of downward arrows. About 1,580 of the $N2$ sources ($\sim$ 1.8%) do not have any counterpart in any of the other bands. In the $N3$ and $N4$ bands, about 3.9% and 6.8% of the sources remained unmatched against any other band data, respectively. All of these unmatched sources can not be confirmed and are likely to be false objects. We excluded such sources in the catalogue.

To find counterparts of the MIR sources, a similar procedure was applied as

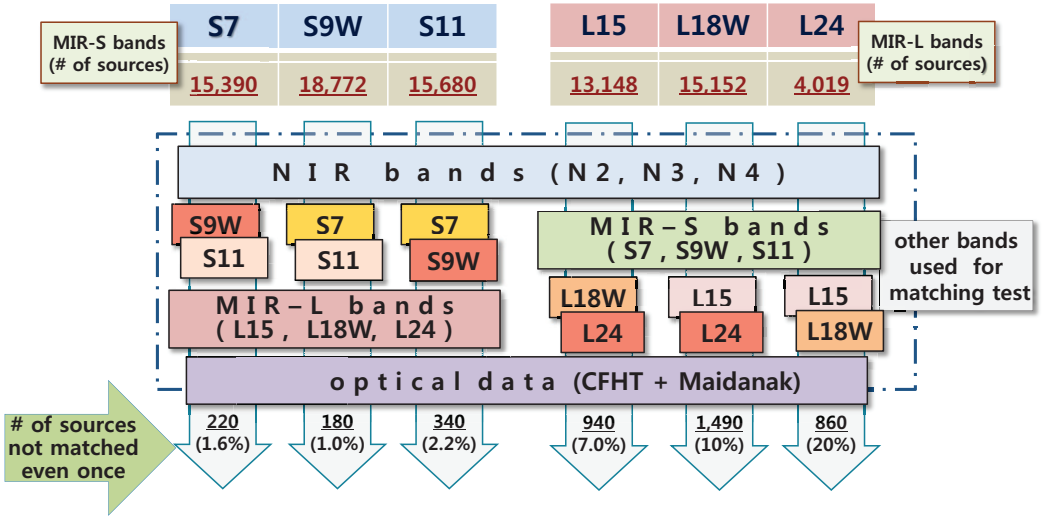

Figure 3.2 Same as Fig. 3.1, but for MIR sources, showing the matching procedure. The numbers of detected sources in MIR bands are given on the top of the diagram. Downwards arrows denote the order of the matching tasks. Each of the MIR sources was first matched against those in the NIR bands first, and then, with those in the other MIR data. Optical counterparts are also investigated.

shown in Fig. 3.2. The number of detected sources in each MIR band is given in the boxes on the top of the diagram. The cross-matching of the sources in each of the MIR band was carried out against the others from the NIR to MIR-L bands in order of wavelength. The numbers of sources having no counterparts after this procedure is given in the lower part of the diagram. The fractions of sources without any counterparts are 1.6%, 1.0%, and 2.2% for the $S7$, $S9W$ and $S11$, respectively. For the MIR-L bands, about 7%, 10%, and 20% of sources in the $L15$, $L18W$ and $L24$ bands remained unmatched against those in other bands. Unlike in NIR bands, it is risky to exclude all of the MIR sources having no counterparts because the artifacts are less serious in MIR bands compared to NIR bands, and very red objects can be detected in a long wavelength band. Therefore we checked all the unmatched sources

by eye and included almost of them except for very rare cases ($\sim 2\%$) with spurious images.

The results of the matching procedures among the IRC bands as well as against optical data are presented in Table 3.1. The numbers in this table include the sources that were matched more than once, which are given in the parenthesis. Duplicated source, or multiple matching occurred predominantly when the sources were located in a crowded region, although numerically they represent a small fraction of the total.

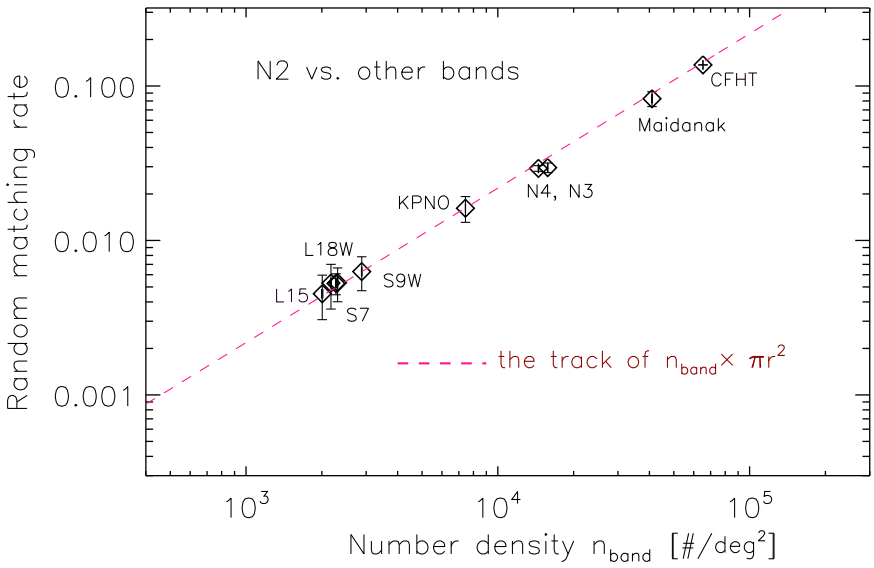

Figure 3.3 The probability of random matching for the $N2$ band sources with those in other bands. The random matching probability is proportional to the density of the sources in the band to be matched, as indicated by the dotted line.

When two band data are used to find a counterpart, there is always a possibility of false matching. Suppose that the sources in bands A and B are uncorrelated and randomly distributed in space. In this case, the fraction of the sources in band A

Table 3.1. The number of sources matched with those in other bands

IRC Bands	Optical	N2	N3	N4	S7	S9W	S11	L15	L18W	L24
N2	72,871 (83%)	87,858 (0)	81,012 (22)	71,919 (21)	13,357 (1)	16,017 (3)	12,643 (2)	8,170 (1)	8,554 (2)	2,070 (1)
N3	77,223 (74%)	81,049 (59)	104,170 (0)	84,856 (49)	13,752 (7)	16,563 (5)	13,180 (3)	9,321 (2)	10,167 (3)	2,266 (0)
N4	67,667 (70%)	71,938 (40)	84,850 (43)	96,159 (0)	14,169 (7)	16,996 (7)	13,434 (2)	9,784 (5)	10,841 (6)	2,454 (0)
S7	13,928 (90%)	13,356	13,745	14,162	15,390	12,091	8,489	4,790	4,750	2,059
S9W	16,662 (89%)	16,014	16,558	16,989	12,091	18,772	12,923	6,757	7,040	2,389
S11	13,404 (85%)	12,641	13,177	13,432	8,489	12,923	15,680	7,084	7,229	2,476
L15	8,628 (66%)	8,169	9,319	9,779	4,790	6,757	7,084	13,148	9,377	2,571
L18W	9,217 (60%)	8,552	10,164	10,835	4,750	7,040	7,229	9,377	15,154	2,673
L24	2,280 (57%)	2,069	2,266	2,454	2,059	2,389	2,476	2,571	2,673	4,019

accidentally matched with those in band B is simply $n_B \times \pi r_{match}^2$, where r_{match} is a matching radius. We confirmed this simple relationship between the source density and the false matching rate by numerical simulations: we tried to match the $N2$ sources to those in other band data but in different fields of the same size, the results of which are shown with diamonds in Fig. 3.3. A dotted line in this figure is an expected relation from the numerical simulation. The matching experiments with the real data for random fields of view show good agreements with the expected relation based on a random-matching probability argument. In our cross identification procedure, the density of the optical data is the highest: the CFHT catalog (Hwang et al. 2007) contains about 118,200 sources in 1.8 deg^2 and thus the source density is 65,700 per deg^2. When we used the matching radius of $3''$, the false matching rate was about 14.3%. For the Maidanak data, the source density is about 41,100 per deg^2 and the false matching rate is estimated to be 9%.

However, these probabilities should be regarded as upper limits for the false matching since the sources detected in the same field of view should be actually correlated, i.e., a source at a given band is likely to be present in the other bands. In order to make more realistic estimates of the false matching rate, we varied the matching radius. In the case of the matching test between the $N2$ and CFHT optical data, for example (Fig. 3.4), we found that the number of the $N2$ sources that have the optical counterparts in an annulus corresponding to matching radii of between $2.5''$ and $3''$ comprises about 1.41% instead of the random matching probability of 4.37%. In the case of the matching with the Maidanak data, we expect a 2.75% false matching rate for the same annulus, but only 1.08% matched sources were found. If we assumed that all the sources in this annulus had been accidently matched, the false matching could be less than 1.5%. We thus conclude that the false matching probability must be very low.

3.1.3 Summary of the source matching

Matching between IRC bands

The results of the source matching among the different wavebands are used for confirmation of the sources. In the AKARI/NEP-Wide data, number of sources in NIR bands are much larger than that of MIR sources. Consequently, majority of MIR sources have NIR counterparts, but the reverse is not true. Therefore, it is reasonable to combine the information on the basis of the NIR framework.

As explained in the previous section, matching between any two bands was performed in both directions. Between the $N2$ and $N3$ bands, for example, we first searched counterparts in the $N3$ band for a given $N2$ source, and then changed the direction. Similar procedures were applied for all possible combinations of the three NIR bands as shown in Fig. 3.5. The numbers shown in the ellipses on the three sides of the triangle are those of the sources, with the number of detection in both bands presented at the apexes. Using the results from cross-matching in both directions, we can find duplicated or multiply matched sources between two bands. The number of sources detected in both $N2$ and $N3$ was 80,990, in $N2$ and $N4$ was 71,898, and the in $N3$ and $N4$ was 84,807.

For a given MIR source, there could be multiple NIR or optical sources since the PSF of the MIR is much larger than that of NIR and source density in NIR is much higher (by up to $\sim$ 8 times) than that in MIR. In such cases, we simply chose the nearest one from the MIR source. On the other hand, there is no multiple matching of MIR sources for a given NIR source. We summarize the results between NIR and MIR bands in the Fig. 3.6. Among the MIR bands, there are no duplicated matches, as presented in the Table 3.1, since the number density of the MIR sources is much lower.

Optical identification

On the left and right hand sides of Fig 3.7, the numbers of sources matched with each of the optical catalogs are presented. Note that the total number of $N3$ sources is 104,170, while the number of them in the CHFT field is about 36,380. Amongst these sources, 82.8% in the CFHT field have optical counterparts. Similarly, the number of $N3$ sources located in the Maidanak field is about 82,750, which is more than twice the number of sources in the CFHT field, and 62.4% of these sources have Maidanak optical counterparts. On the whole, 74.1% of the $N3$ sources have counterparts in either the Maidanak or CFHT data. As shown in the lower part of Fig. 3.7, 83.0% of the $N2$ and 70.4% of the $N4$ sources have optical counterparts. The rate of matching with optical data decreases with NIR band wavelength. The matching rate with the CFHT data is somewhat higher than with the Maidanak data, because the CFHT observations are deeper.

We also examined the matching of the NIR sources against KPNO J, H data. The cross matching results are presented in Fig. 3.8. For the $N2$, $N3$ and $N4$ bands, 78%, 63% and 65 % have counterparts in KPNO data, respectively.

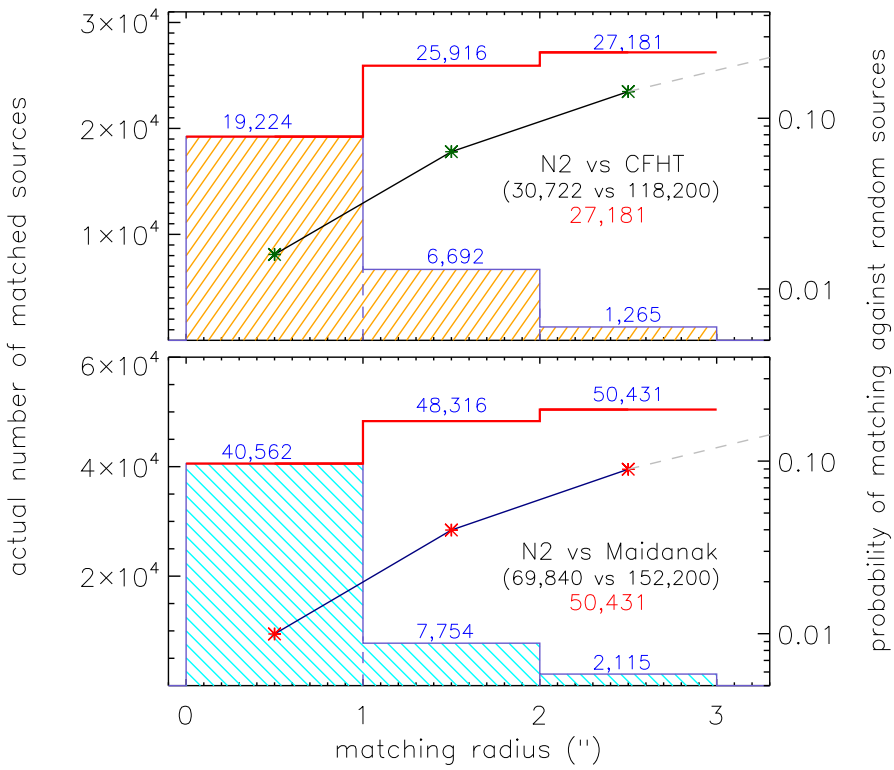

Figure 3.4 The probability of random matching for the $N2$ band sources with those in other bands. The random matching probability is proportional to the density of the sources in the band to be matched, as indicated by the dotted line.

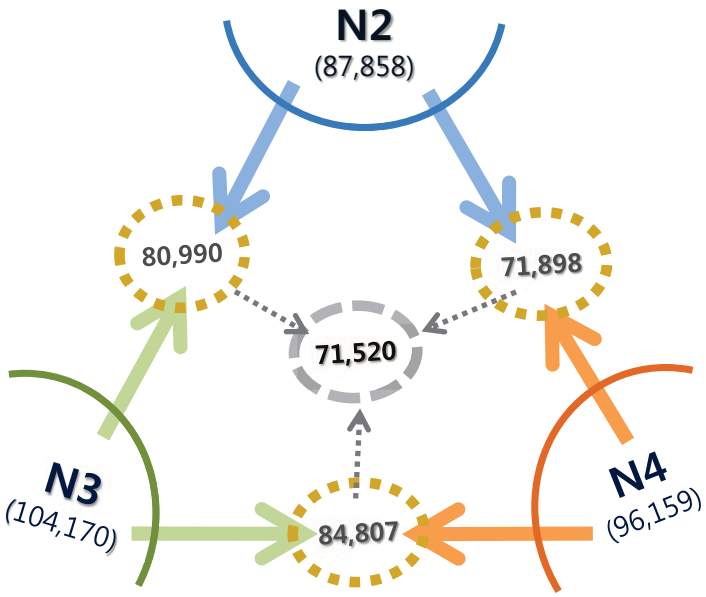

Figure 3.5 Summary of the source matching between the different NIR bands. The numbers of sources detected at each NIR band are presented at the apexes of the triangle. The matching results among them are shown, excluding duplicated or multiply matched sources. The numbers in the dotted ellipses represent the number of sources with the detection in both of the matching bands.

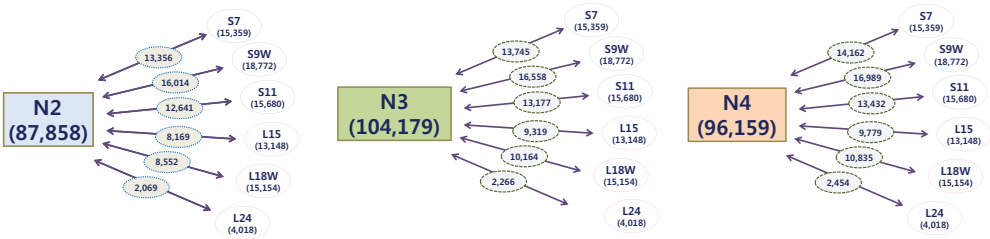

Figure 3.6 Schematic diagram showing the matching results between the sources in NIR and MIR bands except for multiply matched sources. The matching results of $N2$ sources against all the MIR bands are shown in the leftmost panel. The results for $N3$ and $N4$ bands are shown in the middle and the right panels, respectively.

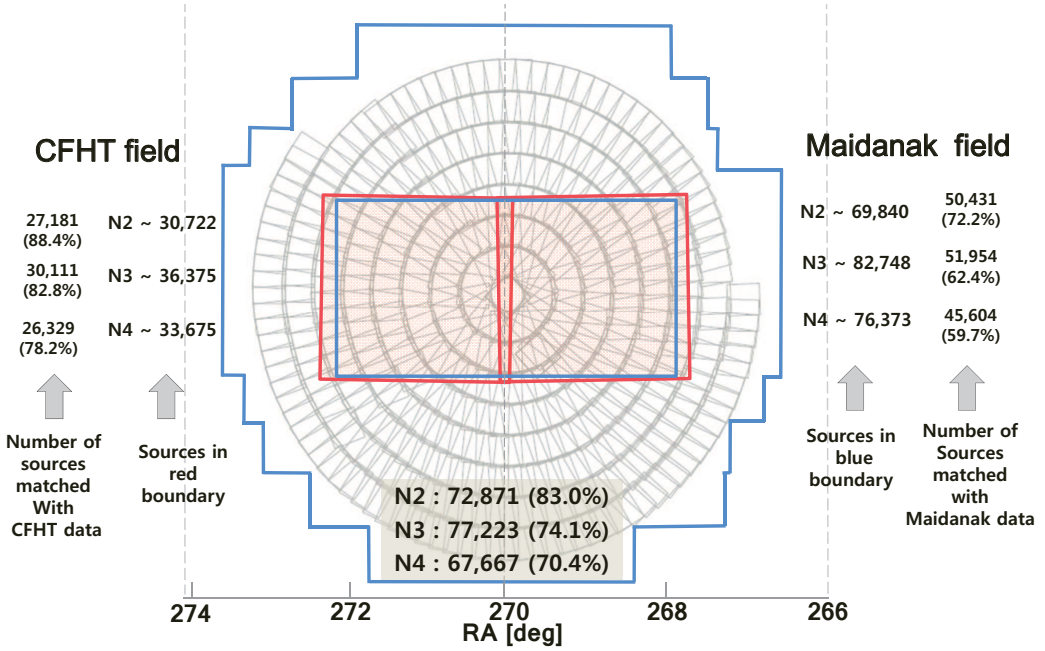

Figure 3.7 The matching results of AKARI sources against optical data covering two separate fields of CFHT and Maidanak observations. On the left and right of the diagram, the result with CFHT and with Maidanak data are presented, respectively. Overall matching results against both optical data are given in the bottom of the figure.

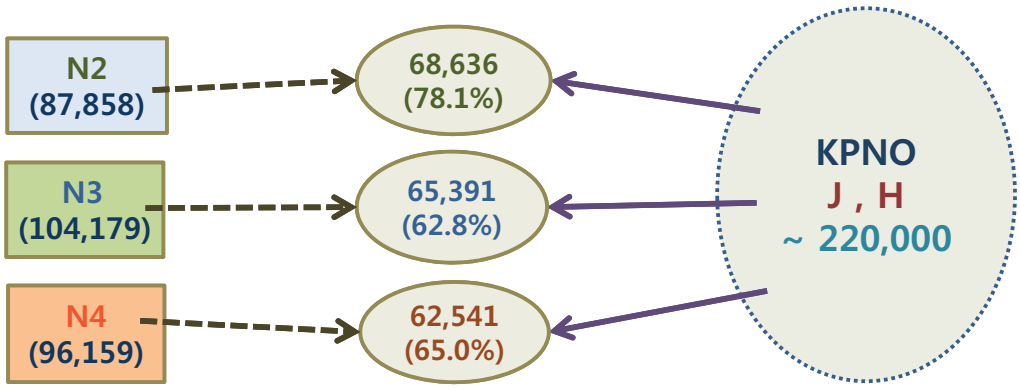

Figure 3.8 The number of sources in each of the NIR band matched with KPNO J, H band data. About 78%, 63%, and 65% of the $N2$, $N3$, and $N4$ sources were found to have their counterparts in J and H band data.

3.2 Point Source Catalog

3.2.1 Band-merging to catalog

After the source matching described above, we generated separate catalogues for nine IRC bands. At this point, each catalogue contained the photometric information from the other bands. We merged those catalogues step by step. As shown in Fig. 3.9, We made NIR band catalogue from the $N2$, $N3$, and $N4$ single band catalogues by cross-matching the sources, and where possible, with the optical data. MIR-S and MIR-L catalogues are also generated with the same method as that used for NIR catalogue. The final band-merging was based on NIR catalogue, and the sources in the MIR-S and MIR-L catalogues were compiled by matching of the entries using corresponding source IDs. For registered sources in the catalogue, if there is no detection in a certain band, we assigned the dummy value, 99.000. The NIR sources having no counterpart in any other bands are excluded to avoid the false objects caused by various artifacts. As explained in §4.2, however, we carried out careful eye inspection on individual images of MIR sources having no counterparts before the exclusion.

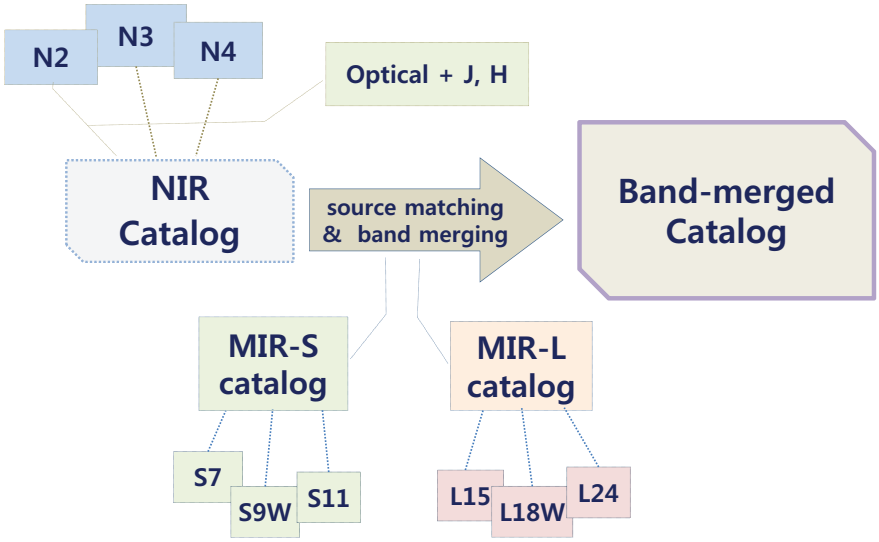

Figure 3.9 Schematic diagram describing the band merging procedure. we first combined the three catalogues of the NIR, MIR-S, and MIR-L channel. Then, we merged them into a band-merged catalogue covering from optical u^* to $L24$ band. During this procedure, we checked the source IDs carefully in order to avoid duplication of the same entries.

3.2.2 Catalog format

The number of sources in this final catalogue is about 114,800. In Table 3.2, a sample of the source catalogue is shown for the purpose of illustration. We give a short description of the columns in the catalogue.

Column (1): identification number of the sources.

Columns (2) and (3): J2000 right ascension (R. A.) and the declination of a source in decimal degrees. The coordinates are based on $N2$ astrometry. If there is no detection in the $N2$, the coordinates are based on the shortest wavelength identification.

Columns (4), (7), (10), (13), (16), (19), (22), (25), and (28): AB magnitudes of the sources in AKARI bands from $N2$ to $L24$ in AB magnitudes.

Columns (5), (8), (11), (14), (17), (20), (23), (26), and (29): uncertainty of the magnitude. They are RMS errors of the measured value.

Columns (6), (9), (12), (15), (18), (21), (24), (27), and (30): the photometric flags from the SExtractor. 0 - well isolated and clean image, 1 - the source has neighbors, about 10% of the integrated area affected, 2 - the object was blended with another one, 3 - 1+2, 4 - at least one pixel is saturated, 8 - object is truncated, close to the image boundary, -1 - no photometry (not detected)

Column (31): additional flag giving a caution for NIR photometry. (this indicates partially damaged sources during the cosmic-ray rejection, masking of MUX-bleeding, and etc.) 2 - for $N2$, 3 - for $N3$, 4 - for $N4$

For the matching results with optical data, we present the magnitude, magnitude error and stellarity information. In addition, the number of matched optical sources and the positional deviation of optical source from the AKARI WCS are included.

Columns (32), (34), (36), (38), (40): magnitudes in u^*, $g^{'}$, $r^{'}$, $i^{'}$, $z^{'}$ from CFHT data

Table 3.2a. NEP-Wide Infrared Point Source Catalogue[a]

ID	RA	Dec	- N2 -			- N3 -			- N4 -			- S7 -			- S9W -			- S11 -			- L15 -			- L18W -		
num	[deg]	[deg]	[mag]	[err]	[flg]	[mag]	[err]	[flg]	[mag]	[err]	[flg]	[mag]	[err]	[flg]	[mag]	[err]	[flg]	[mag]	[err]	[flg]	[mag]	[err]	[flg]	[mag]	[err]	[flg]
(1)	(2)	(3)	(4)	(5)	(6)	(7)	(8)	(9)	(10)	(11)	(12)	(13)	(14)	(15)	(16)	(17)	(18)	(19)	(20)	(21)	(22)	(23)	(24)	(25)	(26)	(27)
3	266.59579	66.47150	19.928	0.066	0	99.000	99.000	-1	99.000	99.000	-1	99.000	99.000	-1	99.000	99.000	-1	99.000	99.000	-1	99.000	99.000	-1	99.000	99.000	-1
7	266.59860	66.55494	99.000	99.000	-1	17.690	0.013	0	99.000	99.000	-1	18.095	0.073	0	18.500	0.118	0	19.031	0.164	0	99.000	99.000	-1	99.000	99.000	-1
18	266.60712	66.53683	19.594	0.051	0	19.073	0.035	2	19.713	0.058	0	99.000	99.000	-1	99.000	99.000	-1	18.755	0.145	0	99.000	99.000	-1	99.000	99.000	-1
296	266.73248	66.44641	19.057	0.037	3	19.440	0.044	2	18.832	0.029	2	18.218	0.065	0	99.000	99.000	-1	17.346	0.067	0	99.000	99.000	-1	99.000	99.000	-1
520	266.79562	66.14382	17.934	0.020	0	18.088	0.018	2	18.502	0.023	0	18.697	0.081	0	16.887	0.043	0	17.081	0.042	0	17.563	0.098	0	17.385	0.067	0
9509	267.66681	65.92631	14.171	0.003	0	14.694	0.003	0	15.335	0.003	0	16.319	0.019	0	16.029	0.022	0	17.089	0.044	0	99.000	99.000	-1	99.000	99.000	-1
24706	268.54489	67.36521	17.518	0.015	0	17.931	0.017	0	18.331	0.021	0	17.333	0.042	0	15.877	0.021	0	16.252	0.024	0	16.555	0.040	0	16.685	0.038	0

[a]This table contains only a subset of NEP-Wide sources. The complete version of the catalogs is in the electronic edition of the Journal. Band merged catalog of AKARI/NEP-Wide sources. Col. (1): ID number. Col. (2)-(3): Coordinates, R.A. and Dec. based on N2 astrometry. Col. (4)-(30): the IRC photometric information of the sources. For each band, magnitudes, magnitude errors and flags are presented.

Table 3.2b. NEP-Wide Infrared Point Source Catalogue[b]- continued from the previous table

ID	- L24 -			N_flg	u^*		g'		r'		i'		z'		B		R		I		stell	# of src	$\Delta\theta$
num	[mag]	[err]	[flg]	[flg]	[mag]	[err]	[mag]	[err]	[mag]	[err]	[mag]	[err]	[mag]	[err]	[mag]	[err]	[mag]	[err]	[mag]	[err]			
	(28)	(29)	(30)	(31)	(32)	(33)	(34)	(35)	(36)	(37)	(38)	(39)	(40)	(41)	(42)	(43)	(44)	(45)	(46)	(47)	(48)	(49)	(50)
3	99.000	99.000	-1	0	99.000	99.000	99.000	99.000	99.000	99.000	99.000	99.000	99.000	99.000	99.000	99.000	22.310	0.170	20.570	0.070	0.460	1	1.146
7	99.000	99.000	-1	0	99.000	99.000	99.000	99.000	99.000	99.000	99.000	99.000	99.000	99.000	19.780	0.040	17.730	0.040	16.550	0.020	0.980	1	2.053
18	99.000	99.000	-1	0	99.000	99.000	99.000	99.000	99.000	99.000	99.000	99.000	99.000	99.000	99.000	99.000	21.470	0.160	20.570	0.150	0.180	1	0.341
296	99.000	99.000	-1	0	99.000	99.000	99.000	99.000	99.000	99.000	99.000	99.000	99.000	99.000	99.000	99.000	99.100	99.000	20.850	0.120	0.010	1	1.072
520	99.000	99.000	-1	0	99.000	99.000	99.000	99.000	99.000	99.000	99.000	99.000	99.000	99.000	99.000	99.000	99.100	99.000	21.360	0.110	0.190	1	2.552
9509	99.000	99.000	-1	0	99.000	99.000	99.000	99.000	99.000	99.000	99.000	99.000	99.000	99.000	14.230	0.030	13.940	0.010	13.440	0.030	1.000	1	0.515
24706	16.661	0.079	-1	0	99.000	99.000	99.000	99.000	99.000	99.000	99.000	99.000	99.000	99.000	19.800	0.050	18.650	0.040	18.270	0.030	0.030	1	0.592

[b]This table is continued from the previous table and contains only a subset of NEP-Wide sources. The complete version of the catalogs is in the electronic edition of the Journal. Col. (32)-(41): CFHT Megacam u*, g′, r′, i′, and z′ magnitudes from Hwang et al. (2007) that are matched with AKARI/NEP-Wide sources. Col. (42)-(47): Maidanak B, R, and I magnitudes from Jeon et al. (2010). Col. (48): stellarity parameter from two optical data. Col. (49): the number of optical counterparts within3″. Col. (50): the angular separation of the optical counterpart from the position of AKARI source.

Columns (33), (35), (37), (39), (41): the magnitude errors in u^*, g', r', i', z'

Columns (42), (44), (46): magnitudes in B, R, I from Maidanak data

Columns (43), (45), (47): magnitude errors in B, R, I

Column (48): stellarity information from optical data. Note that the stellarity values of CFHT data were measured from the g', r', i', z' combined image (Hwang et al., 2007) and those of Maidanak were determined from the R- band image due of the highest S/N (Jeon et al., 2010). If a sources is matched with both CFHT and Maidanak data, we used the stellarity from CFHT data.

Column (49): number of optical sources matched to an AKARI source. For the multiply matched sources, this is larger than 1.

Column (50): distance between the astrometric coordinates of AKARI and optical data in arcsec. When an AKARI source is matched to optical data more than once (that is, column (49) $>$ 1), we chose the smallest number (the value of the closest one).

3.3 Nature of the sources

The point sources in NEP-Wide catalogue are mostly either stars or galaxies. In high resolution optical images, galaxies appear as extended sources unless they are very far or very compact while stars appear as point sources whose images follow the point spread function of the instruments. However, AKARI's images of distant galaxies cannot be easily distinguished from those of stars because of relatively large PSFs. In many cases, the nature of the sources can be identified by their spectral energy distributions (SEDs).

In contrast to the infrared images, the ground based optical images have much smaller PSFs, allowing easy distinction between point and extended sources. In particular, the optical data for NEP-Wide are all taken with excellent seeing conditions. Both CFHT and Maidanak data have typical FWHM size of PSF smaller than 1 arcsecond. The stellarity parameter given by the SExtractor thus can be used to distinguish between point and extended sources, as shown in Fig. 3.10. The sources with stellarity parameters close to 1 are point-like sources while those with values close to 0 are the extended sources. Although the stellarity parameters are spread all over the possible range between 0 and 1, there is a clear dichotomy, unless the sources become too faint. For the following discussion, we selected the high stellarity sources using an optical stellarity parameter (> 0.8) and an $r^{'}$ band magnitude cut (< 19) and designated them as star-like objects.

Stellar SEDs are usually determined by the surface temperature and the atmospheric metal abundances. Since the stellar surface temperature is usually higher than 3000K, the infrared parts of stellar SEDs can be approximated by the Rayleigh-Jeans spectrum. Thus we expect the stars will contribute less as the wavelength becomes longer. However, infrared properties can often be modified by the presence of circumstellar material. Some stars with large amounts of circumstellar material could be bright even in some MIR bands.

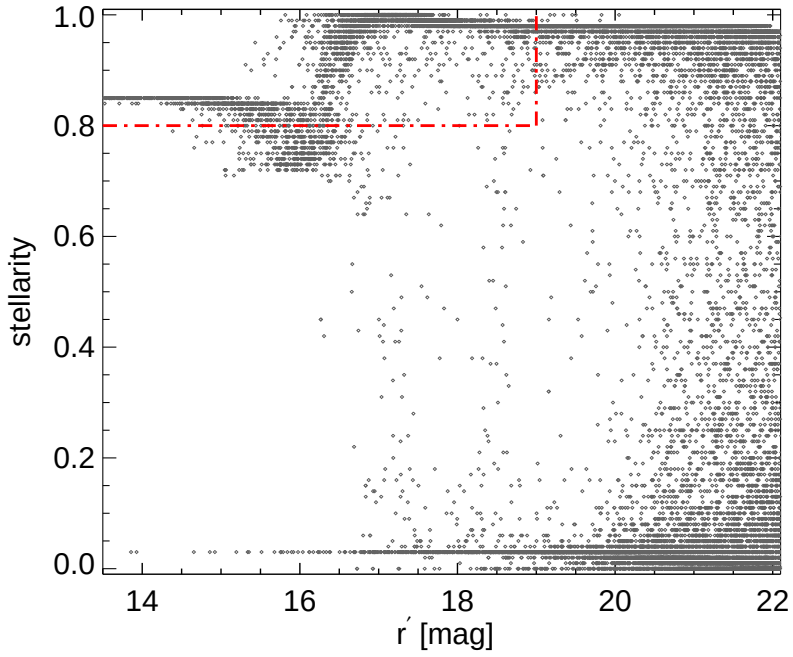

Figure 3.10 The stellarity parameter as a function of $r^{'}$ band magnitude derived from CFHT data. It can be clearly seen that the stellarity parameters are mostly either close to 1 or 0 unless the sources become very faint. Note that the sources brighter than 16 mag have relatively smaller stellarity because central parts of their images are saturated. We designated the sources with stellarity greater than 0.8 and brighter than 19 mag as 'star-like' sources that are likely to be stars.

Galaxies emit significant amounts of radiation in infrared. SEDs of galaxies strongly depend on galactic types and star formation rates (e.g., Polletta et al. 2007). Since our catalogue covers wide range in wavelengths, the SED fitting of individual could provide useful information on the nature of them. However, dealing with individual sources is beyond the scope of present chapter. Here we provide only general and statistical comments on the composition of the sources.

3.3.1 Number counts and the source matching ratio

We present number counts for each band and the cross-matching rate of the sources against optical data, and the other bands as a function of magnitude. Fig. 3.11 shows the results for the NIR bands. The top panels show the number counts of NIR band sources which are confirmed through the cross checking process with the other bands. The $N2$ sources brighter than 12.6 mag were excluded during the data reduction process because they are heavily saturated and generate MUXbleeds.

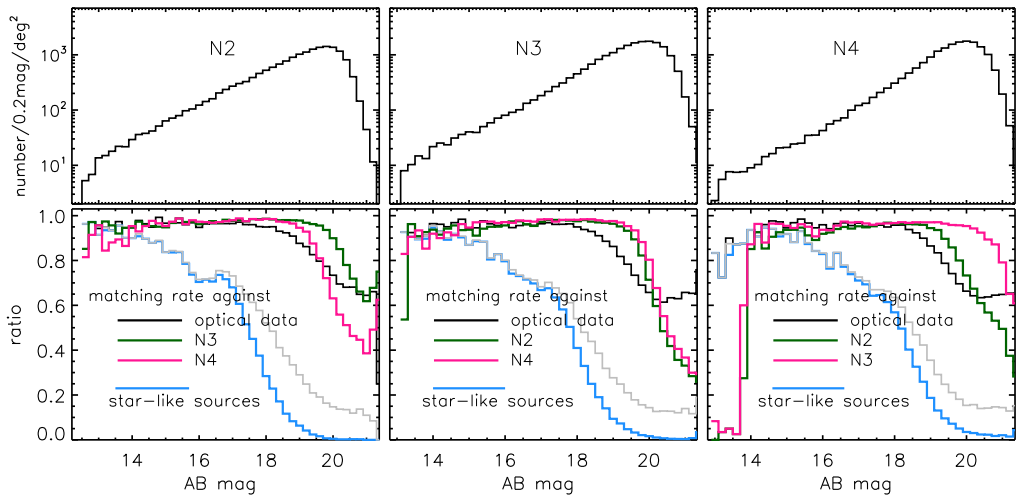

Figure 3.11 The source counts of NIR bands and the matching ratio against optical and other NIR bands. Top panels show the distribution of sources as a function of magnitude per square degree per 0.2 magnitude bin. In the lower panels, the matching ratio against those in other NIR bands and optical data are presented together.

We found that the sources having no counterparts in the other data are mostly fainter than 19 mag in the $N2$ band. And, most of the false objects at bright magnitudes turned out to be residual streaks around bright stars through visual inspection of the image. On the other hand, in the fainter magnitudes, most of the false objects

close to the detection limits are due to noises because the comparison of common areas of NEP-Deep and NEP-Wide show that many of these faint sources do not appear as real sources in NEP-Deep whose detection limits are more than 1 mag deeper.

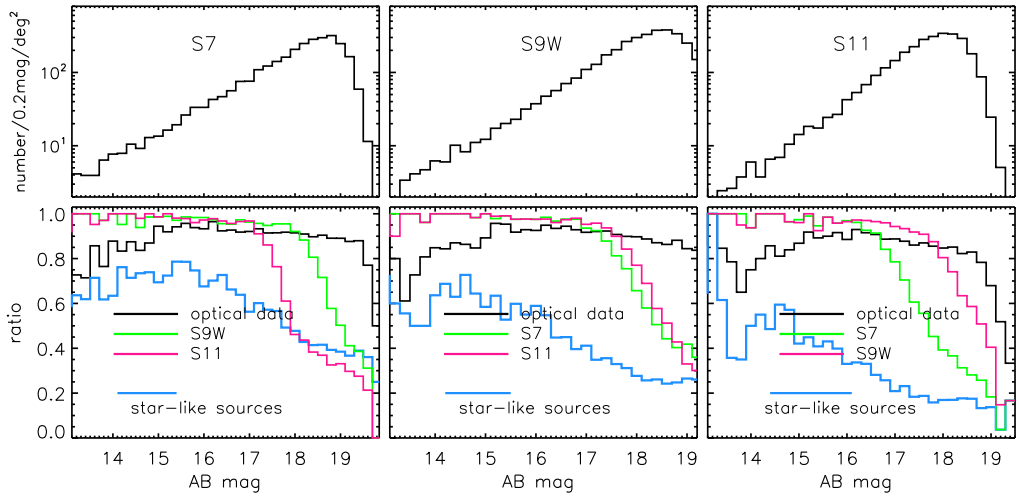

Figure 3.12 Same as Fig. 3.11, but for the MIR-S band sources. The top panel shows the number of sources per square degree per 0.2 mag bin as a function of magnitude. In the lower panel, the matching rates of the sources against those in the other MIR-S bands and the optical data are presented together with the fraction of the star-like sources.

In the lower panel, we showed the matching ratios against the optical, and other two NIR bands data separately. The fraction of sources for which the stellarity greater than 0.8 without any constraint on magnitude are indicated by the gray line in this panel. The fraction of star-like objects that are defined as those with optical stellarity greater than 0.8 and r magnitude brighter than 19 are shown as blue dotted lines. Using the optical-IR SEDs of these objects, we confirmed that most of the star-like objects closely follow black body spectra, suggesting that they

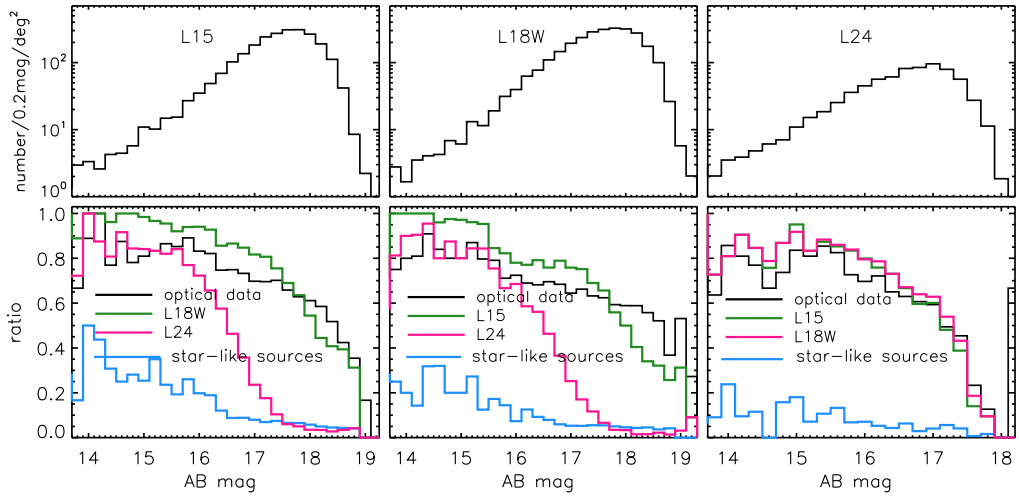

Figure 3.13 Same as Fig. 3.11, but for the MIR-L band sources.

are indeed likely to be stars. Fig. 3.11 thus suggests that the sources brighter than 14 mag in the $N2$ band are mostly stars even though the actual number of them is small. The fraction of high stellarity objects rapidly decreases around the 17 mag, and completely falls off to zero toward $\sim$ 20 mag. The features in the $N3$ and $N4$ band are generally similar to those in the $N2$ band. The properties of these objects in color-color diagrams are discussed in the following section. The overall fraction of star-like objects among the entire $N2$ sources are about 17%. In the $N3$ and $N4$ bands, these fractions are about 15% and 16%, respectively.

The same analysis was conducted for the MIR bands and the results are shown in Fig.3.12 (MIR-S) and 3.13 (MIR-L). The numbers of sources detected in the MIR bands are much smaller than those in the NIR bands. Compared to the NIR bands, the high stellarity sources are not the main contributors in all magnitudes. The fraction of them decreases significantly in the longer wavelength bands. But they do not show the rapid decline or complete downfall to zero in the fainter region.

Overall, about 22% of the entire NIR and 20% of the MIR sources do not have

optical counterparts within a $3^{''}$ radius, while there are multiple optical counterparts for some sources. This multiple matching was most serious between the optical and MIR band sources. We found multiple optical counterparts for about 17% of the MIR sources during the MIR band merging. In these cases, we tried to identify the proper counterparts using the optical sources that had NIR counterparts from AKARI or in the J, H bands. Through this process, we were able to assign the reliable counterparts with confidence. Despite this, the nearest neighbor does not seem to be the most likely optical counterpart for about ($\sim 3\%$) of the MIR sources. In those cases, we visually inspected the images, although this provided little help. In the final catalog, all of the optical counterparts are indeed those found to be the nearest neighbors.

3.3.2 Color-Color and Color-Magnitude diagrams

It is not easy to clearly identify the nature of the sources with AKARI data alone. We attempted to distinguish different types of sources using various color-magnitude and color-color diagrams (CCDs). The star-like sources are plotted with red colors in each color-color diagram from Fig. 3.14 to 3.17. The color-color diagrams for three NIR bands of AKARI are shown in Fig. 3.14.

The majority of the star-like sources lie in the narrow range of colors of $-0.7 < (N2 - N3) < -0.4$, $-1.5 < (N2 - N4) < -1.0$ and $-0.9 < N3 - N4 < -0.4$. The sources with stellarity greater than 0.95, magnitudes in the range $14.5 < r < 17.5$ and identified as stellar sources by the inspection of their images and SEDs are overplotted with dark red. We also present various optical - NIR color-color diagrams in Fig. 3.15.

The star-like sources form a tight sequence in the $(g^{'} - z^{'})$ versus $(u^{'} - r^{'})$ color-color diagram and they are located along the lower right edge. On the other hand, extended sources are more widely spread and occupy the entire region above the

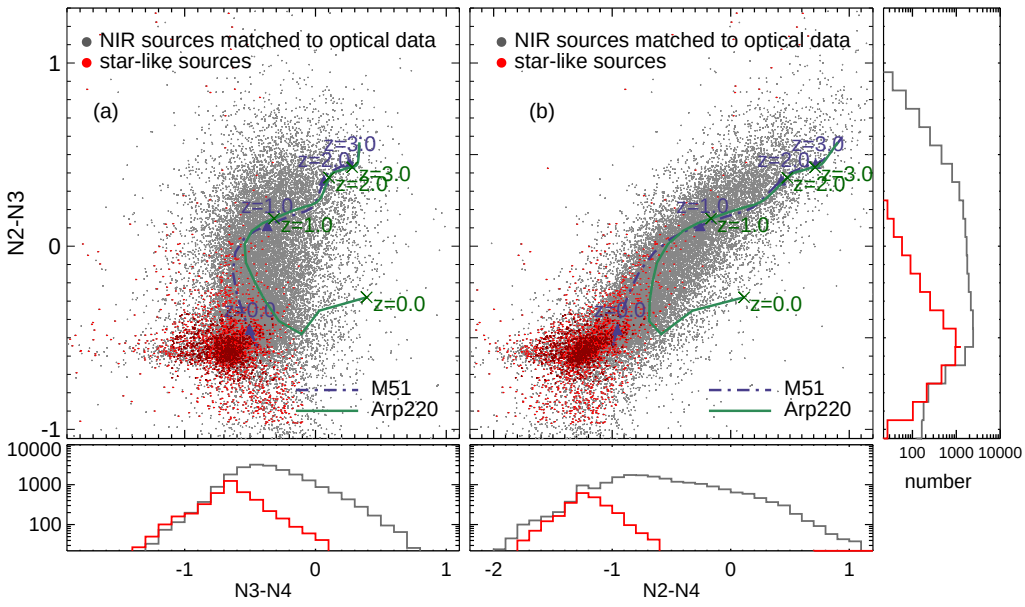

Figure 3.14 The color-color diagrams (CCDs) of the NEP-Wide NIR sources matching with optical data. (a) $(N2-N3)$ vs. $(N3-N4)$ color and (b) $(N2-N3)$ vs. $(N2-N4)$ color. Dark dots represent all of the sources having optical counterparts and red dots represent the star-like sources defined by the stellarity > 0.8 and $r^{'}$ < 19. The histograms in the right and the lower panels show the number of sources per 0.2 magnitude bin.

stellar source sequence. In the $(R-I)$ versus $(B-R)$ diagram, however, the stellar sequence is somewhat broader and runs across the broader region occupied by the extended source. The NIR colors such as $(J-H)$ and $(H-N2)$ are also useful to distinguish the stars from galaxies (extended sources) as shown in the lower panels of Fig. 3.15. The $(J-N2)$ color was not shown here but it is similar to the $(H-N2)$ color. The $N2$ vs. $(H-N2)$ color-magnitude diagram (CMD) in the last panel shows that the star-like sources are the brightest ones in the $N2$ band. By comparing these

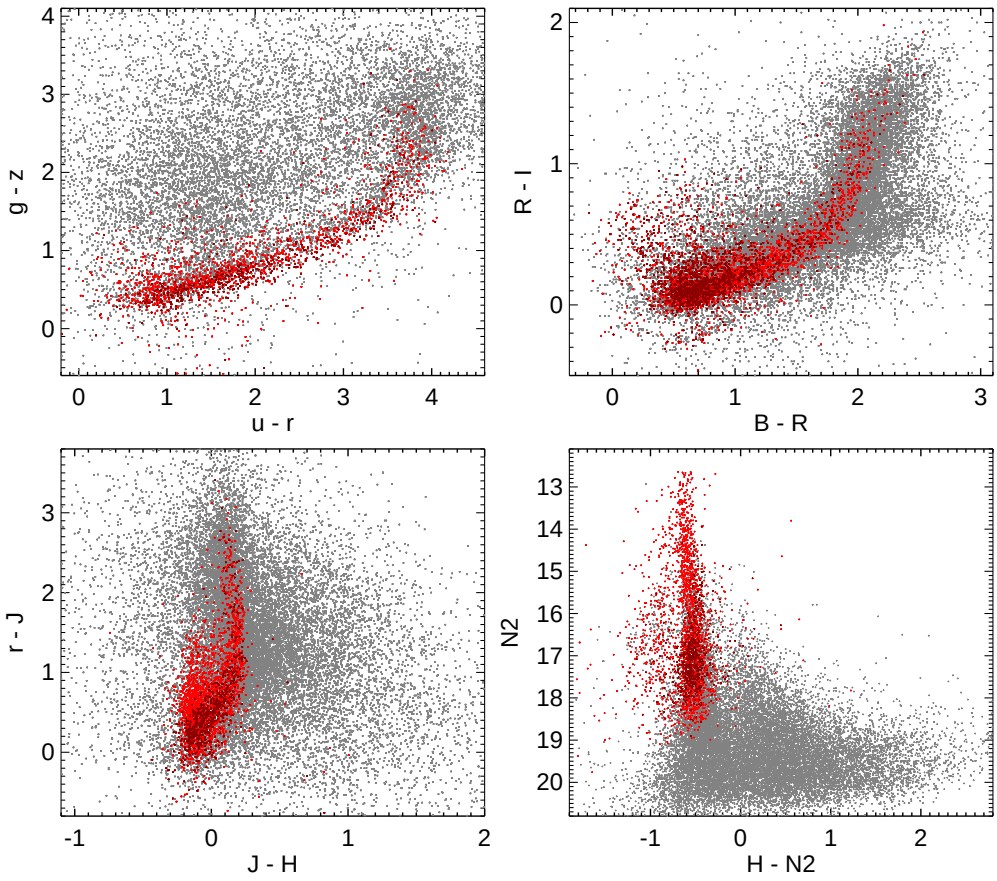

Figure 3.15 The color-color diagrams (CCDs) and color-magnitude diagram (CMD) of the NEP-Wide sources matching with optical data. They show the various colors by optical bands from CFHT and Maidanak and near-IR J, H bands. Red dots represent the star-like sources defined by the stellarity > 0.8 and $r^{'} < 19$.

properties in color-color plots, we can separate stars effectively, even though we can not identify all stars individually. The diagrams show that high-stellarity sources are statistically good indicator for the selection of the stars although the criterion is not perfect to identify all the stars.

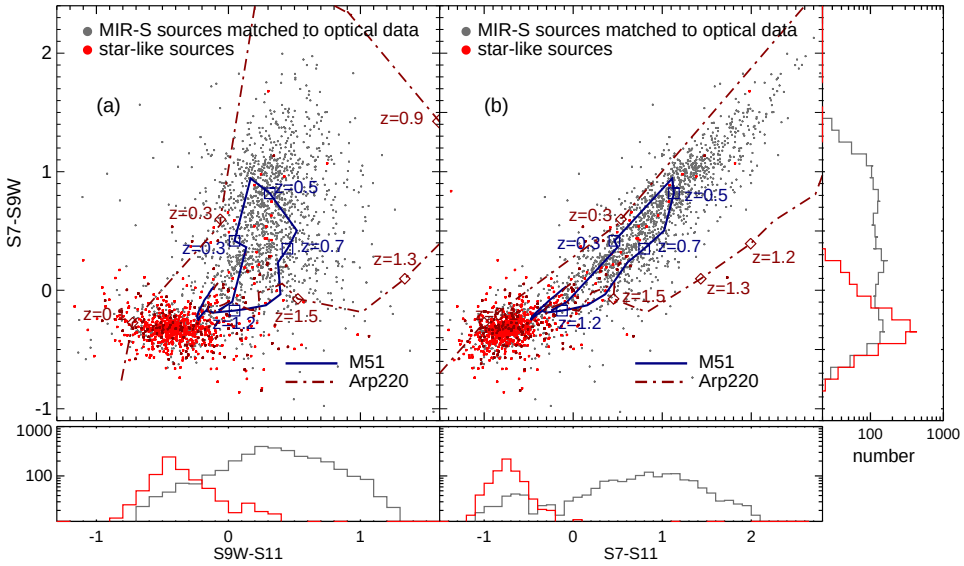

Figure 3.16 The color-color diagrams (CCDs) of the NEP-Wide MIR sources matching with optical data. (a) $(S7 - S9W)$ vs. $(S9W - S11)$ and (b) $(S7 - S9W)$ vs. $(S7 - S11)$ CCDs. All of the MIR sources having optical counterparts are presented using dark dots in the diagrams Among them, the star-like sources defined as those with stellarity greater than 0.8 are plotted in red color.

The colors of galaxies provide us with valuable information about their composition and history (Fukugita et al. 1995). However, unlike point sources, extended sources show widely spread across the color-color diagrams as shown in Fig. 3.14 – 3.17. In Fig. 3.14, we have plotted the redshift tracks of the templates (Silva et al. 1998) of the star-forming galaxy M51 and the typical ultra-luminous infrared galaxy (ULIRG) Arp220 over the diagrams. Compared to these tracks, we find that the NEP-Wide sources are located close to the redshift sequence, although the scatter is quite large. This could mean that the galaxy SEDs are quite diverse, but in addition, a large fractions of the NEP-Wide sources are star forming galaxies at dif-

ferent redshifts. About 70% of the MIR-selected sources in AKARI's early data were identified as star forming galaxies through the detailed inspection of their infrared SEDs (Lee et al. 2007). Since the NIR parts of the SEDs of star-forming galaxies are dominated by late-type stars and thus rather homogeneous, the NIR colors are mostly determined by the galaxy redshifts. The histograms show the distribution of the source density in each 0.1 magnitude bin. We also note that many sources are located quite far away from the star forming galaxy sequence. Some of these sources with very red NIR colors are likely to be active galactic nuclei (AGNs) (Lee et al. 2007).

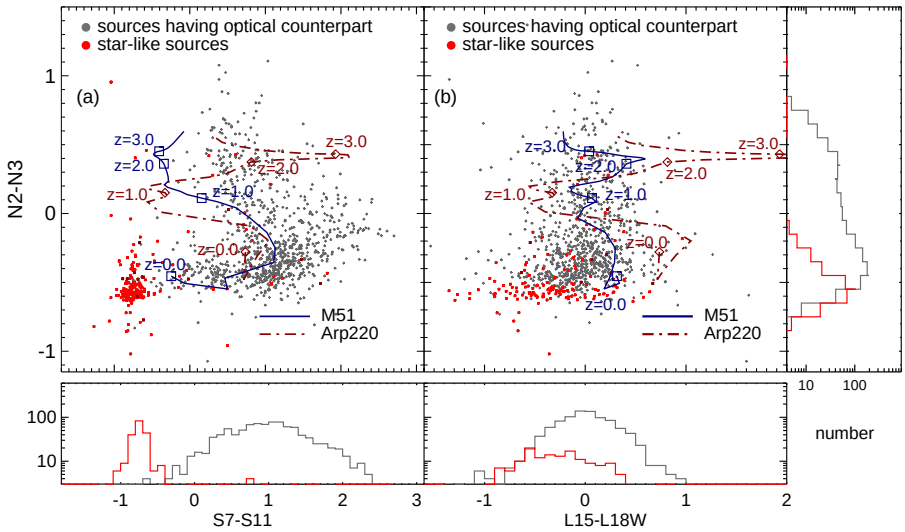

Figure 3.17 (a) $(N2-N3)$ vs. $(S7-S11)$, and (b) $(N2-N3)$ vs. $(L15-L18W)$ CCDs. The NEP-Wide sources whose optical stellarities are known by cross- matching with optical CFHT and Maidanak catalogues are presented using dark dots in the diagrams. Among them, the star-like sources are plotted in red color.

In Fig. 3.16 and 3.17, we show the diagrams using the colors for the MIR bands, for which, the NEP-Wide sources appear to have a much wider distribution. As for

the sources used in the previous color-color diagrams, optically matched sources are presented with gray colors and the star-like sources are plotted with red colors. As shown in these figures, the MIR-S color-color diagrams ($S7 - S9W$), ($S7 - S11$) and ($S9W - S11$) show that the star-like sources are well segregated from the other sources, but this feature gradually disappears in the longer wavelength band colors. Most of the stars (and the early type galaxies) detected in the NIR bands seem to fade out in the MIR bands. Unlike the NIR and MIR-S band colors, the MIR-L band colors do not seem to be helpful in classifying stars since the MIR-L band color-color diagrams do not show any prominent features. The variation in the NIR colors are mainly due to the wide range of galaxy redshift, while the MIR colors are sensitive to the star formation rates, causing the wide spread in the MIR color-color diagrams. The number of sources detected in all IRC bands is about 1,000 and most of them seem to be late-type star forming galaxies. Many of these are identified as disk galaxies by the visual inspection of the optical images, and from their optical–IR SEDs. They are not located in a particular region and occupy a large area in the color-color diagrams. However, various interesting sources seem to be included in the all-band detected sources. Bright sources in the MIR-L bands that have radio counterparts are likely to be AGNs (Lee et al., 2009). We found that many of them show a power law distribution of SEDs while some show PAH bumps (Takagi et al., 2010). Dozens of sources are bright (< 17 mag) in either the $L18W$ or $L24$ band and have faint optical ($r^{'}$ or R) counterparts, seemingly suspected to be dust obscured galaxies (DOGs), a class of high-redshift ULIRGs. There are no sources with high-stellarity associated with faint MIR-L sources. In addition, the MIR-L sources detected in only one band, having no counterparts in our other data sets seem possibly to be very red objects.

Chapter 4

Mid-infrared Luminosity Function of Local Galaxies

4.1 Introduction

The Luminosity Function (LF), denoted by $\Phi(L)$ (in units of $erg\ s^{-1}Mpc^{-3}$), is one of the fundamental tools to probe the distribution of galaxies over cosmological time. The definition of the luminosity function of galaxies follows those of other astronomical objects such as stars or globular clusters. It is the number of sources that exist in a given volume of space having a given luminosity. Therefore, LF of galaxies describes the relative number of galaxies having different luminosities by counting them in a representative volume of the Universe. Astronomers have tried to quantify the nature of the evolution and large scale structure of galaxies by studying their luminosity distribution. Luminosity function is a useful measure to compare the difference between different set of galaxies, i.e., different types, at different redshifts and environments, thus, it allows us to analyze the statistical nature of galaxies.

Compared to the LF of cluster galaxies, the field LF is more difficult to measure because the galaxy densities are much lower than rich clusters (by a factor of 100 –

1000). Large volumes must be surveyed to obtain representative samples of objects. For this reason, astronomers usually consider panoramic and pencil-beam surveys with long integration time to reach low surface brightness galaxies. Naturally, estimation of luminosity function is one of top priority works after a certain survey is carried out and the catalogue of the survey is produced. Here, the 'luminosity' generally means a total magnitude measured in a certain photometric passband such as U, B, V, etc. By historical and classical reason in the LF studies, most of our knowledge has been largely based on the optical photometry. However, during the last decade which can be called 'an era of infrared astronomy', many studies utilized modern wide-field CCD cameras and infrared detectors (especially, equipped in IR satellites orbiting around the Earth), and astronomers were able to explore the LF of galaxies in various infrared bands out from under the optical wavelengths. Now the study of galaxy LFs is a vast subject area spanning a broad range of wavelengths.

Infrared wavelength is actually an important probe of galaxy activity since many studies suggest that significant amount of (at least about half) the luminous energy generated by stars has been reprocessed into the infrared wavelength by dust (Lagache et al. 1999; Puget et al. 1996; Frenceschini et al. 2008). Near-IR wavelengths may tell us about evolved stellar mass, while mid- and far-IR wavelengths may indicate when and where the observed starbursts occurred. The more intense the star forming activities are, the more embedded they are in the dust, which make it harder to observe in optical and ultraviolet (UV). It is also found that galaxies in infrared wavelength show remarkable property that dust-enshrouded starbursts seem to undergo evolution in luminosity and density up to about z $\sim$ 1, and that their evolutionary rate may exceed those measured at any other wavelengths, based on the IRAS data (Hacking et al. 1987; Franceshini et al. 1988; Saunders et al.1990; Fang et al. 1998 etc.) and ISO data (Elbaz et al. 1999; Puget et al. 1999). Therefore, it is vital to understand IR emission. In spite of the importance of the infrared observations,

the researches of galaxies by the IRAS and the ISO were restricted to bright sources by limited sensitivity (Saunders et al. Rowan-Robinson et al. 1997; Flores et al. 1999; Serjeant et al. 2004; Goto et al. 2010). Although earlier works have been hampered by sensitivity, area and identification difficulties (for submm), etc., IR LFs were constructed since the IRAS satellite mission (e.g., Rowan-Robinson, Helou, and Walker (1987) derived 25, 60 and 100 μm LFs). Saunders et al. (1990) used IRAS data to derive the 60 and 40–120 μm LFs. Clements, Desert and Franceschini (2001) used deep 12 μm ISO data with follow-up optical imaging and spectroscopy to determine the mJy 12 μm LF. Serjeant et al. (2004) used the optical–IR band-merged European Large Area Infrared Survey (ELAIS) Final Analysis Catalogue of Rowan-Robinson et al. (2004) to calculate the ELAIS 90 μm LF.

More recently, successful observations using *Spitzer* and AKARI satellite brought revolutionary results with improved sensitivities (Le Floc'h et al. 2005; Perez-Gonzaleze et al. 2005; Babbedge et al. 2006; Caputi et al. 2007. Goto et al. 2010; Rodighiero et al. 2010; Goto et al. 2011). They measured luminosity function in the mid-infrared bands from various fields and found a positive evolution in luminosity and density and increasing importance of the LIRGs and ULIRGs population as we move to high redshifts. In a sense of this context, it seems natural that many researches are interested in higher redshifts. On the other hand, however, understanding local universe is important because it is essential step to see the evolution as a function of time (or redshift). And high-redshift studies need a good comparison sample in the local universe around z= 0. In this study, the galaxies in the local universe are of interest.

Owing to an excellent visibility towards the ecliptic poles, AKARI successfully carried out extragalactic survey on the north ecliptic pole (NEP) with the continuous wavelengths bands from 2 to 24 μm, filling the wavelength gap between *Spitzer* IRAC and MIPS. Taking advantage of this wide field survey with the wavelength coverage, we can construct mid-IR luminosity function of local galaxies if we use accurate

redshift information. We hope that analysis of this NEP-Wide data will contribute to building a comprehensive understanding of local population. The depth of the NEP-Wide survey is rather shallower (much lower than $z \sim 1$, in general) compared to the NEP-Deep survey, but larger area seems more adequate to collect various and many local galaxy samples.

4.2 Galaxy sample

In order to investigate the nature of extragalactic sources such as luminosity function or star formation rate (SFR) etc., accurate redshifts information is necessary. After the NEP-Wide survey was finished, the NEP-team (Im et al.) carried out follow-up spectroscopic survey over the entire AKARI NEP-Wide field, in order to obtain the spectroscopic redshift (spec-z) data. The observations were performed using MMT/Hectospec and WIYN/Hydra (Ko et al. 2012; Shim et al. *in prep.*). The main targets for this observation were star-forming galaxies (SFG) selected based on the criteria by the IRC colors and magnitudes (ex. $S11 < 18.5$, $L15 < 17.9$, etc.) including optical (CFHT and Maidanak) stellarity. Also power law SEDs as active galactic nuclei (AGNs) candidates were selected based on the color criteria of near-IR (NIR) and mid-IR (MIR) bands ($N2 - N4 > 0$ and $S7 - S11 > 0$). Various types of galaxies such as radio sources (White et al. 2010), PAH-luminous galaxies (Ohyama et al. 2009; Takagi et al. 2010), and optical drop-outs were also included in the targeting criteria. (for detailed information, see Ko et al. 2012; Shim et al. *in prep.*)

We constructed a spectroscopic sample (spec-z sample) catalog by matching this spectroscopic data with the final NEP-Wide catalogue (Kim et al. 2012), which will be used to process further works. And, to this catalog, we were able to add 240 sources whose redshifts were available from the NASA Extragalactic Database (NED) (Ko et al. 2012). All the sample have the quality flags representing the

reliability for the redshifts. This catalogue contained about 1,940 sources, but we did not use about 400 sources because their spectroscopic redshifts are unreliable (quality flag < 2.5).

The spatial distribution of the spectroscopic sample is shown in Fig. 4.1 The blue crosses indicate the spectroscopic targets observed using Hectospec, and the red boxes show the sources observed using WYIN. We also show the redshift distribution of our sample in Fig. 4.2. All the spec-z sources in our spectroscopic sample catalog are shown with gray line. The black line shows the distribution of our spectroscopic sample having a reliable redshift (quality flag > 2). The blue color indicate the sample observed using Hectospec, and the red color represents those observed using WYIN. Most of the sources ($\sim 85\%$) have lower redshift ($z < 0.8$). The distribution of the sample with high redshifts (> 1) is shown in an inner small box.

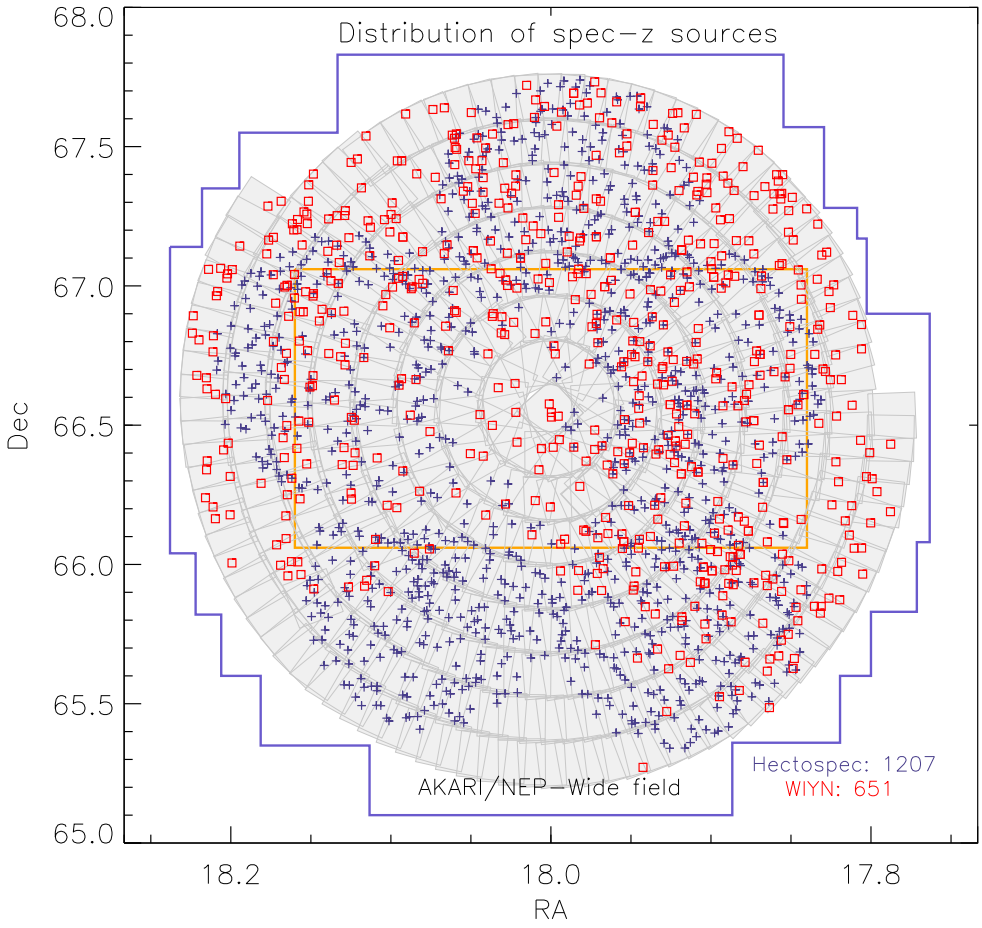

Figure 4.1 The spatial distribution of spec-z sources obtained by follow-up spectroscopic observations over the NEP-Wide field. The blue crosses indicate the spectroscopic targets observed using Hectospec, and the red boxes show the sources observed using WYIN. The representation of the outer blue lines and an inner orange box are the same as Fig. 1.1

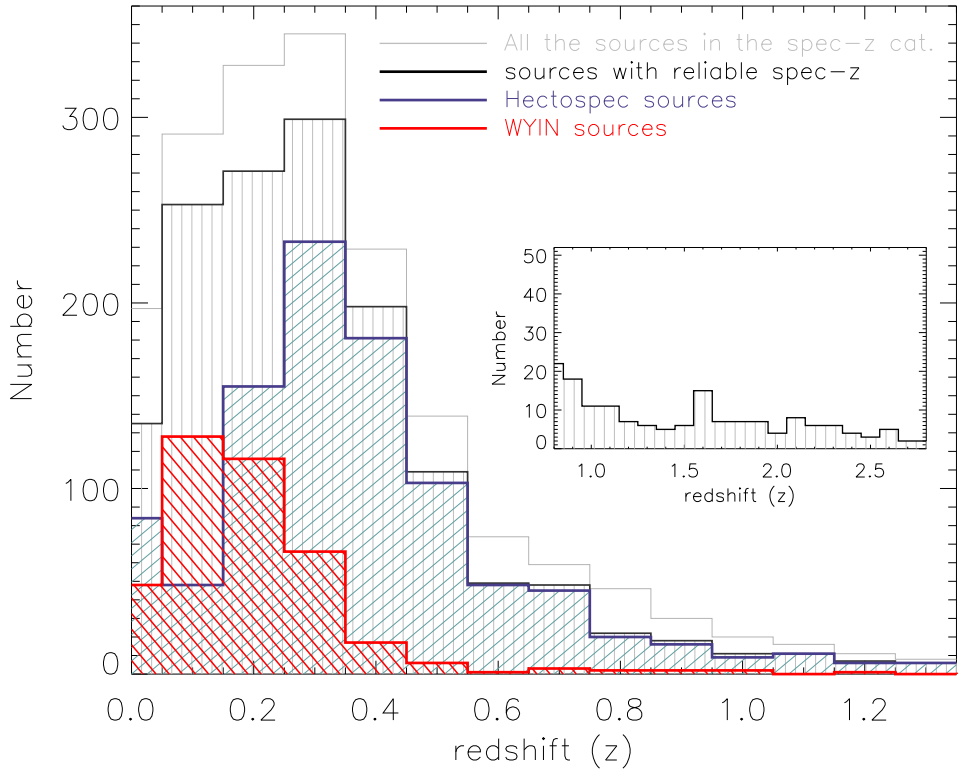

Figure 4.2 The number distribution of spec-z sources as a function of redshift. The black line shows the distribution of our spectroscopic sample having highly reliable redshift (quality flag > 2). The blue color indicate the sample observed using Hectospec, and the red color represents sample observed using WYIN. Most of the sample (85% fraction) have redshifts lower than 0.8.

4.3 SED fitting and SFG/AGN separation

In this work, we would like to focus on the MIR luminosity function of star-forming galaxies in the local universe (z< 0.3), and compare with other works. For the MIR luminosity, we have to be careful that different physical mechanisms contribute to the infrared emission. Galaxy emission, especially in the mid-infrared (approximately up to around ~ 11 μm), are the sum of the Rayleigh-Jean tail of stellar emission, heated dust emission, and a power-law component by accreting black holes. Therefore, to investigate the star-forming activity, we need to identify type of galaxies in our sample, which means that it is essential to separate AGNs from the star-forming (SF) components. However, this has been a very difficult task and one issue of debates over the decades. Galaxy SEDs in this range are very diverse because the proportion from each component vary widely, and the classification of the galaxy type is not straightforward. That is why many separation methods have been proposed, such as radio luminosity, optical line ratios, PAH strength, sub-millimeter properties and so on. Here, we do not have a complete diagnosis to carry out the way suggested above for our samples. But, as used for the target selection to carry out the spectroscopic follow-up on the NEP-Wide field, the NIR color (e.g., $N2-N4>0$) and MIR color ($S7-S11>0$) are known as good criteria for AGN selection (Lee et al. 2007; Lee et al. 2009; Shim et al. 2011; Ko et al. 2012). Among the spectroscopic sample, about 200 sources ($\sim 10\%$) are classified into AGN types by this method. However, this method does not seem to perfectly discriminate the sources because the type of the galaxies gradually change and the AGN types classified by this color could include some composite systems in which a fraction of the IR luminosity is actually due to star formation. Even if the sources are included in the color range of '$N2-N4<0$', it is not easy to assert that they are SF galaxies (SFG) because there are also AGN/composite types in the range close to $N2-N4=0$. Although majority of AGN sources are well classified, some SFGs are included in the AGN domain and

some of AGNs still reside in the $(N2-N4<0)$ range. For a few hundreds sources, it is not straightforward to judge whether it is AGN or SFG. We would like to exclude all of these confusing sources in order to use only SF component confidently in this analysis. We compared observed fluxes (from optical to mid-IR bands) with SED model templates, and investigated if the results can be used for this purpose (to exclude all these confusing sources).

We performed SED fitting of the spec-z samples. To find the best-fit model to the distribution of the observed fluxes, we utilized the publicly available code *Le PHARE* (Ilbert et al. 2006). Detailed specifics of the code are given in Ilbert et al. (2006). Using this software, the SED fitting was done over all the available photometric band with the spectroscopic redshift. We were able to compare the observed fluxes with all SED models of galaxies and AGNs/composites from Polletta et al. (2007) as well as SFGs including various stellar SED templates provided in the software. We searched for a best-fit model from SF galaxies, AGNs, and stars, and chose one template SED giving the minimum χ^2.

We present figure 4.3 showing the subset of our sample best-fit to Sc template. We also plotted SEDs of best-fit star and best-fit AGN just for comparison. The red lines represent the template SEDs of Sc from Polletta et al. (2007) adjusted to observed fluxes denoted by small squares. Different colors in those small square boxes indicate different wavelength bands from CFHT, Maidanak, J-, H-band, and from AKARI NIR, MIR-S, and MIR-L. In figure 4.4 and figure 4.5, we also show the examples fitted to M82 and Seyfert type 2 (Sey2) template from Polletta et al. (2007). On the other hand, these figures suggest that some sources are actually difficult to discriminate or determine their types exactly.

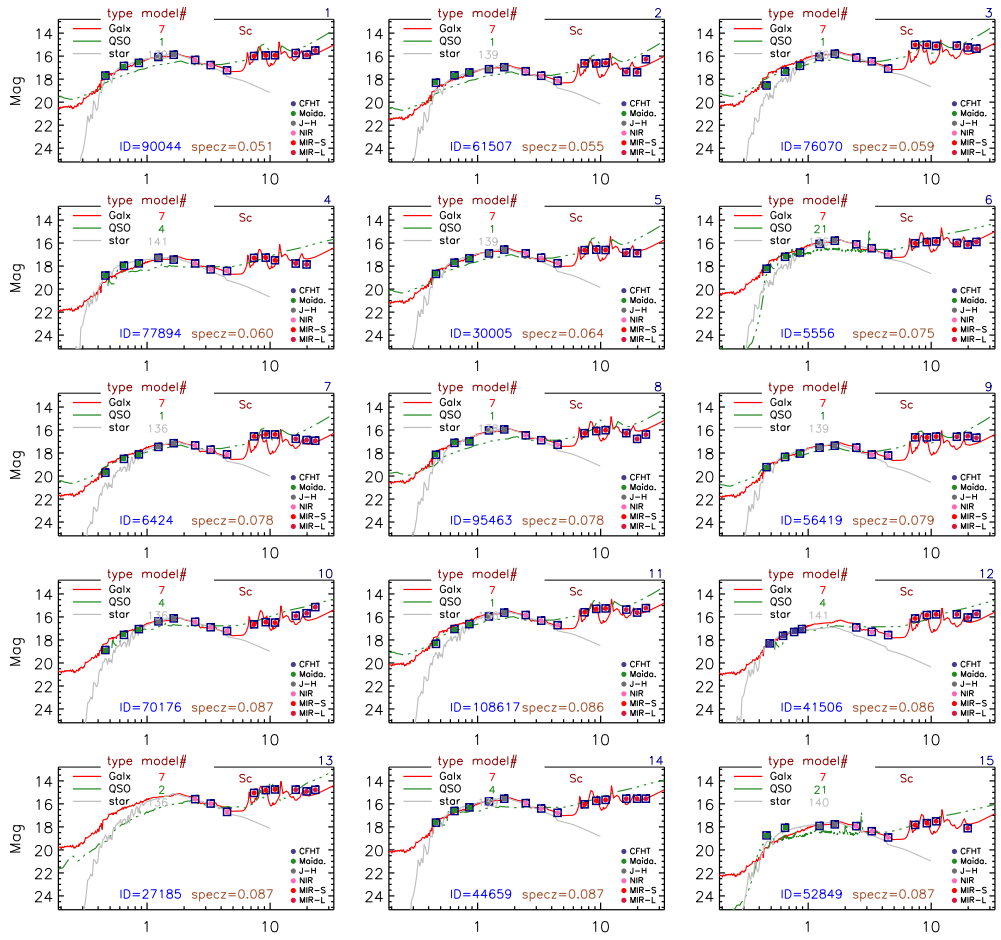

Figure 4.3 Examples of galaxies best-fit to Sc type galaxy. The observed fluxes from CFHT u* band to AKARI L24 band are presented by small squares. Overplotted red lines represent the Sc template from Polletta (2007). We also plotted SEDs of best-fit star and AGN with Sc template just for comparison.

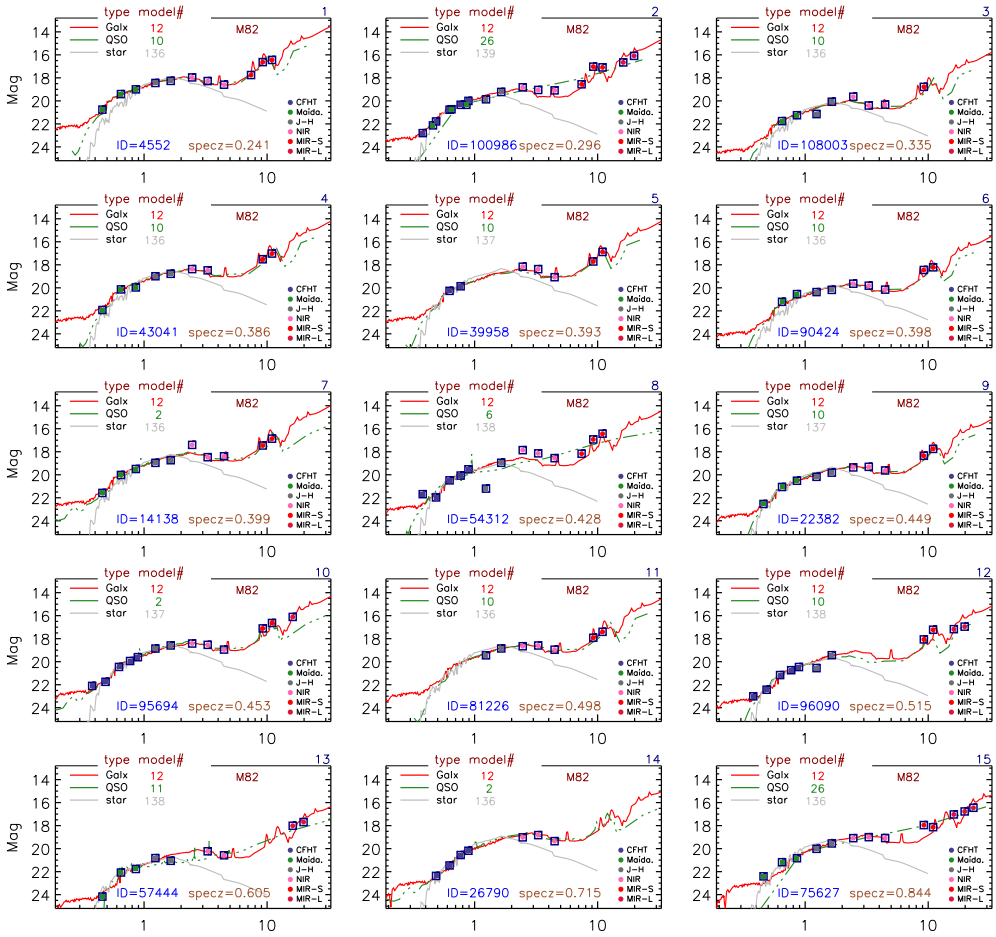

Figure 4.4 Examples of galaxies best-fit to M82 template. The observed fluxes from CFHT u* band to AKARI L24 band are presented by small squares. Overplotted red lines represent the M82 template. We also plotted SEDs of best-fit star and AGN with M82 template just for comparison.

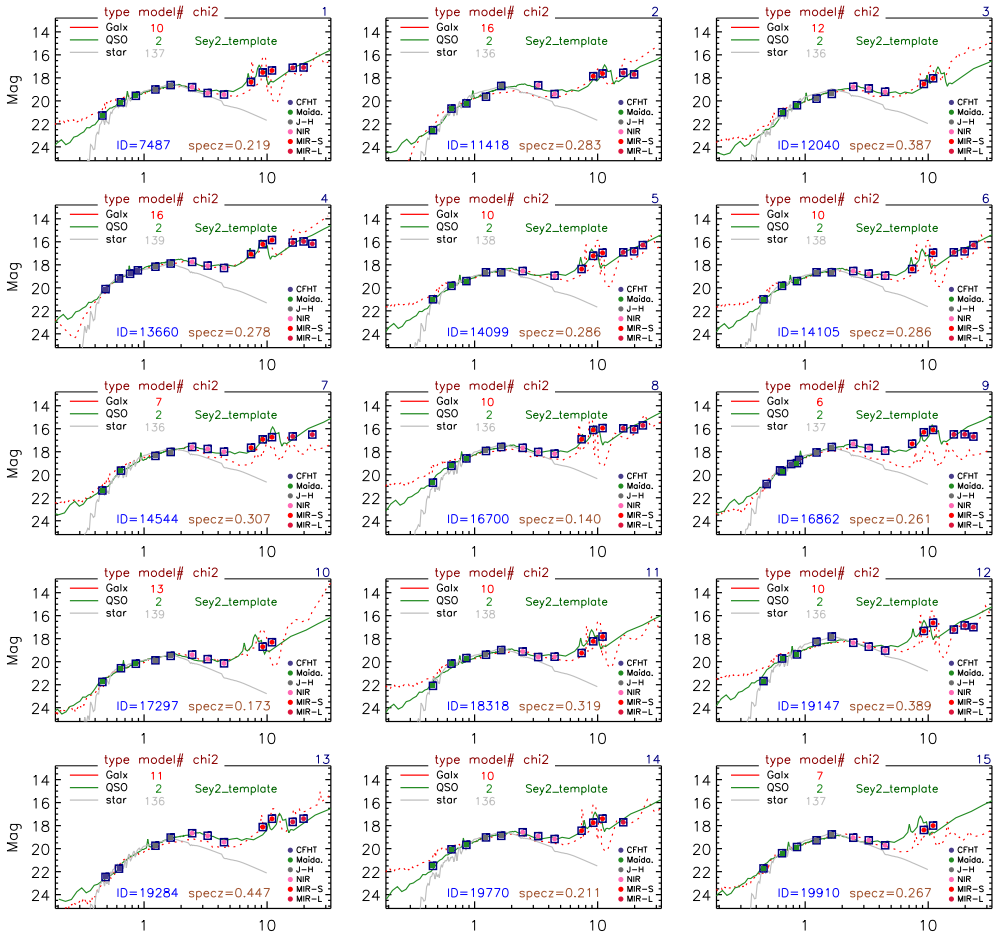

Figure 4.5 Examples of galaxies best-fit to Sey2 type galaxy. The observed fluxes from CFHT u* band to AKARI L24 band are presented by small squares. Overplotted green lines represent the template SED of Sey2 type from Polletta (2007). We also plotted SEDs of best-fit star and galaxy (red dotted) just for comparison.

Note that, in this stage, we focused on the separation of AGN components rather than a detailed analysis for the precise type-decision of individual source. Among these samples, we excluded the sources which have better fit to AGN or composite types than to SFGs. And the sources whose SED fit had quite similar χ^2 for the both SFG and AGN were also excluded. The number of source having best-fit to stellar SED was about 120 and they were also excluded. Finally, we have about 600 galaxies to calculate the mid-IR luminosity function.

4.4 Luminosity Function Procedure

4.4.1 K-correction for AKARI bands

The observed wavelength from a galaxy is different from the one that was emitted, due to cosmological redshift, z. When we estimate intrinsic galaxy luminosity at a certain wavelength, it is necessary to correct for the fact that a fixed passband for observation corresponds to a different range of wavelengths in the rest frame of galaxy at z. In this situation, the K-correction allows us to transform the observed flux (or apparent magnitude) at observed wavelength λ_0 into that of the emitted wavelength, λ_e in the rest frame (or absolute magnitude). This is a purely technical effect occurred by the redshift of spectra and a fixed spectral-response band (Oke & Sandage, 1968). It is composed of two parts, one of which is $(1 + z)$ responsible for the effective band width, thus independent of SED, and the other is the ratio of F_{ν_e}/F_{ν_0}, thus a function of λ and SED as shown in Eq. 4.1. Therefore, the K-correction depends on the SED of galaxy, its redshift (z), and the filter response ($S(\lambda)$) used for observation.

$$K(z) = (1 + z)\frac{\int F(\lambda)S(\lambda)d\lambda}{\int F(\frac{\lambda}{1+z})S(\lambda)d\lambda} \tag{4.1}$$

For the calculation of K-correction, we used the response curves of the IRC

filter bands and SED model templates from Polleta et al. (2007). Convolving each model with these filter function can give us the K-correction values for the NIR/MIR bands as a function of redshift. This procedure is important because it is used to estimate absolute magnitude (i.e., intrinsic luminosity measured in the corresponding passband), which will be used, in turn, to calculate z_{max} for $1/V_{max}$ method.

Figure 4.6 shows the K-correction for three NIR bands (N2, N3, and N4), using some of representative SED templates from the Polleta et al. (2007). The NIR bands take mainly stellar emission of Rayeigh-Jean tail part, therefore, the K-correction curves seem to be almost model-independent, and shows negative K-correction except for the composite type. Only the curve for the starburst Apr220 shows the considerable changes according to the wavelength bands.

Figure 4.7 shows the K-correction for three MIR-S bands (S7, S9W, and S11), using the same SED templates from the Polleta et al. (2007). The MIR-S bands show model dependencies for starbursts and star-forming galaxies because the MIR-S bands are affected by the emission features in these kinds of galaxy types, whereas the NIR bands mainly take monotonically decreasing stellar emission. Especially, the 7μm band shows the most sensitive dependencies, because the 7μm band width includes the PAH features 6.2 μm, 7.7 μm, and 8.6μm according to the redshift. But the 8.6μm feature leaves this band very soon (around $z \sim 0$) because this feature is located at the boundary of the S7 band. From $z \sim 0.11$, the 7.7 μm PAH feature begins to move out from this band. This means that the K-correction is not negligible in the MIR bands. In case of early-type, it seems that K-correction is not much different from those for the NIR bands. The other MIR-S bands (S9W and S11 band) show different shapes of correction curve from that of S7 band. The band width of the S9W is much wider than the other MIR-S bands (ranging $6 \sim 11\mu$m, approximately), its width includes the most parts of the other two bands while the S11 band is comparable to S7. Compared to the MIR-S bands, the MIR-L bands

are not affected much by the emission (Fig. 4.8) because the redshifted features are not reached the MIR-L bands in the redshift range of interest (below 0.6).

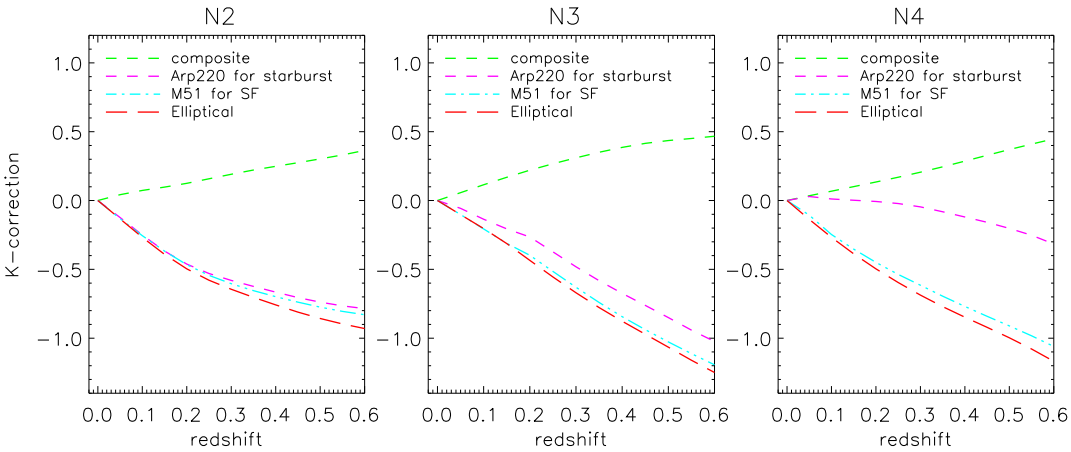

Figure 4.6 K-corrections for the IRC N2 (2μm, the left-most panel), N3 (3μm, middle panel), and N4 (4μm, the right-most panel) bands, using representative galaxy templates from Polleta et al. (2007). Red color is used for elliptical, cyan color for star-forming, magenta for starburst, and green color for composite type. The NIR band takes mainly stellar emission longward of Wien peak, that is, Rayeigh-Jean tail part, therefore, appearing almost model-independent, and shows negative K-correction except for the composite type. (See Fig. 4.7 and Fig. 4.8, to compare with those of the MIR bands.)

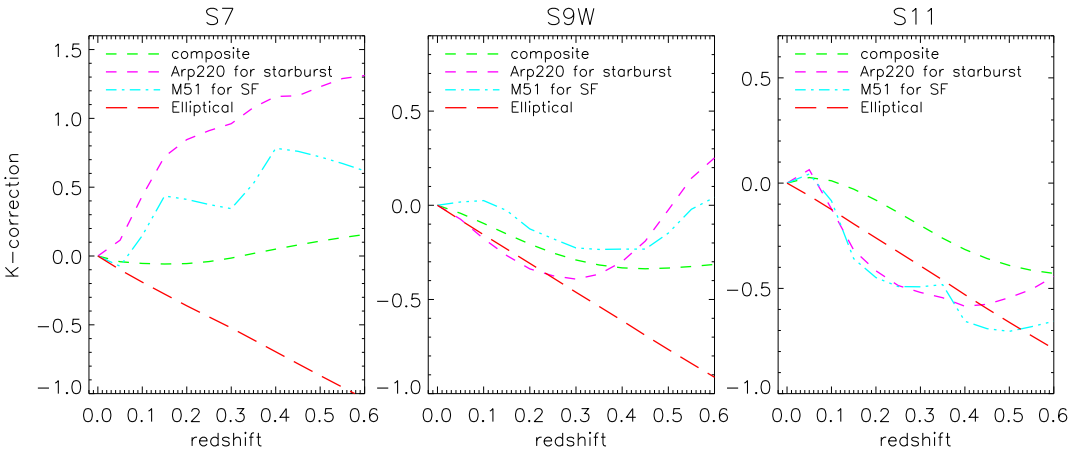

Figure 4.7 K-corrections for the S7 (the left-most panel), S9W (middle panel), S11 (the right-most panel) bands, using some representative galaxy templates from Polleta et al. (2007), the K-corrections for the MIR-S bands are shown. The MIR-S bands are affected by the PAH emission features around the band widths while the NIR bands take mainly stellar emission. Therefore the 7μm (S7) band has the model dependency and shows positive K-correction for starbursts and star-forming galaxies because the 7μm band width includes the PAH features around 7 – 8μm in the redshift range of interest. The S9W and S11 bands show naturally different shapes of correction because the bandwidth and effective wavelength are different from that of S7.

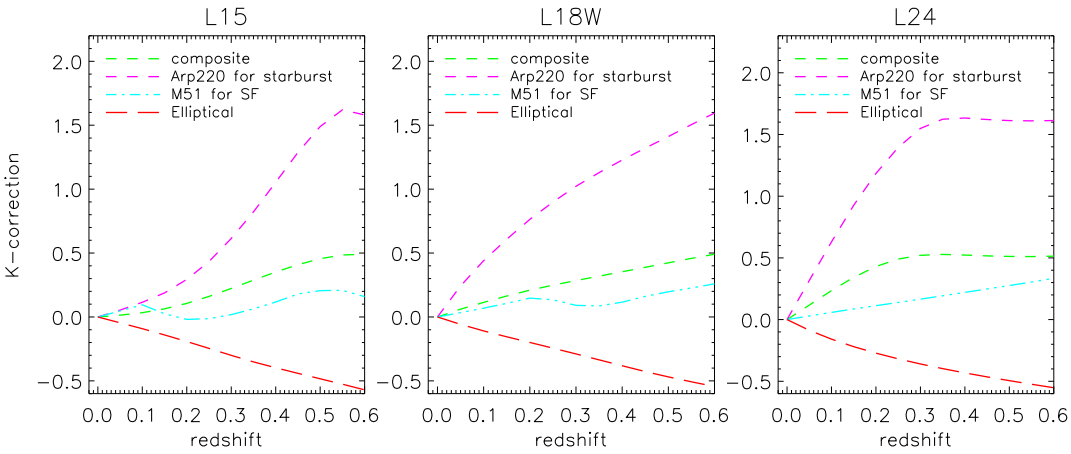

Figure 4.8 Using some representative galaxy templates from Polleta et al. (2007), the K-corrections for the MIR-L bands are shown, whose figures are drawn using the same methods as those of previous figures, 4.6 and 4.7. Compared to the MIR-S bands, the MIR-L bands are not affected much by the emission because the redshifted features are not reached the MIR-L bands in the redshift range of interest (below 0.6).

4.4.2 $1/V_{max}$ method

Over the several decades there have been various approaches devised to estimate the luminosity function; all of them have advantages but there is no perfect one. All the diverse methods perhaps suggest the efforts to avoid intrinsic bias that can lead to large uncertainties and inaccurate results. We used $1/V_{max}$ method, which have been established in the 60s (Schmidt 1968) and used by many researchers ever since (Babbedge et al. 2006; Ilbert et al. 2006; Huang et al. 2007; Caputi et al. 2007; Shim et al. 2009; Goto et al. 2010; Rodighiero et al. 2010) because of its advantage that it allows us to compute an luminosity function directly from data, with no parametric dependence or an assumed model. We began by calculating z_{max}, which is the maximum redshift at which a source could be observed by the detection limits of the survey (see Fig. 2.12), and is determined by using K-correction calculated from the template fits as explained previously. If this z_{max} is larger than the upper limit of the redshift bin, we took smaller one, that is $z_{max} = \min(z_{upper}$ of the z-bin, z_{max} of a source). A comoving volume V_{max} associated with a source is the maximum volume corresponding to the maximum redshift within which the source could still remain to be detected in our survey, and defined as $V_{max} = V(z_{max}) - V(z_{min})$, such that

$$V_{max} = \int_{z_{min}}^{z_{max}} \frac{dV}{dz} dz \; d\Omega \tag{4.2}$$

And then, for each luminosity bin, the LF(Φ) is derived as

$$\Phi(L) = \frac{1}{\Delta L} \sum_{i} \frac{1}{V_{max,i}} \omega_i. \tag{4.3}$$

where ΔL is the size of the luminosity bin, and ω_i is correction factor to compensate the selection bias for ith galaxy.

4.4.3 Completeness and the selection function

Complete resolution for bias and incompleteness seems a quite difficult task. They have always been problems that LFs research encounters ever since the first studies on the LFs in the mid-1930s (Hubble 1936, etc.). In general, when compiling a magnitude-redshift catalogue, we would like to be able to quantify in some way, how close we have a representative sample of the underlying distribution of galaxies.

However, there are a number of constraints preventing us from observing all objects in the sky. The methods to interpret and measure it accurately is not trivial. There are many diverse contributing sources of incompleteness that have to be corrected for and understood to construct accurately the LF. One of the fundamental incompleteness arises from the observational limitations of a telescope and is often referred to as Malmquist Bias (see e.g. Hendry and Simmons 1990). This is because, in the most general sense, an observer will measure apparent magnitudes of galaxies in a portion of the sky out to a faint limiting magnitude, imposed by the physical limitations of the telescope. As one images out to higher redshifts, only intrinsically bright sources will be observed. Since bright objects at large distances are rare, one observes a decrease in the number density of imaged objects as a function of redshift.

For the spectroscopic observation, using multi-fiber seems a good way, where optical fibers are positioned on a plate which has holes drilled at the positions of the sources measured from the photometry. A drawback of measuring redshifts in this way sometimes arises from physical spatial limitations at a high density region i.e. fiber collisions. However, this does not seem to be crucial for our targets selected for spectroscopic survey.

One way to quantify these effects is to compute the selection function, the probability that a galaxy at a redshift z will be included in a given survey. In the simplest scenario, the selection function may be expressed as the ratio of the selected sources with respect to all the underlying sources.

Since we used the spectroscopic samples only, the luminosity function has to be corrected for the incompleteness of these samples. The effect of the spectroscopic observation implies we are sampling less of the underlying distribution of galaxies, and the correction has to be applied to compensate the lack of number density of the sample. For the correction, a weighting scheme by incorporating the inverse of the selection function in the LF estimation is to be applied. To do this, we compared the number distribution of the spectroscopic sample with that of the sources in the NEP-Wide catalog as a function of observed magnitude. And, we used the detection completeness, (shown in Fig. 2.11), which mean the detection probability in the band.

4.5 Results and Discussion

4.5.1 8μm luminosity function

We constructed the 8μm luminosity function for star-forming galaxies at $0 < z < 0.3$ using $1/V_{max}$ method (Schmidt 1968). It is known that monochromatic 8μm luminosity ($L_{8\mu m}$) of SF galaxy is correlate well with the total IR luminosity (Babbedge et al. 2006; Huang et al. 2007) because the rest-frame 8μm fluxes are dominated by prominent PAH features which are sensitive to SF activity, meaning the MIR luminosity is a good indicator for the star formation activity hidden by dust. When we estimate the 8μm luminosity for this work, we are free from uncertainties occurred by redshifts since we used spectroscopic redshift. Thanks to the continuous wavelength coverage by the AKARI mid-IR bands, uncertainty for galaxy MIR SED is also very small, therefore, K-correction uncertainties are accordingly very small for low redshift (< 0.3) range.

In Fig. 4.9, we show the 8μm luminosity distribution of samples as a function of redshift (left panel). Rest-frame luminosity (in erg s $^{-1}$) is calculated using the

relation, $\nu L_\nu(8\mu m) = 4\pi {D_L}^2 F_\nu(8\mu m)$, where D_L is the luminosity distance. In this figure, the background circles represent all the spec-z samples, and black crosses represent the galaxies except for AGNs and stars. A vertical structure at around 0.09 is a known supercluster at z = 0.087 (see Ko et al. 2012). We found there is a small effect of this supercluster between a 10^8 – 10^9 range of the luminosity function, and we excluded it. Since $1/\mathrm{V}_{max}$ method assumes a homogeneous galaxy distribution, local over-/under-densities seem to affect the luminosity function. In our local sample, it is hard to find luminous galaxies while a large fraction of sources occupy between a 10^9 – 10^{10} range of luminosity.

Infrared luminosities (νL_ν) at 8μm are predominantly attributed to normal galaxies below $\sim$ $10^{11} L_\odot$, which means the contributions from luminous galaxies are very small. We also show the number of sources in the finer redshift bins ($0.0 < z < 0.1$, $0.1 < z < 0.2$, $0.2 < z < 0.3$) just for the information. These soures were used to construct the 8μm luminosity function of local (z < 0.3) galaxies observed in the NEP-Wide field.

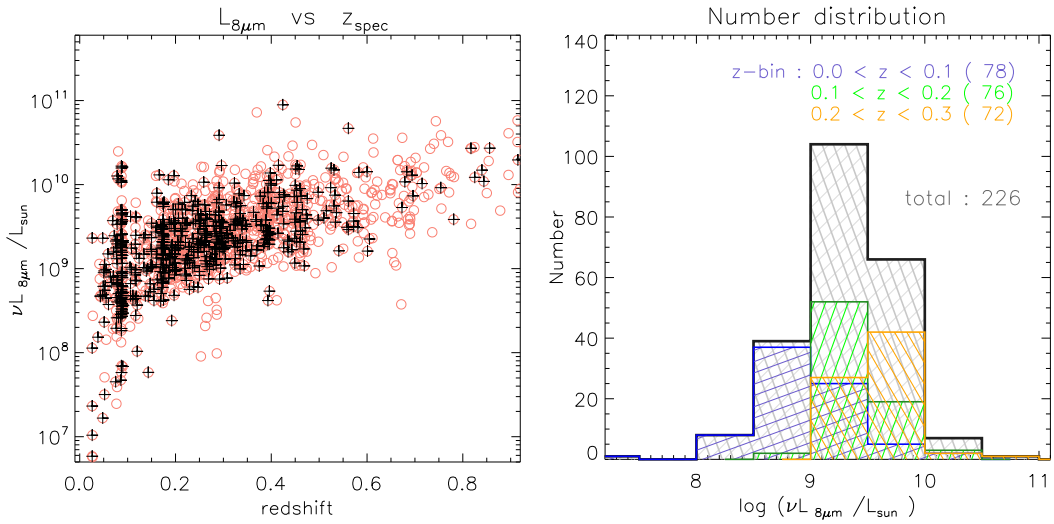

Figure 4.9 Left: 8μm luminosity distribution of spec-z samples as a function of redshift. Background circles represent all the spec-z sources and the black crosses indicate the galaxies except for AGNs (and stars). Right: the number of sources as a function of luminosity for z < 0.3, which were used to calculate the rest-frame 8μm LF.

In Fig.4.10, we show the rest-frame 8μm luminosity function of local galaxies observed in NEP-Wide field. For a comparison, other studies are also presented. Diamonds are from Babbedge's (2006) work base on the Spitzer Wide-area Infrared Extragalactic (SWIRE) data , and triangles are from Huang's work (2007) based on the *Spitzer* NOAO Deep Wide data. These show a good agreement in the bright-end, while there is a large discrepancies between the two in the range fainter than $10^{10}L_{\odot}$. Dark crosses are from Goto's work (2010) for $0.38 < z < 0.58$, based on the AKARI NEP-Deep field observation.

Babbedge constructed luminosity function from SWIRE Survey data and showed evidence for moderate positive luminosity evolution upto z $\sim$ 1.5. They used the SED models from Rowan-Robinson (2005) and tried to calculate photometric redshift for a large number of sources (upto $\sim$ 100,000, different numbers for each band). They carried out SED fitting to get 8μm luminosities and to separate the AGN sample from the SFGs. Huang (2007) used Spitzer survey data in the NOAO Deep Wide Field in Boötes (covering $\sim$ 6.8 sq. deg) to discuss PAH luminous galaxies and SFRs. Most (79 %) of their sources (4870 galaxies) have spectroscopic redshifts, allowing low uncertainties. They used SED models from Lu & Hur (2000). Both of these are the works on the 8μm luminosity function of local (z $<$ 0.3) galaxies.

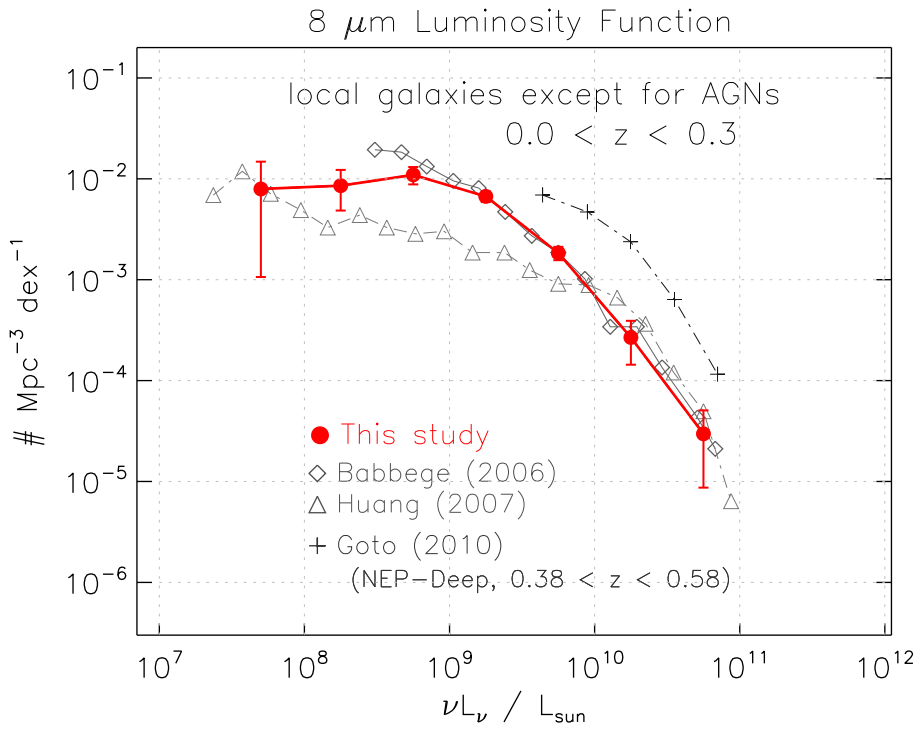

Figure 4.10 Rest-frame 8μm luminosity function of local galaxies observed in NEP-Wide data. Other studies are also presented to compare with this work. Diamonds are from Babbedge's (2006), and triangles are from Huang's work (2007). Dark crosses are from Goto's work (2010).

In the bright-range, our result also agrees well with the previous results, and is closer to the Babbege's results. In the faint-end, however, it is more closer to Huang's. The previous works with *Spitzer* used a large extrapolation from 24μm to estimate the rest-frame 8μm luminosity depending on SED models because of the wavelength gap between 8μm and 24μm. Compared to the previous works, the advantage of our work is useful spectroscopic redshifts data for many sources and AKARI's continuous filter coverage in the mid-IR wavelength, which allow us to avoid the uncertainties from photometric redshifts and a large extrapolation based on SED models. Goto's work is based on the deeper NEP-Deep data, but they did not present the LF for $0 < z < 0.3$ focusing on the high redshift range. The comparison of ours with Goto's result can imply the luminosity evolution to the higher redshifts, which is consist with the down-sizing pattern reported for other fields.

4.5.2 AKARI Mid-IR bands luminosity functions

In Fig. 4.11, we present AKARI S7 luminosity function derived using the same manner as the 8μm LF. AKARI S7 luminosity function shows similar result to the 8μm LF because the S7 band covers the PAH features around 8μm, which means that S7 luminosity also somehow can be a similar indicator for SF activity as the 8μm LF. The reults show that the slope at bright-end also seems to agree well with previous results of 8μm, but in the faint-end, the results doesn't look better than that of 8μm. It seems not easy to constrain the faint-end slope using these spectroscopic sample. We also present the S9W and S11 luminosity functions, showing the similar trend as that of S7 band.

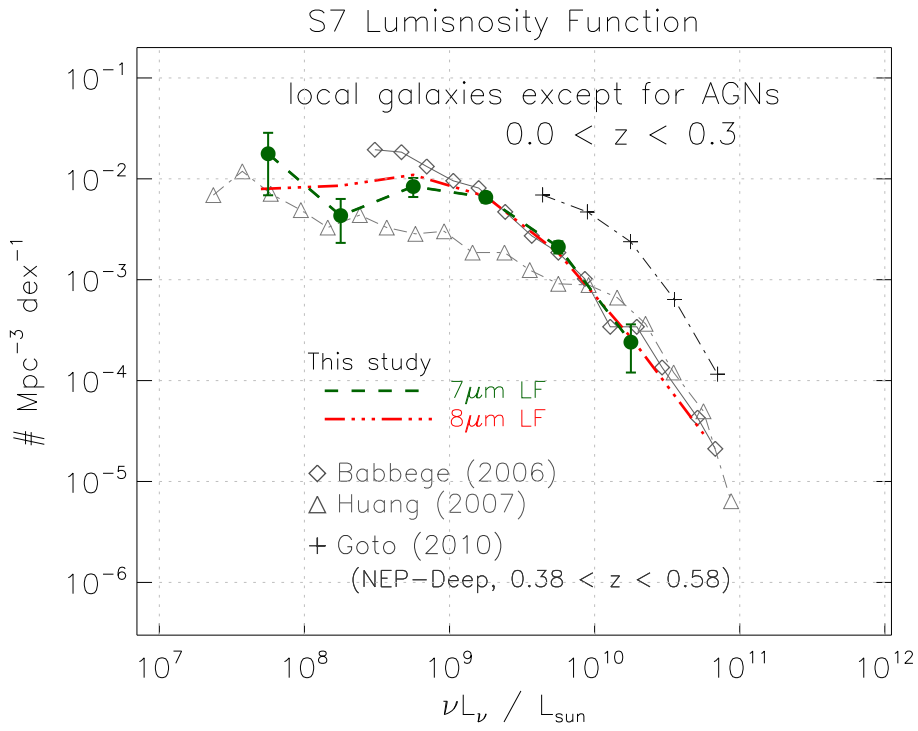

Figure 4.11 Rest-frame 7μm luminosity function of local galaxies observed in NEP-Wide data. Other studies are also presented to compare with this work. Diamonds are from Babbedge's (2006), and triangles are from Huang's work (2007). Dark crosses are from Goto's work (2010).

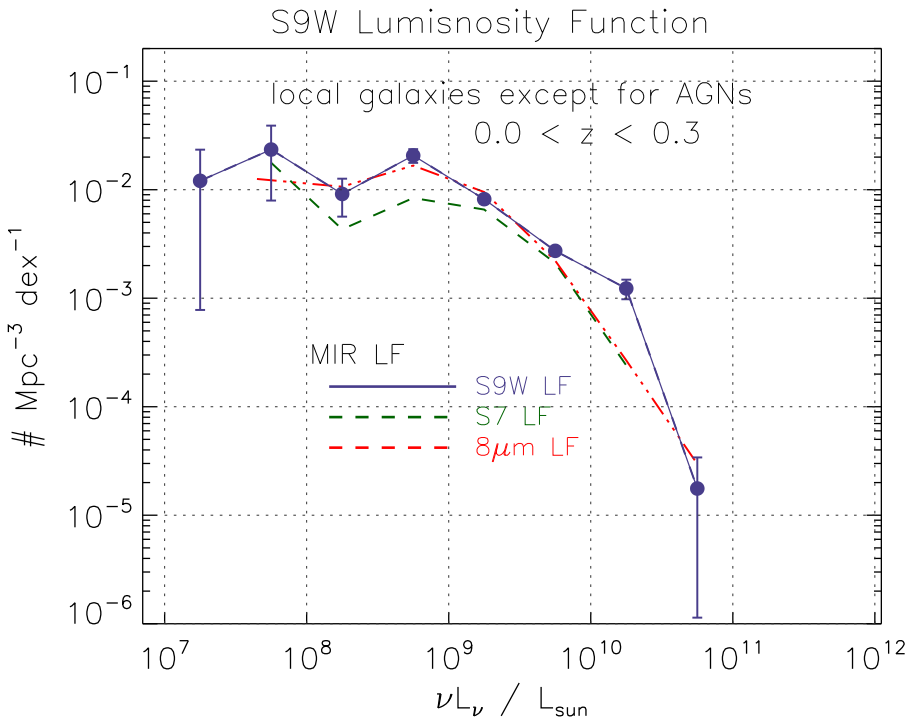

Figure 4.12 Rest-frame S9W luminosity function of local galaxies observed in NEP-Wide data. Other MIR bands LFs are also presented to compare with.

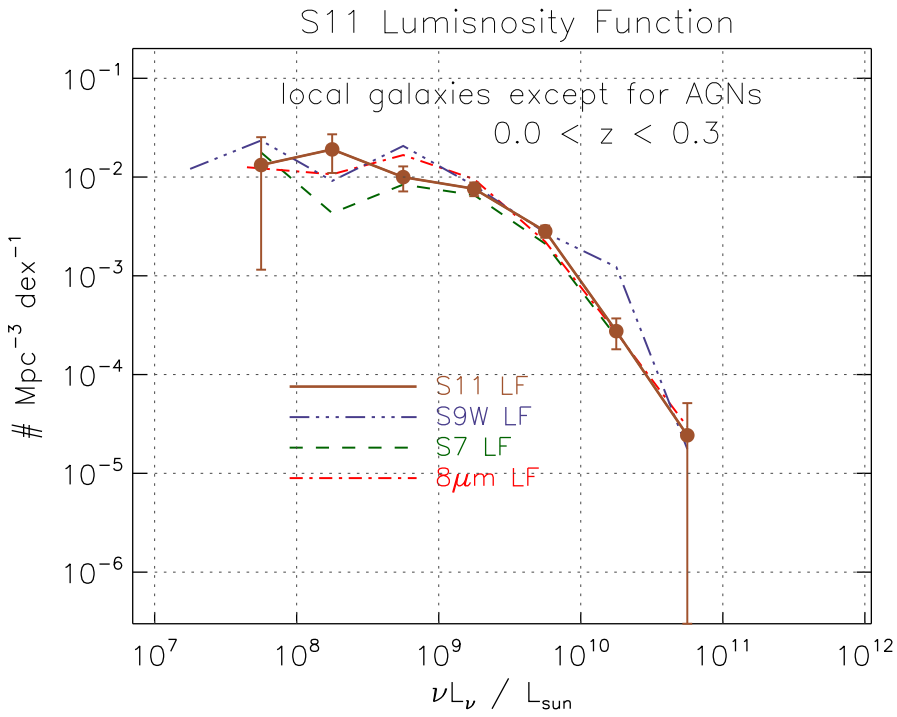

Figure 4.13 Rest-frame S11 luminosity function of local galaxies observed in NEP-Wide data. Other MIR bands LFs are also presented to compare with.

We may consider various contributing factors affecting LF uncertainties such as: galaxies that are missed because they are located close to bright stars or lie close to the edge of the CCD image; photometric uncertainties at each band for relatively faint soruces ; the inevitable selection bias occurred when we targeted sources for the spectroscopic observation; the wrong SED model adopted; the wrong K-corrections applied; galaxies with the same surface brightness that may or may not be detected depending on their shape and overall extent i.e. a compact object is more likely to have enough pixels above the detection limit than a very diffuse galaxy of the same brightness; adverse effects from a varying magnitude limit over CCD image, and so on.

At this stage, possible factors on this matter may likely be the selection bias for spectroscopic samples and photometric errors for the faint sources. Wrong SED model or wrong K-correction seems to be the factors somewhat depening on the redshift and photometric accuracy. Since we used quite accurate spectrosocopic redshifts and modern SED templates which are adopted these days, these do not seem to be the serious or crucial problems. But we need to test various other templates and compare with this results. Malmquist bias can be avoided if we use appropriate flux cut and completeness corrections. Anyway, it is not easy to get sufficient number of faint sample without bias and incompleteness.

Field surveys generally have flux limits (apparent magnitude limits) owing to the sensitivity or detection limits of the detector systems. This means that intrinsically bright galaxies are destined to be dominant in the survey samples because they are visible over large distances compared to the fainter ones. To fainter luminosities the surveyed volumes shrink substantially and the galaxy numbers drop significantly. At the level of inhomogeneities in the three-dimensional galaxy distribution do not always average out and can cause biases in the data. For instance the detection volume for the Small Magellanic Cloud is 4000 times smaller than for M87 just because of

the difference in their total magnitudes. Although we used fairly appropriate methods to avoid biases for the flux-limited sample, the substantial corrections at the faint end of the LF seems to make the shape highly uncertain in any case.

Chapter 5

Summary and Future Studies

We have carried out the reduction and analysis of NEP-Wide survey data obtained by the AKARI/IRC. In order to reduce spurious detection, we masked out the regions affected by instrumental effects such as MUX-bleeding trails, especially in the near infrared. The detected sources are compared with the data at the other wavelengths, including optical, ground-based near infrared observations, in addition to the other bands of AKARI. The areal coverage is about a 5.4 deg^2 circular field centered on NEP. The 5σ detection limits of the survey are around 21 AB mag in the NIR bands, 19 – 19.5 mag in the MIR-S bands, and 18.5 – 18.8 mag in the MIR-L bands.

The ancillary optical data from the CFHT and the Maidanak observatory are sufficiently deep to identify most of the AKARI sources. We carried out extensive comparisons by cross-matching of the sources among the photometric bands ranging from optical to mid infrared wavelengths in order to confirm the validity of the detected sources and exclude the low-reliability sources. Using these results, we produced a band-merged source catalogue covering the wavelength bands from the u^* band to the MIR $L24$ band. This catalogue contains about 114,800 entries. Based on this catalogue, we have shown the characteristics of the sources using various color-

color diagrams. By comparing and using optical stellarity, we found that the NIR and MIR-S band colors are statistically a good indicator for the star-galaxy separation. Except for the star-like objects, most of the NEP-Wide sources appear to be various types of star forming galaxies. The sources detected in all of the AKARI/IRC bands include interesting sources such as PAH galaxies, AGNs, ULIRGs or DOG candidates, and MIR-bright early-type galaxies.

NEP-Wide catalogue covers moderately large sky area with wide wavelength range. It is complementary to the NEP-Deep catalogues by Wada et al. (2007) and Takagi et al. (2012) which has better sensitivity and smaller angular coverage, but the same filter bands. The Spitzer also carried out large area surveys such as SWIRE and FLS. These surveys are carried out with all wide-band filters of Spitzer: 3.6 4.5, 5.8 and 8.0 μm with IRAC and 24, 70 and 160 μm with MIPS instrument. This should be compared to the nearly continuous wavelength coverage of AKARI's NEP surveys from 2.4 to 24 μm. The FLS covered the area of about 5 square degrees which is similar to that of the NEP-Wide. The survey area of SWIRE is about 10 times larger, but composed of several different fields.

We made an analysis on the subset of the NEP-Wide data having spectroscopic redshift. Using $1/V_{max}$ method, we estimated 8μm luminosity functions of star-forming galaxies in the lower redshift range ($0 < z < 0.3$). Compared to the other previous work, the advantage of this work is useful spectroscopic redshifts and AKARI's continuous filter coverage in the mid-IR wavelength, which allow us to avoid the uncertainties from photometric redshifts and a extrapolation relying on SED models. AKARI S7 luminosity function is similar to 8μm luminosity function because the S7 band covers PAH features around the 8μm. We also presented other MIR bands LFs, for comparison. The slope at bright-end seems to agree well with previous results for local universe, which suggest the downsizing evolutionary pattern together with the LF of the NEP-Deep field (Goto et al. 2010). But it is not

easy to constrain the faint-end slope using our spectroscopic sample.

This study is not a completed work, which means we have the next stage to go on. Based on the results of this work. we are going to examine if the extension of this work to the higher redshift range and for other type of sources can be possible. We have to test various SED templates (the FIR wavelength) to confirm the total infrared luminosities. Also, we are also going to estimate SFRs and luminosity densities to discuss the evolutionary properties of local galaxies.

This work is based on observations with AKARI, a JAXA project with the participation of ESA, universities and companies in Japan, Korea, the UK, and Netherlands. This work contains many data obtained by the following ground-based telescopes: Maidanak Observatory's 1.5 m, KPNO 2.1 m, and CFHT 3.5 m telescopes as well as the spectroscopic data obtained by MMT/Hectospec and WIYN/Hydra.

Bibliography

Babbedge, T. S. R., Rowan-Robinson, M., Vaccari, M., Surace, J. A., Lonsdale, C. J., Clements, D. L., Fang, F., Farrah, D., Franceschini, A., Gonzalez-Solares, E., Hatziminaoglou, E., Lacey, C. G., Oliver, S., Onyett, N., Pérez-Fournon, I., Polletta, M., et al. 2006, MNRAS, 270, 1159

Beichman, C. A., Neugebauer, G., Habing, H. J., Clegg, P.E., Chester, T. J. (eds) 1988, "IRAS Explanatory Supplement", NASA

Bertin, E., & Arnouts, S. 1996, A&AS, 117, 393

Capak, P., Aussel, H., Ajiki, M., McCracken, H. J., Mobasher, H. J., Scoville, N., Shopbell, P., Taniguchi, Y., Thompson, D., Tribiano, S., Sasaki, S., Blain, A. W., Brusa, M., et al. 2007, ApJS, 172, 99

Caputi, K. I., Lagache, G., Yan, L., Dole, H., Bavouzet, N., Le Floc'h, E., Choi, P. I., Helou, G., and Reddy, N., et al. 2007, ApJ, 660, 97

Clements, D. L., Desert, F.-X., Franceschini, A. 2001, MNRAS, 325, 665

Condon, J. J. 1974, ApJ, 188, 279

Elbaz, D., Cesarsky, C. J., Fadda, D., Aussel, H., Désert, F. X., Franceschini, A., Flores, H., Harwit, M., Puget, J. L., et al. 1999, A&A, 351, L37

Fang, Fan, Shupe, David L., Xu, Cong, Hacking, Perry B. 1998, ApJ, 500, 693

Finlator, K., Ivezić, Z., Fan, X., Strauss, M. A., Knapp, G. R., Lupton, R. H., Gunn, J. E., Rockosi, C. M., Anderson, J. E., Csabai, I., Hennessy, G. S., Hindsley, R. B., Mckay, T. A., Nichol, R. C., Schneider, D. P., Smith, J. A., yok, D. G., et al. 2000, ApJ, 120, 2615

Flores, H., Hammer, F., Thuan, T. X., Césarsky, C., Desert, F. X., Omont, A., Lilly, S. J., Eales, S., Crampton, D., Le Févre, O. 1999, ApJ, 517, 148

Franceschini, A.; Danese, L.; de Zotti, G.; Xu, C. 1988, MNRAS, 233, 175

Fukugita, M., Shimasaku, K., Ichikawa, T. 1995, PASP, 107, 945

Gioia, I. M., Henry, J. P., Mullis, C. R., Böhringer, H., Briel, U. G., Voges, W., Huchra, J. P. 2003, ApJS, 149, 29

Goto, T., Takagi, T., Matsuhara, H., Takeuchi, T. T., Pearson, C., Wada, T., Nakagawa, T., Ilbert, O., Le Floc'h, E., Oyabu, S. et al. 2010, A&A, 514, A6

Goto, T., Arnouts, S., Inami, H., Matsuhara, H., Pearson, C., Takeuchi, T. T., Le Floc'h, E., Takagi, T., et al. 2011, MNRAS, 410, 573

Hacking, P., & Houck, J. R. 1987, ApJS, 63, 311

Hendry, M. A. and Simmons, J. F. L. 1990, A&A, 237, 275

Henry, J. P., Gioia, I. M., Mullis, C. R., Voges, W., Briel, U. G., Böhringer, H., Huchra, J. P. 2001, ApJ, 553, L109

Henry, J. P., Mullis, Christopher R., Voges, W., Böhringer, H., Briel, U. G., Gioia, I. M., Huchra, J. P. 2006, ApJS, 162, 304

Hogg, D. W. 2001, AJ, 121, 1207

Holloway, H. 1986, J. Appl. Phys., 60, 1091

Houck, J. R. 1988, Lecture Note in Physics, 297, 340,

Hwang, N., Lee, M. G., Lee, H. Mok., Im, M., Kim, T., Matsuhara, H., Wada, T., Oyabu, S., Pak, S., Chun, M.-Y., et al. 2007, ApJS, 172, 583

Huang, J.-S., Ashby, M. L. N., Barmby, P., Brodwin, M., Brown, M. J. I., Caldwell, N.; Cool, R. J., Eisenhardt, P., et al. 2007, ApJ, 664, 840

Hubble, E. 1936, ApJ, 84,517

Im, M., Ko, J., Cho, Y., Choi, C., Jeon, Y., Lee, I., Ibrahimov, M. 2010, J. Korean Astron. Soc., 43, 75

Ilbert, O., Lauger, S., Tresse, L., Buat, V., Arnouts, S., Le Févre, O., Burgarella, D., Zucca, E., Bardelli, S., Zamorani, G., et al. 2006, A&A, 453, 809

Jarrett, T. H., Cohen, M., Masci, F., Wright, E., Stern, D., Benford, D., Blain, A., Carey, S., Cutri, R. M., Eisenhardt, P., et al. 2011, ApJ, 735, 112

Jeon, Y., Im, M., Ibrahimov, M., Lee, H. M., Lee, I., Lee, M. G., 2010, ApJS, 190, 166

Johnston, R. 2011, A&AR 19, 41

Kawada, M., Baba, H., Barthel, P. D., Clements, D., Cohen, M., Doi, Y., Figueredo, E., Fujiwara, M., Goto, T., Hasegawa, S., et al. 2007, PASJ, 59, S389

Kessler, M. F., Steinz, J. A., Anderegg, M. E., Clavel, J., Drechsel, G., Estaria, P., Faelker, J., Riedinger, J. R., Robson, A., Taylor, B. G., Ximénez de Ferrán, S. 1996, A&A, 315, L27

Kim, S. J., Lee, H. M., Matsuhara, H., Wada, T., Oyabu, S., Im, M., Jeon, Y., Kang, E., Ko, J., Lee, M. G., et al. 2012, A&A, 548, A29

Ko, J., Im, M., Lee, H. M., Lee, M., G., Kim, S., J., Shim, H., Jeon, Y., Hwang, H. S., Willmer, C. N. A., et al. 2012, ApJ, 745, 181

Kollgaard, R. I., Brinkmann, W., Chester, M. M., Feigelson, E. D., Hertz, P., Reich, P., Wielebinski, R. 1994, ApJS, 93, 145

Kron R. G. 1980, ApJS, 43, 305

Lacy, M., Riley, J. M., Waldram, E. M., McMahon, R. G., Warner, P. J. 1995, MNRAS, 276, 614

Lee, H. M., Im, M., Wada, T., Shim, H., Kim, S. J., Lee, M. G., Hwang, N., Matsuhara, H., Nakagawa, T., Oyabu, S., et al. 2007, PASJ, 59, S529

Lee, H. M., Kim, S. J., Im, M., ; Matsuhara, H., Oyabu, S., Wada, T., Nakagawa, T., Ko, J., et al. 2009, PASJ, 61, 375

Le Floc'h, E., Papovich, C., Dole, H., Bell, E. F., Lagache, G., Rieke, G. H., Egami, E., Pérez-González, P. G., et al. 2005, ApJ, 632, 169

Lorente, R., Onaka, T., Ita, Y., Ohyama, Y., Tanabe, T., Pearson, C. 2008, AKARI IRC Data User Manual, ver.1.4

Loiseau, N., Reich, W., Wielebinski, R., Reich, P., Muench, W. 1988, A&AS, 75, 67

Marshall, F. E., Reichert, G. A., White, R. A. 1985, Bull. Am. Astron. Soc., 17, 596

Matsuhara, H., Wada, T., Matsuura, S., Nakagawa, T., Kawada, M., Ohyama, Y., Pearson, C., Oyabu, S., Takagi, T., Serjeant, S., et al. 2006, PASJ, 58, 673

Murakami, H., Baba, H., Barthel, P., Clements, D. L., Cohen, M., Doi, Y., Enya, K., Figueredo, E., Fujishiro, N., Fujiwara, H., et al. 2007, PASJ, 59, S369

Nakagawa, T., Murakami, H. 2007, AdSpR, 40, 684

Neugebauer, G., Habing, H. J., van Duinen, R., Aumann, H. H., Baud, B., Beichman, C. A., Beintema, D. A., Boggess, N., Clegg, P. E., de Jong, T., et al. 1984, ApJ, 278, L1

Offenberg, J. D., Fixsen, D. J., Rauscher, B. J., Forrest, W. J., Hanisch, R. J., Mather, J. C., McKelvey, M. E., McMurray, R. E., Jr., Nieto-Santisteban, M. A., Pipher, J. L., et al. 2001, PASP, 113, 240

Oke, J. B. & Sandage, A. 1969, ApJ, 154, 210

Oke, J. B. & Gunn, J. E. 1983, ApJ, 266, 713

Onaka, T., Matsuhara, H., Wada, T., Fujishiro, N., Fujiwara, H., Ishigaki, M., Ishihara, D., Ita, Y., Kataza, H., Kim, W., et al. 2007, PASJ, 59, S401

Onaka, T., Nakagawa, T. 2005, AdSpR, 36, 1123

Ohyama, Y., Wada, T., Matsuhara, H., Takagi, T., Akari Spicy Team, et al. 2009, ASPC, 418, 329

Pérez-González, P. G., Rieke, G. H., Egami, E., Alonso-Herrero, A., Dole, H., Papovich, C., Blaylock, M., Jones, J., Rieke, M., Rigby, J., et al. 2005, ApJ, 630, 82

Pilbratt, G. L., Riedinger, J. R., Passvogel, T., Crone, G., Doyle, D., Gageur, U., Heras, A. M., Jewell, C., Metcalfe, L., Ott, S., Schmidt, M. 2010, A&A, 518, L1

Polletta, M., Tajer, M., Maraschi, L., Trinchieri, G., Lonsdale, C. J., Chiappetti, L., Andreon, S., Pierre, M., Le Févre, O., Zamorani, G., et al. 2007, ApJ, 663, 81

Puget, J. L., Lagache, G., Clements, D. L., Reach, W. T., Aussel, H., Bouchet, F. R., Cesarsky, C., Désert, F. X., Dole, H. et al. 1999, A&A, 345, 29

Rodighiero, G., Vaccari, M., Franceschini, A., Tresse, L., Le Fevre, O., Le Brun, V., Mancini, C., Matute, I., Cimatti, A., Marchetti, L., et al. 2010, A&A, 515, A8

Rowan-Robinson M., Helou G., Walker D., 1987, MNRAS, 227, 589

Rowan-Robinson, M., Lari, C., Perez-Fournon, I., Gonzalez-Solares, E. A., La Franca, F., Vaccari, M., Oliver, S., Gruppioni, C., Ciliegi, P., et al. 2004, MNRAS, 351, 1290

Rowan-Robinson, M., Mann, R. G., Oliver, S. J., Efstathiou, A., Eaton, N., Goldschmidt, P., Mobasher, B., Serjeant, S. B. G., Sumner, T. J., et al. 1997, MNRAS, 289, 490

Rowan-Robinson, M., Babbedge, T., Surace, J., Shupe, D., Fang, F., Lonsdale, C., Smith, G., Polletta, M., Siana, B., et al. 2005, AJ, 129, 1183

Saunders, W., Rowan-Robinson, M., Lawrence, A., Efstathiou, G., Kaiser, N., Ellis, R. S., Frenk, C. S. 1990, MNRAS, 242, 318

Schmidt, M. 1968, ApJ, 151, 393

Sedgwick, C., Serjeant, S., Sirothia, S., Pal, S., Pearson, C., White, G. J., Matsuhara, H., Matsuura, S., Shirahata, M., Khan, S., et al. 2009, ASPC, 418, 519

Serjeant, S., Carramiõana, A., Gonzáles-Solares, E., Héraudeau, P., Mújica, R., Perez-Fournon, I., Sedgwick, N., Rowan-Robinson, M., et al. MNRAS335, 813

Shim, H., Colbert, J., Teplitz, H., Henry, A., Malkan, M., McCarthy, P., Yan, L. 2009, ApJS, 696, 785

Shim, H., Im, M., Pak, S., Choi, P., Fadda, D., Helou, G.; Storrie-Lombardi, L. 2006, ApJS, 164, 435

Shim, H., Im, M., Lee, H. M., Lee, M. G., Kim, S. J., Hwang, H. S., Hwang, N., Ko, J., 2011, ApJ727, 14

Silva, L., Granato, G. L., Bressan, A., Danese, L. 1998, ApJ, 509, 103

Skrutskie, M. F., Cutri, R. M., Stiening, R., Weinberg, M. D., Schneider, S., Carpenter, J. M., Beichman, C., Capps, R., Chester, T., Elias, J., et al. 2006, AJ, 131, 1163

Smith, J. D. T., Draine, B. T., Dale, D. A., Moustakas, J., Kennicutt, R. C., Jr., Helou, G., Armus, L., Roussel, H., Sheth, K., Bendo, G. J., et al. 2007, ApJ, 656, 770

Takagi, T., Matsuhara, H., Goto, T., Hanami, H., Im, M., Imai, K., Ishigaki, T., Lee, H. M., Lee, M. G., et al. 2012, A&A, 537, A24

Takagi, T., Matsuhara, H., Wada, T., Oyabu, S., Imai, K., Pearson, C. P., Hanami, H., Onaka, T., Fujishiro, N., et al. 2007, PASJ, 59, 577

Takagi, T., Ohyama, Y., Goto, T., Matsuhara, H., Oyabu, S., Wada, T., Pearson, C. P., Lee, H. M., Im, M., et al. 2010, A&A, 514, A5

Tanabé, T., Sakon, I., Cohen, M., Wada, T., Ita, Y., Ohyama, Y., Oyabu, S., Uemizu, K., Takagi, T., et al. 2008, PASJ, 60, S375

van Dokkum, P. G. 2001, PASP, 113, 1420

Voges, W., Aschenbach, B., Boller, T, Bräuninger, H., Briel, U., Burkert, W., et al. 1999, A&A, 349, 389

Wada, T., Matsuhara, H., Oyabu, S., Takagi, T., Lee, H. M., Im, M., et al. 2008, PASJ, 60, S517

Wada, T., Oyabu, S., Ita, Y., Matsuhara, H., Pearson, C. P., Onaka, T., Ohyama, Y., Usui, F., Fujishiro, N., et al. 2007, PASJ, 59, S515

Werner, M. W., Roellig, T. L., Low, F. J., Rieke, G. H., Rieke, M., Hoffmann, W. F., Young, E., Houck, J. R., Brandl, B., et al. 2004, ApJS, 154, 1

White, G. J., Pearson, C., Braun, R., Serjeant, S., Matsuhara, H., Takagi, T., Nakagawa, T., Shipman, R., Barthel, P., Hwang, N., et al. 2010, A&A, 517 A54

요 약

적외선 우주 망원경 아카리(AKARI)가 그 임무 중 하나인 황도 북극(North Ecliptic Pole, NEP) 지역에 대한 관측을 성공적으로 수행하고 많은 양의 데이터를 쏟아내었다. 본 연구는 이 관측 데이터를 처리하고, 신뢰성 있는 분석을 바탕으로 비교적 가까운 곳에 위치한 은하(local galaxies)들의 밝기(luminosity) 분포를 조사하여, 은하의 진화(evolution)에 관해 논의하였다. 아카리가 관측한 곳은 황도 북극을 중심으로 대략 5.4 $\deg^2$의 영역이며, 아카리에 장착된 적외선 카메라(IRC)의 9개 측광 밴드를 통해서 관측되었다. 근적외(NIR)에서 중적외(MIR) 측광 밴드로 관측된 다양한 외부 은하들을 이해하기 위해 수많은(∼10만개) 소스들을 측광학적으로 조사하여, 적외선 천체 목록(catalogue)을 만든 후 그들의 통계적인 특징들을 보고자 하였다.

천문 관측 본래의 특징 뿐 아니라 적외선 파장대와 관측 기기의 고유한 특성 등에서 비롯되는, 우주선(cosmic-ray)이나 Mux-bleeding 현상과 같은 수많은 거짓 신호·소스들을 제거하기 위해 폭넓은 시도와 노력을 기울였다. 검출된 소스들의 갯수는 필터 밴드에 따라 다르게 나타나는데, 근적외에서 10만 여개인데 반해, 중적외 파장대에서 만 5천여개 정도이며, 소스의 검출 한계(5-σ)는 대략 근적외에서 21 등급(AB), 중적외에서는 19.5 – 18.5 등급(AB) 수준이었다.

검출된 소스들의 정당성 확보를 위해, 보유한 보조 데이터를 포함한 모든 밴드의 소스를 이용하여 교차적인 매칭(cross-matching)을 통해 거짓 소스들을 최대한 가려내었다. 모든 결과를 종합한 최종 통합(band-merged) 카타로그에는 대략 114,800개의 소스들이 등재되었고, 여기에는 우리 은하의 항성들을 비롯하여 다양한 외부 은하 천체들이 포함되어 있다. 광학 파장대(r', R)의 stellarity와 등급을 이용하면, 우리 은하의 별들을 통계적으로 골라내는 좋은 기준을 제시할 수 있고, 은하들의 통계적인 특성과 분류에 대해서는 아카리의 근적외 및 중적외 밴드의 색지수(color)를 이용하여 효율적으로 논의할 수 있음을 보였다.

이들 중 분광 관측으로 적색이동(redshift, z) 값을 알아낸 소스들을 이용하여 근접한 ($z < 0.3$) 은하들의 적외선 광도 분포를 조사하였다. 근접한 우주에서 광도함수에 기여하는 은하들은 밝기가 보통인 은하들이 대다수인 것으로 보인다. 가장 널리

받아들여지고 있는 $1/V_{max}$ 방법을 이용하여, 중적외 파장대의 광도 함수(luminosity function)를 측정한 결과, 밝은 쪽에서는 최근에 보고된 연구와 잘 일치하는 결과를 얻었다. 이것을 NEP-Deep data의 결과(Goto et al. 2010)와 함께 비교하면, z에 따른 luminosity evolution의 관측적인 신호로 해석할 수 있고, 근접한 우주(local universe)에 이르기까지 은하들이 down-sizing의 진화 패턴을 따르고 있다는 사실을 짐작하게 한다. 반면 어두운 쪽에서는, 경향성을 판단하기 어려운 불확실성을 내포하고 있는데, 상대적으로 어두운 은하들이 관측·검출될 확률과, 표본 추출된 소스들의 편향성(bias) 및 어둡기 때문에 생기는 측광 오차 등에 의해 영향을 받는 것으로 판단되며, 이것은 광도함수의 연구에 있어 신중하게 해결해야 할 문제이다.

주요어: 데이터 분석, 천체 목록, 적외선, 은하, 광도 함수, 탐사 관측

학 번: 2004-30943

감 사 의 글

시간이 흐르고 학위 논문이 출판되기까지 긴 시간 동안 힘과 격려를 주신 모든 분들께 감사드립니다. 드디어 이렇게 마지막 페이지에 도달했습니다. 여기에 이르기까지 참 많은 사건들이 있었네요. 그 와중에도 한결같이 믿어주시고 버팀목이 되어 주신 부모님께 고개 숙여 감사드립니다. 이런 마음 어찌 몇 자 글로 표현이 되겠습니까. 그리 잘 나지 못한 아들의 느릿느릿한 걸음을 묵묵히 기다려 주신 덕분에 포기하지 않고 여기까지 올 수 있었습니다.

부족한 저를 이끌어 결실을 맺도록 해 주신 지도 교수님께 감사드립니다. 한 사람의 천문학자로서 새로운 출발점에 설 수 있도록 도와주셨습니다. 학과 모든 교수님들의 소중한 가르침에 감사드리며 행정실에 계신 분들께 받은 도움과 지지 또한 잊을 수 없을 것입니다.

힘든 학위 과정을 아무렇지 않은 듯 뚝딱 해치우신 여러 선배 학우들의 내공에 존경을 표합니다. 더불어 같이 지내온 동료들에게도 심심한 감사와 존경을 표합니다. 가장 실질적이고 현실적인 도움을 여러분께 받지 않았나 싶습니다. 깊은 연구의 숲에서 길 잃고 헤메는 것을 취미삼아, 슬럼프라는 친숙한 벗과 함께 험난한 가시밭길을 헤쳐 나아가고 있는 여러 후배들에게서도 멋진 연구 결과를 기대합니다.

표현력 부족한 저인지라 긴 글로써 하나 하나 감사를 표시해도 부족함이 남겠지만, 여기까지 와서 시간과 지면에 쫓기며 하찮은 필력으로 어눌하게 구느니 이쯤에서 쿨하게 접는 것이 오히려 더 나을 것 같습니다. 그러나 얼굴 하나하나 떠올리며 고마운 마음 깊이 간직하고 있다는 것을 꼭 기억해 주시기 바랍니다..

저를 아는 모든 분들께 감사드리며, 그 동안 좀 더 쓸모 있는 가족의, 학과의 일원이 되지 못했던 것 같아 아쉬운 마음이 들지만, 이제는 제가 받은 것들을 베풀고 나누어 줄 수 있는, 좀 더 쓸모 있는 사회의 일원이 되도록 노력하겠습니다.